POLITECNICO DI TORINO

Ph.D. School

Ph.D. in Water and Territory Management
Engineering – XXV cycle

Ph.D. Thesis

River antidunes and bars: new models and nonmodal analysis

Riccardo Vesipa

Supervisors	**Ph.D. program coordinator**
Prof. Luca Ridolfi	
Ph.D. Carlo Camporeale	Prof. Claudio Scavia

20th March 2013

Alle persone speciali
che mi circondano, e
con cui ho il piacere
di vivere ogni giorno

Ringraziamenti

Scrivendo questa tesi ho riesumato appunti e lavori dei passati tre anni, e con loro ho avuto il piacere di rispolverare e ricordare tutti i piccoli eventi che li hanno accompagnati. La rabbia per una revisione negativa accompagnata però dagli incoraggiamenti di colleghi e amici, o la gioia di apprendere, in una spiaggia della piccola isola di Bozcada, che un paper era stato accettato. Ringrazio tutti coloro che in quei momenti sono stati con me.

Contents

Chapter 1

Introduction

1.1 An overview on morphodynamics

Scientists have been fascinated from centuries by the description
and the understanding of the motion of fluids. The main reason
is that a great number of phenomena is related with fluid motion,
ranging from the planetary scale (e.g., circulation of the atmo-
sphere, Schneider, 2006; Klein, 2010, and of the oceans, Wunsch &
Ferrari, 2004; Gargett, 1989), down to the microscopic scale (e.g.,
bacteria locomotion, Brennen & Winet, 1977; Guasto *et al.*, 2012).

One of the basic task of fluid mechanics is to describe the mo-
tion of a stream bounded by some provided surfaces (Chow, 1959;
Potter & Wiggert, 1991). The task is simple: provided a bound-
ary, the flow velocity profile (and the flow depth, if the flow has
a free surface) have to be computed. The problem, anyway, is
easy only to say, and exact solutions exists only in a limited num-
ber of cases, for instance when the laminar flow of a newtonian
fluid is confined by flat surfaces (Case, 1960; Wendl, 1999; Taylor,
1923). More complex geometries (Boutounet *et al.*, 2008; Ben-
jamin, 1959), flow unsteadiness (Williams, 1977; Miles, 1980), free
surface tension (Oron *et al.*, 1997; Craster & Matar, 2009), turbu-
lence (Woods, 2010; Simpson, 2001), complex rheologies (Crochet
& Walters, 1983; Griffiths, 2000) and many other factors (Linden,
1999; Ku, 1997) complicate the problem.

An additional source of complexity can be given by the nature of
the confinements which bound the flow. In many cases, especially

when environmental phenomena are considered, streams modify their own boundaries through a number of different mechanisms (Charru *et al.*, 2013; Blondeaux, 2001; Fagherazzi & Overeem, 2007), such as the transport of non cohesive particles (Seminara, 2010; de Swart & Zimmerman, 2009), the erosion of cohesive surfaces (Blank, 1970; Balmforth & Vakil1, 2012), chemical and thermal dissolution processes (Gilpin & Cheng, 1980; Dreybrodt, 1988). The modification of the boundaries, in turn, causes alterations in the flow structure which has driven the boundary modification (Seminara, 2010; de Swart & Zimmerman, 2009). This feedbacks' chain entails a strong coupling between the evolution of the flow field and that of the boundaries (Colombini & Stocchino, 2005; Kennedy, 1963), which often results in the self-organization of the dynamical system composed by the streams and the boundaries into very ordered and regular patterns (Ikeda *et al.*, 1981; Camporeale & Ridolfi, 2012; Devauchelle *et al.*, 2010).

Morphodynamics is the branch of fluid mechanics devoted to study the interaction between a stream and its flow-influenced confinement (Seminara, 2010; Blondeaux, 2001; Charru *et al.*, 2013). Morphodynamics is particularly important because many environmental processes which determine the shape and the characteristics of Earth's landscapes are the result of complex interactions between geophysical flows (the fluid is usually water or air) and movable boundaries. Depending on the scale (Seminara, 2010; Colombini, 2004; Charru *et al.*, 2013), the type of fluid (Kocurek, 1991; Short *et al.*, 2005) and the mechanical and chemical properties of the boundaries (Sauermann *et al.*, 2001; Camporeale & Ridolfi, 2012; Haff & Anderson, 1993), the assortment of induced phenomena is really impressive.

The wind gives an important contribution in modeling the Earth's surface (Andreotti *et al.*, 2002; Neuman, 1993). Its effects are well visible especially in non vegetated zones, where the soil is fully exposed to the air streams (Edgett & Christensen, 1991). Remarkable examples of the morphologies generated by the winds are sand dunes (Sauermann *et al.*, 2000; Andreotti, 2004; Preusser *et al.*, 2002, figure 1.1*a*), when the movable boundary is made of sediment particles and snow formations, such us snow dunes (Birnbaum *et al.*, 2010; Frezzotti *et al.*, 2002, figure 1.1*b*), snow ripples (Kosugi *et al.*, 1992; Kobayashi & Ishida, 1979, figure 1.1*c*) and
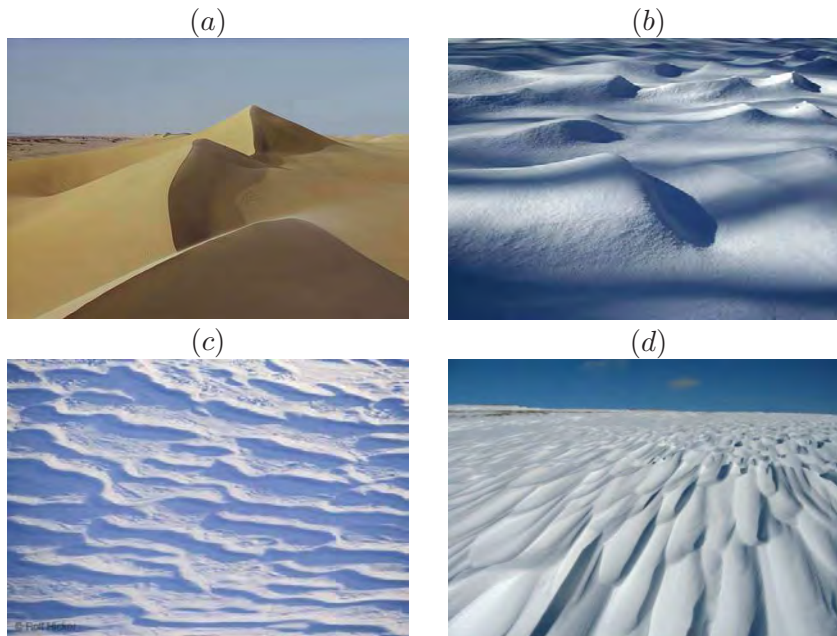
Figure 1.1. Morphologies generated by the interaction between non-cohesive particles and the wind: (*a*) sand dunes in the Egyptian desert; (*b*) snow dunes; (*c*) snow ripples and; (*d*) sastrugi.

sastrugi (Mondet *et al.*, 1997; Parish, 1988, figure 1.1*d*) when the movable boundary is made of snow particles.

The most important modeler of Earth's surface for the number and the importance of the driven morphological phenomena, is anyway water (Seminara, 2010; de Swart & Zimmerman, 2009; Blondeaux, 2001). Water flows over an impressive number of materials such as non cohesive sediments (Colombini, 2004; Charru *et al.*, 2013), cohesive substrates (Balmforth & Vakil1, 2012; Kostic *et al.*, 2010) and ice (Parker, 1975a; Camporeale & Ridolfi, 2012), with a large variety of scales (Ashmore, 1988; Charru *et al.*, 2013; Camporeale & Ridolfi, 2012) and behaviors, ranging from the laminar flow over an icicles (Ueno, 2003; Neufeld *et al.*, 2010) to the fully turbulent flow of rivers (Colombini, 2004; Seminara, 2010) or coastal currents (Blondeaux, 2001; de Swart & Zimmerman, 2009), and under many thermal and chemical conditions (Gilpin, 1981; Short *et al.*, 2005; Feltham & Worster, 1999).
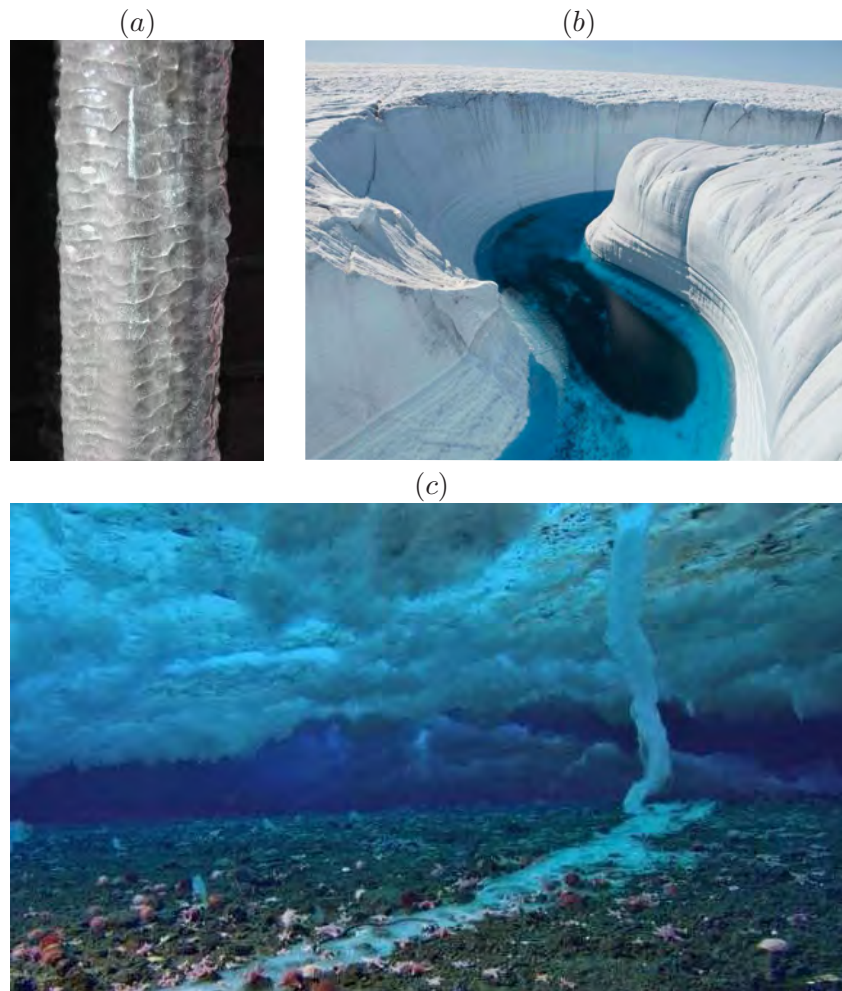
Figure 1.2. Morphologies generated by the interaction between water and ice: (*a*) ripples over an icicles; (*b*) meandering of a supra-glacial stream in Antarctica and; (*c*) formation of an icicle of brine in the polar environment.

The interaction between ice and water streams, is responsible of a number of phenomena that, despites difficult to be observed due to the ephemeral nature of ice, are astonishing and surprising. Examples are the formation of ripples on icicles (Ogawa & Furukawa, 2002; Camporeale & Ridolfi, 2012, figure 1.2*a*), the meandering of

supra-glacial streams (Ferguson, 1973; Parker, 1975a, figure 1.2*b*) and the formation of ice stalactites in polar oceans (Martin, 1974; Dayton & Martin, 1971, figure 1.2*c*).

Almost perpetual, at least for the humans perspective, are instated the morphological phenomena associated with the interaction between cohesive substrates and water films with chemical and thermal characteristics prone to drive chemical dissolution or deposition of the substrate. Examples or these hydro-chemical interactions are the scallops (Blumberg & Curl, 1974; Goodchil & Ford, 1971, figure 1.3*d*), the crenulations (Camporeale & Ridolfi, 2012; Chan & Goldenfeld, 2007, figure 1.3*e*) and the draperies (Martin-Perez *et al.*, 2012; Freile *et al.*, 1995, figure 1.3*f*).

It is with sediments, anyway, that water streams interact in the most spectacular, fascinating and widespread way. The characteristics of the water stream (e.g., Reynolds and Froude numbers) can vary over a wide ranges of values, but the shapes and patterns resulting from the interaction with sediments are always marvelous. We can start our quick glance over the sediment morphodynamic patterns by considering the three most important environments influenced by morphological processes: (i) seas; (ii) tidal inlet systems of sand barrier coastline and; (iii) rivers.

In the seas and in the oceans flow currents are generated by tides or winds (Peregrine, 1983; Garrett & Munk, 1979; Battjes, 1988) and are responsible of a number of phenomena, both in the offshore region, and in the nearshore region. In the former, tidal currents are responsible of the formation of sand banks (inclined with respect of the current, Van Rijn, 1998; Dyer & Huntley, 1999), sand waves (perpendicular to the stream, Langhorne, 1982) and sand ridges (parallel to the current, Stride, 1982; Colombini, 1993). In the transition towards the nearshore region, a typical feature is represented by the so called shoreface connected ridges (Antia, 1996; Trowbridge, 1995). In the nearshore region typical morphologies are: longshore (Roelvink & Broker, 1993; Zhang & Sunamura, 2011), crescentic (Vittori *et al.*, 1999; Falques *et al.*, 2000) and welded (Castelle *et al.*, 2007, figure 1.4*a*) bars and the so called "high-angle wave instability" (Ashton & Murray, 2006; den Berg *et al.*, 2011, figure 1.4*b*). Finally, very close to the shore, when a sandy bottom interacts with shallow waters, the oscillations of the flow induced by the propagating sea waves (Craik, 1971)

(a) (b)

(c)
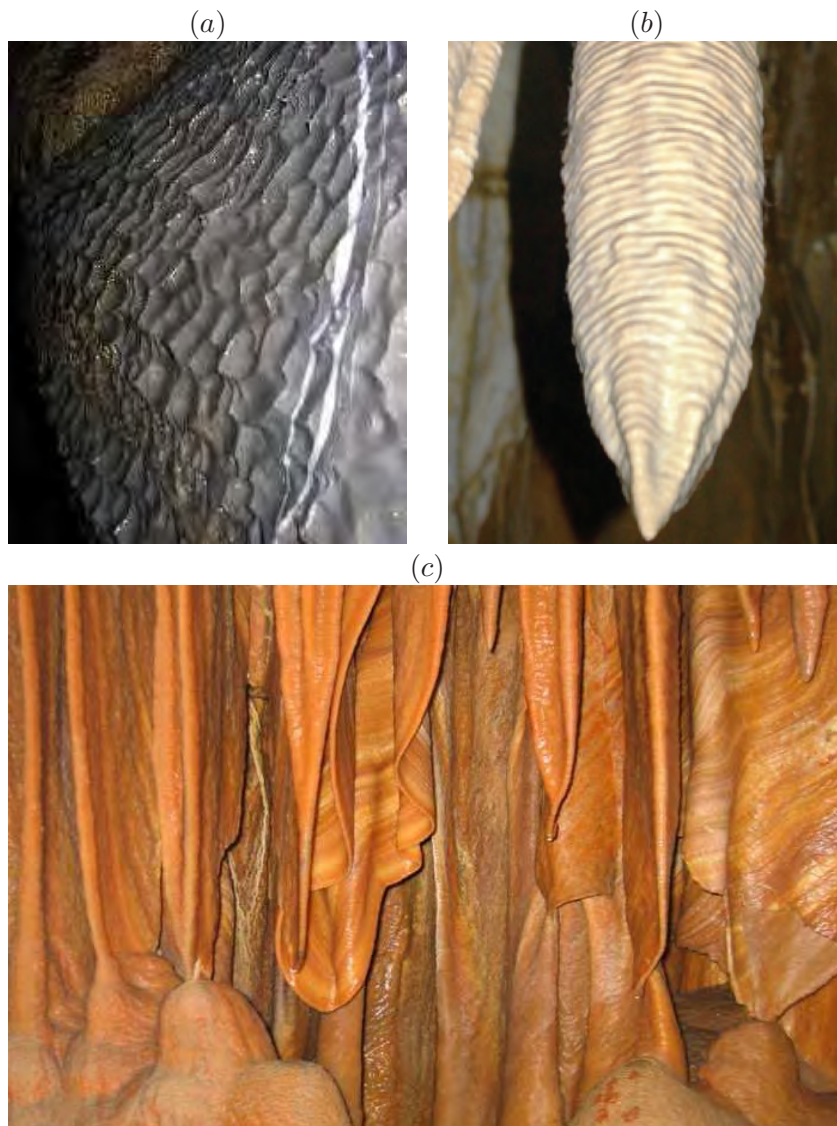
Figure 1.3. Morphologies generated by chemical dissolution and deposition processes in karst environment: (a) scallops; (b) crenulation over a stalactite and; (c) draperies on a vertical wall.

are responsible for the formation of ripples (Vittori & Blondeaux, 1990).

(a)

(b)
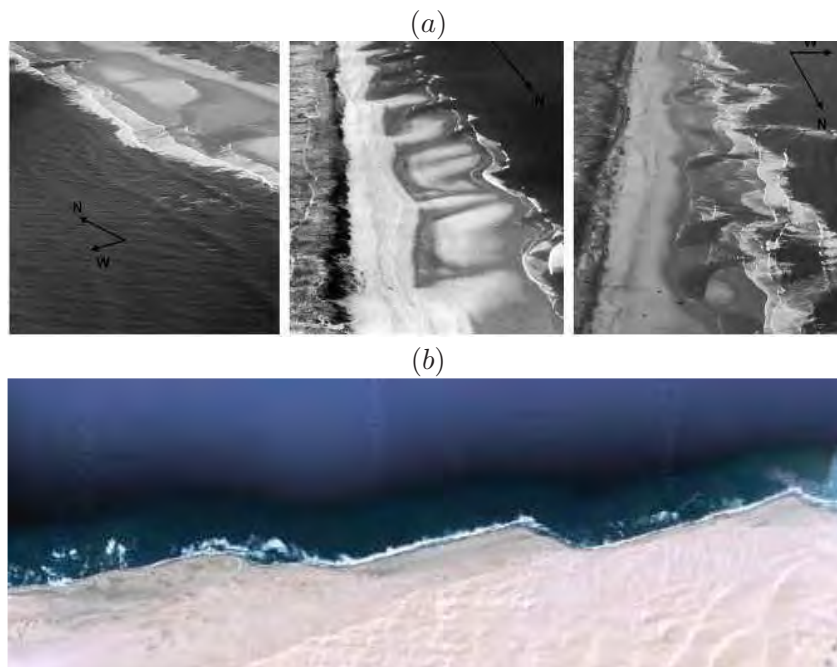
Figure 1.4. Morphologies generated by interaction between sediments and marine streams: (a) complex bar morphologies in the Aquitanian beaches, as reported by Castelle *et al.* (2007) and; (b) high-angle wave instability in Namibia.

The sand barriers coastline (figure 1.5a) is a very beautiful, fragile and extremely widespread environment (15% of World's coastline is made of sandbarriers, Beets & Van der Spek, 2000; Davis & Fitzgerald, 2004). The inlet system (figure 1.5b), in particular, is a formidable source of morphological mechanisms and processes (Ranasinghe & Pattiaratchi, 2003; Van der Vegt *et al.*, 2007). A first interesting issue is the analysis of the stability of the inlet itself. Its dynamics are the result of the competition between the stabilizing effects of wave currents (which tent to clog up the inlet by depositing sediments) and the destabilizing effect of the tidal currents (which promote the inlet widening by removing sediments, Tambroni & Seminara, 2006; Van de Kreeke, 1990). A second issue is the study of the complex morphologies of the inlet bottom, in which features resembling river bars and meandering

7

(*a*)

(*b*)
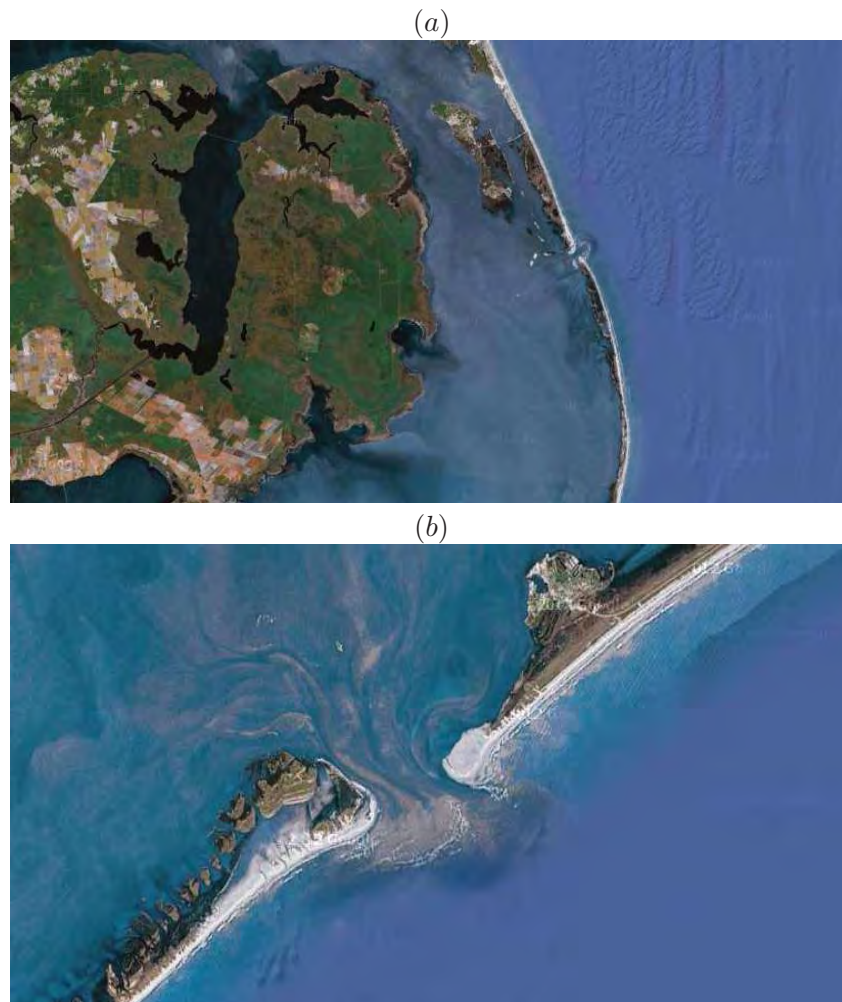
Figure 1.5.   Sand barrier coastline: (*a*) "The Outer Banks", North Carolina, USA, an outstanding example of sand barrier coastline and; (*b*) one of the inlet of "The Outer Banks" near Ocracoke North Carolina, USA.

often occur (Ahnert, 1960; Dalrymple & Rhodes, 1995). Other interesting phenomena are the formation of the complex network of channels responsible of the drainage of the water from the tidal basin (Schuttelaars & de Swart, 1999; Marciano *et al.*, 2005) and the formation of the ebb-tidal delta (Tambroni *et al.*, 2005), namely

the delta taking place seaward of an inlet, and formed by the sediment transported by the ebb-tidal current).

1.2   River morphodynamics

Rivers provide one of the greatest collection of morphodynamic phenomena. The nature of the processes can be very different, and their spatial and temporal scales can vary of several order of magnitudes, shaping the landscape with a sensational variety of patterns and posing tough problems in describing and analyzing the different mechanisms involved in such complexity.

The first, fundamental step necessary to understand the wide varieties of morphological processes occurring in rivers is to classify the type of phenomena. It can be an erosional, depositional or equilibrium process, if the capacity of the flow to carry sediments is higher, lower or equal to the equilibrium sediment rate, respectively (Seminara, 2010). Erosional processes are typical of the mountain zones, where there is plenty of sediment and water has a high potential energy (with respect of the sea level, Perron *et al.*, 2008). Typical morphologies caused by erosional processes are hillslopes (Willgoose *et al.*, 1991; Tucker & Bras, 1998, figure 1.6*a*) and meanders in rocks (Zeller, 1967). Depositional processes takes place whenever a reduction in flow velocity occurs, thus reducing the stream capacity of transport. The most widespread examples of depositional processes are fluvial deltas and alluvial fans (Parker *et al.*, 1998; Swenson *et al.*, 2000; Parker & Sequeiros, 2006, figure 1.6*b*). Erosional and depositional events, despite their importance and influence in human activities, are localized processes and their effects are usually important only at the head and at the mouth of rivers. As a result, researchers have more often been focused on equilibrium processes, namely the morphological dynamics which take place when the sediment supply is equal to the carrying capacity of the river (Seminara, 2010).

The second step useful to have a clearer vision of the wide range of phenomena related with river morphodynamics, is to classify the river morphologies according to their temporal and spatial scales (Seminara, 2010). We can distinguish between large, meso and small scale phenomena, respectively. Large scale morphologies are

(a)

(b)

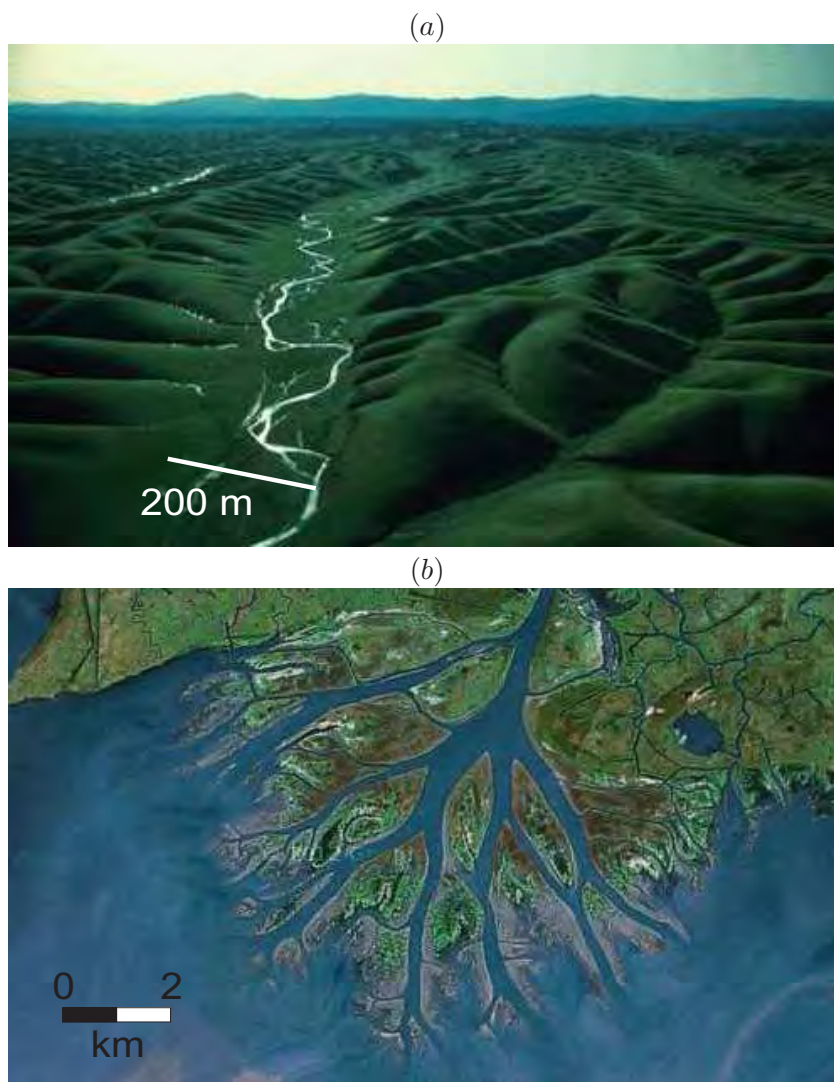Figure 1.6. Non equilibrium morphologies: (a) an erosional pattern consisting of a rhythmic sequence of valleys near Orland, California, USA (Seminara, 2010) and; (b) a depositional pattern consisting of the fluvial delta of the Wax Lake, Louisiana, USA (Seminara, 2010).

processes occurring at spatial scales of the order of many times the channel width, and are responsible of the planimetric evolution of

the river (Ikeda *et al.*, 1981; Zolezzi & Seminara, 2001; Seminara, 2006). Micro scale morphologies scale with the water depth and mostly affect the river bottom elevation and, consequently, the local flow depth (Best, 2005; Colombini & Stocchino, 2008). Meso scale bed forms scales with the channel width and, in this case, they are important both for the planimetric and for the bed elevation evolution (Blondeaux & Seminara, 1985; Colombini *et al.*, 1987; Colombini & Stocchino, 2012).

River meanders and braided patterns are examples of large scales morphologies (Ashmore, 1991; Parker & Johannesson, 1989). River meanders are one of the most original and ubiquitous pattern in fluvial morphology (figure 1.7*a*). A first condition for a straight reach to evolve into a meandering one concerns the slope of the alluvial plain in which the river flows. The slope has to be sufficiently small so that also the aspect ratio of the river is small (Engelund & Skovgaa, 1973). Under this condition, any deviation of the channel alignment from perfectly straight induces the presence of curvature, which, in turn, causes the near bank velocities at the inner bank and at the outer bank of the bend to be smaller and larger than the average flow velocity, respectively (Ikeda *et al.*, 1981; Parker & Johannesson, 1989; Zolezzi & Seminara, 2001). This, in turn, causes erosion of the outer bank and deposition in the inner bank (Camporeale *et al.*, 2007). This process deviates more and more the river centerline from the originally straight alignment. The lack of dumping factors able to limit the amplitude of the bends to a finite value, and the occurrence of cutoffs that locally reduce the river length and its sinuosity (Seminara *et al.*, 2001; Camporeale & Ridolfi, 2006) let the meandering process be an emblematic example of dynamical system far from equilibrium (Liverpool & Edwards, 1995; Stølum, 1996) affected by strong non-linearities and able to produce fascinating geometrical patterns.

Braided patterns (figure 1.7*b*) are also extremely widespread (Ashmore, 1982; Reinfelds & Nanson, 1993), and, differently from the meandering case, they develop only when the slope is sufficiently high so that the aspect ratio of the river is high, too (Engelund & Skovgaa, 1973). As a matter of facts, the mechanism governing the river braiding consists of the initial growth of central bars (or even higher-order bars) that generates a complex network of thalweg where the discharge is concentrated (Ashmore, 1991;

11

(*a*)

(*b*)

Figure 1.7. Examples of morphologies relevant for the planimetric evolution of rivers: (*a*) a meandering river and; (*b*) a braided river.

Hall, 2006). The concentration of the stream along some preferential directions (thalweg) concentrates the erosion as well, so that the depth of the channel at the thalwegs is increased, in this way

12

more water is concentrated in these zones and the mechanisms goes on as far as a dynamical equilibrium is reached (Ashmore, 1991; Ashmore *et al.*, 2011). In this way, the final shape of a braided pattern will be a number of islands emerging from a network of channel. The dynamics of the system are further complicated by the strongly nonlinear behavior of the stream, especially in the zones of flow bifurcation and merging occurring at the edges of the islands (Federici & Paola, 2003; Ashmore & Parker, 1983), and by the occurrence of bar cutoffs (Van Dijk *et al.*, 2012). The result is spectacular: especially in strongly braided rivers many different environments with peculiar flow characteristics can be observed, such as the main channels, where the discharge can be very high, and death zones, generated by the interplay between cutoff and bypass mechanisms, where water is basically at rest (Kemp *et al.*, 2000; Powell, 1998).

The most important micro-scale bed forms are: ripples, dunes, antidunes, cyclic steps, sand ribbons and streaks. Ripples, dunes (figure 1.8*a*), antidunes (figure 1.8*b*) and cyclic steps arise as an instability of the fluid sediment interface (Kennedy, 1963; Reynolds, 1965; Richards, 1980; Colombini, 2004).

The growth mechanism can be resumed as follows: a slight perturbation of the bottom generates perturbations also in the flow structure. Such perturbations influence the dynamics of the shear stress exerted at the bottom (Colombini, 2004) and, in turn, of the sediment flux (Kennedy, 1963). Depending on the hydrodynamic and sediemntological conditions, the bottom perturbation and the sediment flux perturbation are out of phase of some angle (Gradowczyk, 1970, figure 1.9). The actual value of this parameter is crucial (Hanratty, 1981), as it determines whether the initially small perturbation will grow (and evolve to a well defined pattern of mature bed forms) or decay; whether the perturbation will migrate upstream, downstream or will be stationary and, finally, the velocity at which all these processes occur (table 1.1).

The determination of the precise value of the phase angle, anyway, is not an easy task (Kennedy, 1963; Reynolds, 1965; Hayashi, 1970), as many different mechanisms contributes in phasing out bed elevation and sediment flux. For instance, it has been demonstrated that purely hydrodynamic mechanisms are sufficient for creating phase angles appropriate for the growth of bed forms

13

(a)

(b)

Figure 1.8. Examples of morphologies relevant for the evolution of the river bottom: (a) river dunes after a flood event and; (b) active antidunes.

(Colombini, 2004; Colombini & Stocchino, 2012), but mechanisms as important as particle inertia (Parker, 1975b), suspended sediment (Richards, 1980; Fredsøe, 1974), flow separation (Best, 2005),
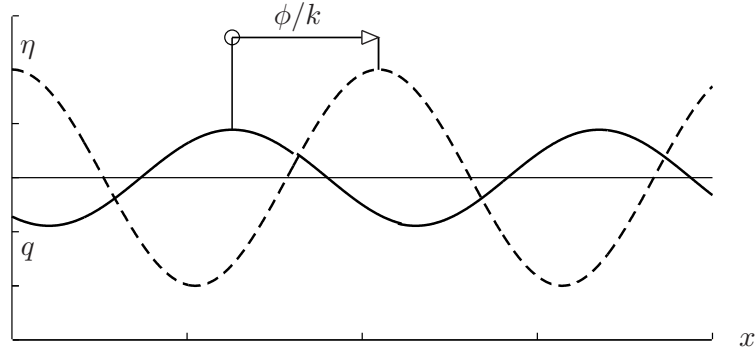
Figure 1.9. Phase between the solid transport perturbation q (continuous line) and the bottom perturbation η (dashed line). The phase is the ratio between the phase angle ϕ and the perturbation wavenumber k.

Table 1.1. Fate of an infinitesimal bottom perturbation as a function of its phase angle with respect of the solid transport perturbation. See figure 1.9 for the evaluation of the phase angle.

Phase angle	Amplitude evolution	Migration direction
$\phi = 0$	Constant	Downstream
$0 < \phi < \pi/2$	Growing	Downstream
$\phi = \pi/2$	Growing	No migration
$\pi/2 < \phi < \pi$	Growing	Upstream
$\phi = \pi$	Constant	Upstream
$\pi < \phi < 3\pi/2$	Decaying	Upstream
$\phi = 3\pi/2$	Decaying	No migration
$3\pi/2 < \phi < 2\pi$	Decaying	Downstream

gravity (Hayashi, 1970), saltation mechanisms (Charru *et al.*, 2013) and the disequilibrium between local erosion and deposition (Devauchelle *et al.*, 2010) contribute to a significant extent in defining the morphological dynamics of the fluid sediment interface. A further aspect which contributes to add complexity to the dynamics

15

of the river bottom evolution is the effect of the channel width (Best, 2005; Colombini & Stocchino, 2012). When the value of this last parameter is sufficiently high, two-dimensional bed forms (i.e., there is no variation of the bottom elevation along the coordinate perpendicular to the channel axis) may evolve in more complex morphologies, such as three dimensional dunes and antidunes (Best, 2005; Colombini & Stocchino, 2012). Finally, the evolution of the bed form is regulated by non linear mechanisms, such as the amplitude saturation and the pattern coarsening due to sand waves superimposition and amalgamation (Colombini & Stocchino, 2008). Sand ribbons are a very peculiar type of bed form which scales with the flow depth. They appear as regularly-spaced parallel streaks of sand aligned with the channel axis. The mechanism that allows for their growth is turbulence anisotropy (Colombini, 1993), which generates secondary flows able to sustain the growth of the sand-ribbon perturbations.

Finally, bars (figure 1.10) are an outstanding example of mesoscale bed forms. They are characterized by a regular sequence of rifles and pools, separated by a diagonal front and characterized by transversal and longitudinal scales of the order of the channel width, vertical scale of the order of the stream depth and slow downstream migration (Callander, 1969; Ikeda, 1982; Jaeggi, 1984). Their formation can be explained in terms of balance between the destabilizing effects of secondary flows induced by an early bottom unevenness and the stabilizing effect of gravity. As the magnitude of secondary flows is inversely proportional to the spacing between two bar units, while the stabilizing effect of gravity depends on the inclination of the lateral bar slope, it is clear that as the width-depth ratio is decreasing, the effect of gravity becomes more relevant (Federici & Seminara, 2003). Summing up, very narrow channels don't allow for bar formation while in wide channels also multiple rows of bars can form (Ashmore, 1982). Bars can be free and forced. Free bars (figure 1.10*a*) arise in straight or slightly curved rivers with a sufficiently high width-depth ratio with the mechanism just described. Forced bars arise from strong disturbing effects, such as channel curvature (Zolezzi *et al.*, 2005, figure 1.10*b*) or changing in river cross section (Repetto *et al.*, 2002, figure 1.10*c*).

16

(a)

(b)   (c)
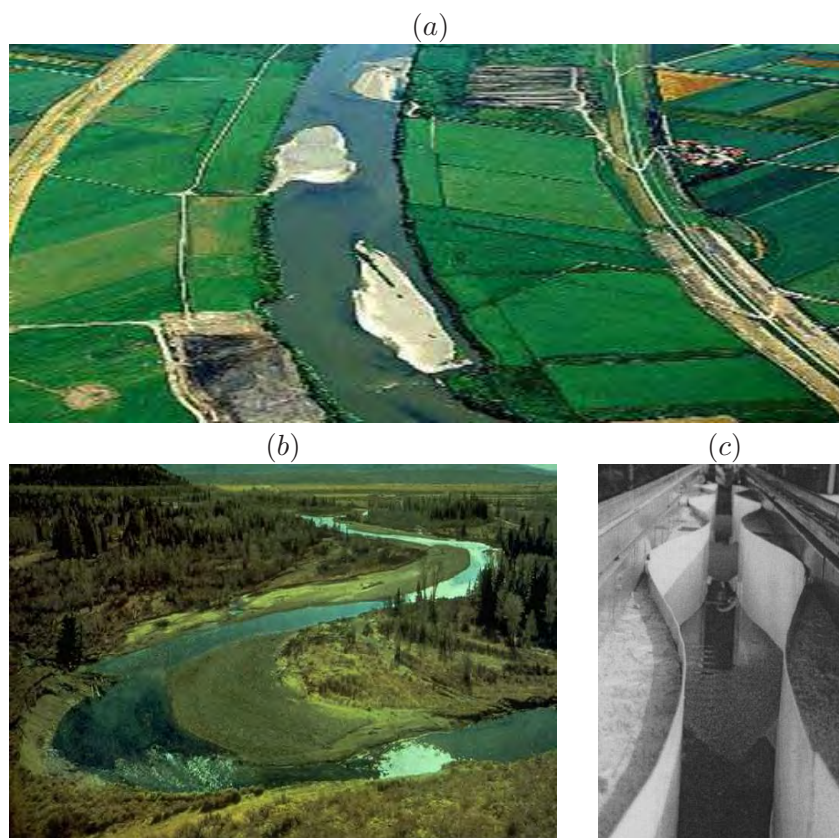
Figure 1.10. River bars: (*a*) free bars in a straightened reach of the Tokachi River, Japan; (*b*) point bar induced by the river curvature and; (*c*) experimental apparatus for the study of the forcing on bottom elevation induced by the changing of river cross section (Repetto *et al.*, 2002).

1.3 Practical and scientific implications

Besides speculative aspects related with the beauty and complexity of bed forms, understanding the processes occurring in rivers is also fundamental for the management and the safety of the human activities that develop along river banks (Amsler & Garcia, 1997; Ikeda, 1982), as well as for the preservation of the riparian environment (Tealdi *et al.*, 2011; Kemp *et al.*, 2000; Powell, 1998). Many books could be written for illustrating the interactions between

(a)   (b)
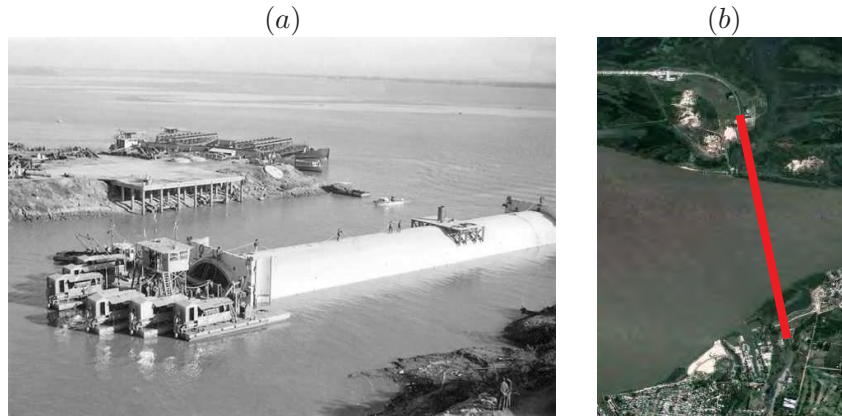
Figure 1.11. Infrastructures threatened by river morphological evolution, the case of the "Uranga and Sylvester Begnis" tunnel, near Paranà City, Argentina : (a) construction in 1968 and; (b) location of the tunnel, the north suburbs of Paranà City are visible in the bottom left corner of the panel.

morphodynamic processes, human activities and environment. In the following we will report some emblematic cases that illustrate well the importance of the topic and the potential consequences of a poor understanding of the problem considered.

The first example here reported is about the interaction between a river and a human infrastructure. In particular, the case of the "Uranga and Sylvester Begnis" underground tunnel built near the city of Paranà (Argentina) will be discussed (Amsler & Garcia, 1997). The mentioned tunnel (2.4 km long) was built in 1968 (figure 1.11a) where the Rio Paranà narrows to roughly 1.5 km in width (Amsler & Garcia, 1997; Best, 2005, figure 1.11b). The placement depth of the tunnel was determined from flow regime theory, so that a minimum cover thickness of 4 m was supposed to be guaranteed. During the floods occurred in 1983, 6.5 m high and 320 m long dunes formed and migrated through the river section were the tunnel was built. The large dunes caused the exposure of the tunnel to the flow, thus threatening its stability. In order to avoid the uplift of the structure, a large number of trucks full of sediment had to be parked inside the tunnel (Amsler & Garcia, 1997; Best, 2005).

Figure 1.12.   Navigation threatened by river morphological evolution, the case of the Rhine River: A Mainz, Germany; B Rhine River and; C Neckar River. The massive dunes formation begins in the reach just downstream of the confluence of the Neckar River in the Rhine River.

Morphodynamic processes may also interfere with river navigation (Harbor, 1998; Julien & Klaassen, 1995). An emblematic case is given by the Rhine River reach just downstream of Mainz (Germany), where the Main and Rhine River actually merge (Carling *et al.*, 2000b,a; Droge, 1992; Golz, 1990, figure 1.12). This reach is extremely important from an economic point of view, being part of the Rhine-Main-Danube Canal, an infrastructure in which every year 6.9 million tonnes of traffic volume are transported. Due to the complex sedimentological and hydraulic conditions (barrage 100 km upstream, inlet of sediments from the Main River and the Neckar River, sediment trap just upstream the Main River confluence), the 13 km long reach between Mainz and Bingen continuously develops big river dunes (height ~ 1.5 m for ~ 4 m water depth) which have to be constantly removed, for the barrage traffic to be guaranteed.

An other key issue is the protection of the land besides rivers and the protection against floods. It is well known and reported (Ikeda, 1982) that during the high population and economic growth occurred in Japan during the Sixties, many natural river was channelized and many meandering rivers straightened, in order to gain land for agricultural, industrial and civil purposes. As a result, in many channels alternate bars patterns developed, leading to bank

19

(a) (b)
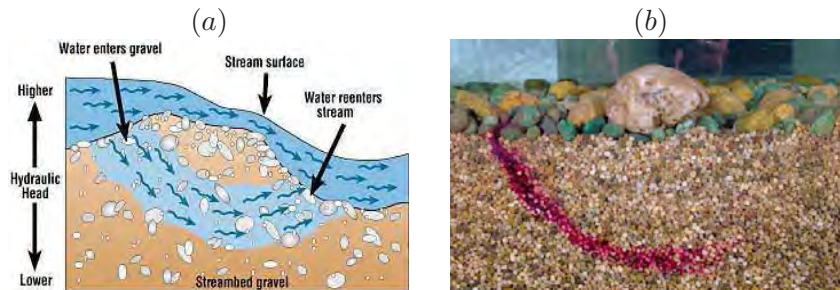
Figure 1.13. Hyporheic fluxes induced by river bedforms: (a) sketch of the problem and explanation of the role of bed forms in promoting hyporheic exchanges and; (b) visualization in an experiment of the hyporheic fluxes.

erosion, difficulties in navigation as previously reported, and to an increase of drag. The latter effect, in particular, caused the most tragic effects: as a result of the drag increase most of the channels were no longer sufficient for containing the flood peak discharge. A more current problem, instead, is the loss of land in Bangladesh (Ashworth *et al.*, 2000; Best *et al.*, 2003). The so called *within channel aggradations* linked to the growth of dunes and bars lead to the deviation of the flow from the channel axis, which is ultimately causing extensive bank erosion. The instability of the bank, in turn, is responsible of loss of infrastructures and agricultural land in a very poor and densely populated area.

River morphodynamic processes can also influence some phenomena apparently not linked, such as underground flows. The river deposits play a key role in the underground flows of many ancient sedimentary succession because they create anisotropic and heterogeneous permeability zones (Blom *et al.*, 2003; Kleinhans, 2004). As a result, preferential patterns are created, and the prediction of flows in hydrocarbon reservoirs or aquifers can be much complicated (Weber, 1986; Van de Graaff & Ealey, 1989). Ancient sedimentary deposits play also an important role in paleohydrology, i.e., the reconstructions of paleo-flow depths starting from the morphologies detectable in the sedimentary stratigraphy (e.g., dunes or antidunes height, Leclair, 2002; Shaw & Kellerhals, 1977).

Finally, river morphological processes have a huge impact for many environmental aspects. We here report only an exemplifying case of river-vegetation interactions and a brief summary about hyporheic exchanges. We will first analyze the effect on hyporheic exchanges. They consist in the mixing of the stream water and the pore water beneath the sediment bed (Thibodeaux & Boyle, 1987; Findlay, 1995). River bed forms promote hyporheic exchanges as they cause differential pressure gradients that generate flows within the sediments (Tonina & Buffington, 2007; Packman & Brooks, 2001, figure 1.13*a*). Such flows trap the fluids (and the relative chemical components dissolved) for a period that can be very long inside the sediments (Bayani Cardenas, 2008, figure 1.13*b*). The occurrence of hyporheic flows plays an important role, especially for what concerns the quality of the water and the nutrient cycling (Boulton *et al.*, 1998; Brunke & Gonser, 1997). As a matter of facts, the mixing occurring in the hyporheic zone between water rich of oxygen coming form the river and water rich of organic components coming form the groundwater, generates a unique environment in which rich communities of microbiota can flourish and many fundamental chemical reactions can occur (Hunter *et al.*, 1998; Bohlke *et al.*, 2009).

For what concerns the river-vegetation interactions we will briefly analyze the chain of feed backs between riparian vegetation and river morphology alterations (Gurnell & Petts, 2002, figure 1.14*a, b*). The riparian vegetation is a very dynamical system whose behavior is determined by a number of external (e.g., river discharge stochasticity, Tockner *et al.*, 2000, sediments characteristics, Steiger *et al.*, 2001) as well as internal (e.g., competition between species Tealdi *et al.*, 2013) factors. Changes in the river morphology (e.g., a transition from braided river to single thread river, a change in the average bed elevation due to erosion) ultimately alter the water table, and thus the water availability to the surrounding flora (Tealdi *et al.*, 2011). Moreover, the zones flooded during high discharge periods may also vary, leading the negative effects of high water level (e.g., erosion, anoxia Naumburg *et al.*, 2005) to act on wider portion of biomass. The loss of vegetation, moreover, reduces the soil resistance against erosion, making morphological changes faster and easier (Tealdi *et al.*, 2011). This quick glance at the problem shows how destructive slight alterations on the reached dynamical

(a) (b)

Figure 1.14. Effect of damming on the riparian vegetation: (*a*) picture of a reach of the Colorado River, California, USA, in natural discharge conditions (the upstream dam is under maintenance and there is no water retention) and; (*b*) Picture of the same reach reported in panel *a*, after damming. Note that in panel (*b*) vegetation is growing in previously submerged area, and that vegetation close to the water in panel (*a*) has now limited access to the water due to the reduction of the water depth in the river.

equilibrium can be. Moreover, studies on simplified models have tried to quantify these effects, and have indicated that slight morphological changes can reduce up to the 100% the total biomass (Tealdi *et al.*, 2011).

Observing the practical and technical importance of all the previously mentioned effects of morphodynamic processes, it is easy to understand that morphodynamics was born as an applied science. The first researchers involved in this topic had to provide engineers with simple rules for performing the difficult predictions of the river behavior and evolution (Ikeda, 1982; Jaeggi, 1984; Guy *et al.*, 1966). Anyway, many years of study of the morphological processes unveiled complex behaviors and dynamics that fascinated also the scientific world in and more speculative and academic way (Camporeale & Ridolfi, 2006; Federici & Seminara, 2003; Stølum, 1996). Among the many aspect that over the last years have interested scientists, some key issues are still posing intriguing questions to the researchers. In particular, the most studied theoretical topics are: (i) the interactions between the stream and the solid particles; (ii) the modeling of streams bounded by deformable and flow-dependent surfaces; (iii) the assessment and the analysis of the
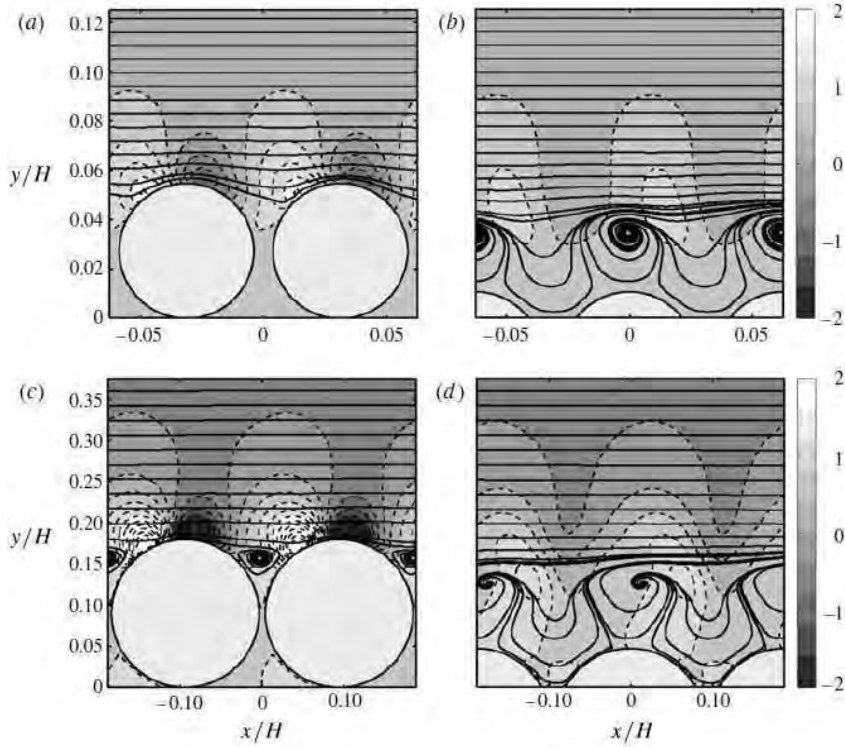
Figure 1.15. Results of a DNS used for the evaluation of forces and torques acting on a particle in a transitionally rough open channel flow (Chan-Braun *et al.*, 2011). In the panels is reported the time-averaged pressure field (dashed lines are iso-contour lines of pressure) and the corresponding stream lines (continuous lines).

stream-boundaries system stability and; (iv) the long term evolution of strongly nonlinear dynamical system.

For what concerns the stream-particles interactions the principal interests are the precise evaluation of forces and torques acting on the single particle (Chan-Braun *et al.*, 2011; Auton, 1987, figure 1.15). These analyses are actually a starting point in order to fully understand the sediment-stream interactions which ultimately drive the morphodynamic processes through the solid transport (Seminara *et al.*, 2002; Parker *et al.*, 2003). A wide body of literature exists on the evaluation hydrodynamic forces induced on spherical objects: both in the low-Reynolds-number range, for

which analytical (Saffman, 1965; Auton, 1987) experimental (King & Leighton, 1997) and numerical (Lee & Balachandar, 2010) studies have been performed, and in the high-Reynolds-number limit (Yun *et al.*, 2006). Considering the modeling of solid transport, over the last decade a switching towards a mechanistic approach for the study of this topic occurred (Seminara *et al.*, 2002; Parker *et al.*, 2003; Luque & van Beek, 1976). Many recent works have considered sediment transport no longer a steady process (as was done by Colombini, 2004) in which the solid rate is empirically evaluated directly from the flow characteristics. On the contrary, the sediment transport is seen as the dynamic equilibrium resulting from the competition between local erosion and deposition of particles (Nino *et al.*, 1994; Lee & Hsu, 1994; Sekine & Kikkawa, 1992; Luque & van Beek, 1976). Moreover, in order to evaluate the solid rate, the aerial concentration of particle in motion and their velocity is computed with a physically based approach (Devauchelle *et al.*, 2010; Charru *et al.*, 2013). To this end, the forces acting on the single particles are evaluated and the momentum exchanges between the stream and the sediment particles are considered (Seminara *et al.*, 2002; Parker *et al.*, 2003).

Also the modeling of open channel streams is a topic far from been completely understood and solved, and poses a number of computational (He & Seddighi, 2013; Zang & Krist, 1989) and conceptual (Colombini & Stocchino, 2012; Balmforth & Vakil1, 2012) issues. The research on this branch is divided roughly in two categories: on one side, powerful numerical tools are adopted in order to solve the Navier Stoke's equations (DNS approach, Moin & Mahesh, 1998), on the other side, simplified models are developed for facing a particular problem. The DNS approach provides the solution of the full flow field (He & Seddighi, 2013; Zang & Krist, 1989), with these data, important results about the structure and the statistics of turbulence in open channel flows (Kim *et al.*, 1987), such as turbulence intensities, vorticity fluctuations, Reynolds stresses, and energy spectra can be obtained. Closure models for the dissipation rate of the Reynolds normal stresses can also be tested using the results from DNS simulations. The recent advances in the simulation of transient flows have also clarified the role of flow unsteadiness in promoting the creation of particular

24
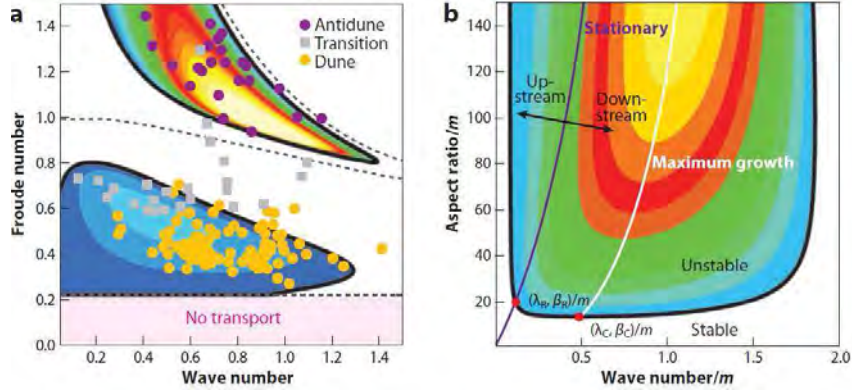
Figure 1.16. Results of linear stability analysis for the study of the stream-bed interface instability (Seminara, 2010). In the panel on the left: a dune instability plot. The unstable regions in the Froude-number versus wave-number space are compared with observations. In the panel on the right: a unified marginal stability curve for bars of any (transversal) mode.

structures (Jeong & Hussain, 1995; Chung, 2005), which may ultimately contribute in explaining peculiar behaviors of the fluids that not always occur in steady flows (Ricco *et al.*, 2011). The development of simplified models (e.g., turbulence averaging (Fredsøe, 1974; Engelund, 1970) and depth averaging (Dressler, 1978; Luchini & Charru, 2010)), still able to describe some important physical aspects (e.g., eddy viscosity, bottom curvature), has proven to be fundamental for the study of river morphodynamic processes for their analytical and mathematical tractability (Richards, 1980; Colombini & Stocchino, 2012).

Scientists have been fascinated also by the study of the stream-boundaries interface stability (Federici & Seminara, 2003; Camporeale & Ridolfi, 2006; Lanzoni & Seminara, 2006) because of the complex nature of this system (Stølum, 1996), which develop, under different flow conditions (Colombini, 2004; Colombini & Stocchino, 2008, 2012), spatial (Colombini & Stocchino, 2011) and temporal (Camporeale & Ridolfi, 2011, 2009) scales, extremely different and complex behaviors. As reported also by Seminara (2010), "*the interface separating the fluid from the adjacent erodible medium is a free boundary, in which the exchange of sediment particles between*

the two media is allowed". The emblematic behavior, anyway, is that sediment waves arise spontaneously from an instability of the bed interface itself, and not driven by flow instability (Kennedy, 1963; Reynolds, 1965, figure 1.16).

Finally, morphodynamic processes have attract much interest because they often exhibit an asymptotic behavior far from equilibrium, in which self-organized criticality (Furbish, 1991; Stølum, 1996, 1997), fractal geometry (Snow, 1989; Nikora *et al.*, 1993; Stølum, 1998) and statistical equilibrium (Howard, 1992; Liverpool & Edwards, 1995; Sun *et al.*, 1996; Stølum, 1996, 1997) can be observed. An example is given by meandering rivers. They can be thought as planar curves which evolve under two contrasting forcings: a continuous elongation driven by the differential bend erosion, and sporadic shortenings induced by cutoff events. The continuous elongation that generates new reaches provides the dynamics with spatial memory and induces a sensitivity to initial conditions typical of locally (spatially or temporally) unstable systems (Argyris *et al.*, 1994). The sporadic cutoffs are intermittent and eliminate the most mature meanders when two distinct river bends try to overlap (Gagliano & Howard, 1984). Moreover, this sequence of phases (elongation and shortening), which represents the key dynamics of the long-term evolution of meandering rivers, is forced by several external factors, some of them also with stochastic variability, such as: riparian vegetation, flow variability, anthropic actions , and geological processes (Sun *et al.*, 1996; Camporeale *et al.*, 2005).

1.4 Open problems and contributions of the thesis

In spite of the remarkable efforts and progresses in the modeling and understanding of the dynamics of river morphologies, some features are still not understood. One of the most fascinating and unexplored aspect is the inception of bed forms and their evolution at initial stages. The bed forms inception concerns the transient dynamics occurring from the very preliminary stages of the bed instability up to the definition of a well-formed bed form. Experiments and theory haven't focused often in this aspect, but the

available data show very intriguing behaviors (Fujita & Muramoto, 1985; Lanzoni, 2000; Coleman & Melville, 1996). For many morphologies (e.g., bars, dunes) it is common to observe the formation of early bed forms characterized by a short wavelength. These early bed forms then merge together with complex processes of amalgamation, generating longer waves. Consequently, it is possible to observe a progressive increase of the dominant wavelength, until an asymptotically stable wavelength is reached. We have been inspired by these experimental findings to investigate the bed forms inception dynamics. In particular, in chapter 2, we have focused on alternate bars: regular bed forms characterized by vertical and transversal scales that are comparable with the stream depth and width, respectively. Bars are widespread in rivers and play a crucial role in a number of engineering and environmental problems. Well established mathematical models exist, and linear and weakly nonlinear stability analysis have been performed. However, none of the mentioned approaches has been decisive in explain the rich and beautiful dynamics of the inception phase. In order to shed light on the transient dynamics we have tackled the problem as an initial boundary problem rather than the usual eigenvalue problem. This has allowed us to follow a non-normal approach, and to demonstrate a strong nonnormality in the operator governing bar dynamics, in large regions of the parameter space. This entails the existence of strong transient growths in the evolution of bed perturbations. Our work has been completed by performing new experiments for a more complete understanding of the inception phase of alternate bars. By interpreting the results of our new experiments as well as those available in literature with the results of our theory, we explain the progressive increase of the dominant bar wavelength through a purely linear process triggered by the system nonnormality.

An other current topic concerns the study of the instability of the water stream – sediment bed interface. Among others (Best, 2005; Charru *et al.*, 2013), two issues are particularly relevant: (i) the clarification of the role of the sediment transport in promoting or damping these bed-interface instabilities and; (ii) to develop a depth average model for the study of dunes and antidunes. This in particular is extremely useful for the analysis of the nonlinear

27

behavior of such bed forms. Over the last years, the fluid dynamics of a stream over dunes and antidunes have been modeled using either irrotational (Kennedy, 1963; Reynolds, 1965; Hayashi, 1970) or rotational (Engelund, 1970; Fredsøe, 1974; Colombini, 2004) 2D models. Very recently the linear stability of the fully 3D problem has also been proposed (Colombini & Stocchino, 2012). Therefore, it is commonly assumed that the simplest hydrodynamic model that is able to predict antidunes has to be at least two-dimensional. The use of a two (or three) dimensional model for the description of the dynamics of the fluid phases, despite providing very good predictive results, causes a number of difficulties in the analytical and computational handling of the problem. As a result, a number of very key issues fundamental for the interpretation of numerical and experimental results as well as field observations, such as the nature (absolute or convective) of the bed form instability, the nonlinear dynamics of the bed forms, the nonlinear interactions between free surface and bed instability and many others could not be answered yet. In order to overcome the limitations given by the complexity of 2D models, in chapter 2, a novel linearly theory for antidunes is proposed. The morphodynamic model is obtained by coupling 1D shallow-water (Dressler's) equations with a mechanistic sediment transport formulation. In spite of some simplifications in the modeling of the fluid phase, the physical mechanisms required for the inception of the instability and for the selection of the dominant wavelength are preserved. The second key point of the chapter concerns the sediment transport modeling. The common simplifications of equilibrium conditions (no aggradation or erosion) and uniform flow adopted in empirical sediment transport formulas are relaxed. In the sediment transport modeling, we do not assume any equilibrium conditions (between local entrainment and deposition processes) or uniform flow, and adopt a mechanistic approach. It is based on the the momentum exchange between the fluid and the sediment and on the (space- and time-dependent) balance of the forces acting on the sediment particles (Seminara *et al.*, 2002; Parker *et al.*, 2003). Such an approach allows the sediment transport to be evaluated from the competition between the local entrainment and deposition processes. We will finally make use of the analytical tractability of the 1D modeling and we will elucidate the key physical processes which drive antidune instability. Finally

we will demonstrate the absolute nature of the antidune instability.

A final remark is about the notations adopted in the following chapters. In order to facilitate the reader which is interested in comparing the results presented in this thesis with the literature already available, we have adopted for each argument (and therefore for each chapter) the typical notations used for the topic. Therefore, in each chapter all the symbols and notation will be defined, and the meaning of symbols may vary in different chapters. Anyway, in order to facilitate the reader, a list of symbol valid for each chapter is provided in Appendix E.

Chapter 2

Nonnormality and wavelength selection in bar dynamics

Among the remarkable variety of patterns generated by the interaction between a water stream and an erodible bed, in this chapter we focus on alternate bars. Bars are regular bed forms characterized by vertical and transversal scales that are comparable with the stream depth and width, respectively. They are widespread in rivers and play a crucial role in a number of engineering and environmental problems. Well established mathematical models exist and linear and weakly nonlinear stability analysis have been performed. However, no nonmodal analysis has yet been proposed. With this new approach, in this chapter we demonstrate the strong nonnormality of the operator governing bar dynamics in large regions of the parameter space, entailing the existence of strong transient growths in the evolution of bed perturbations. We also present the results of new experiments devoted to understand the inception phase of alternate bars. Finally we explain the progressive increase in the dominant bar wavelength that can be observed in experiments through a purely linear process, without invoking nonlinear mechanisms.

2.1   Introduction

In the wide range of scales exhibited by river morphodynamics we here focus on bars. An example of bars emerging in a reach of the Rheine river as well as in laboratory flume are shown in figure 2.1. Bars are three-dimensional perturbations of the sediment bottom, characterized by a regular sequence of riffles and pools separated by a diagonal front (see figure 2.1*b*). Two consecutive diagonal fronts delimit a bar unit. Bars have a transversal scale of the order of the channel width and a longitudinal scale that is roughly six times the channel width. They migrate slowly downstream and their vertical scale is of the order of the stream depth. Bars can be both free and forced (Seminara & Tubino, 1989): the former arise spontaneously in a uniform stream with a flat bed and are triggered by a morphodynamic instability, while the latter are due to external forcing, such as channel curvature or stream cross-section changes. In this chapter, we will concentrate on free bars.

(*a*)

(*b*)

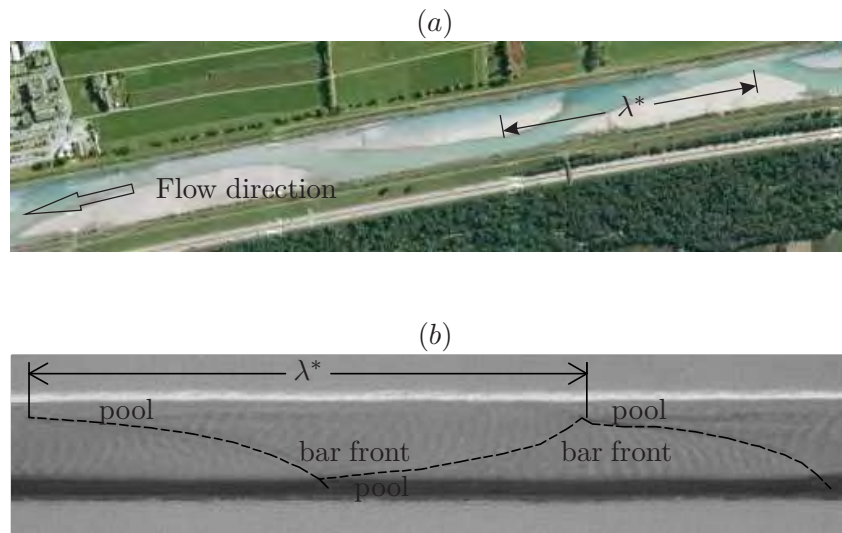Figure 2.1.   Panel (*a*): an alternate bar pattern in the Rheine river, nearby Vaduz, Liechtenstein (47º06'40"N, 9º31'02"E). The bars emerge in an artificially straightened reach of river. The picture is taken from Google earth. Panel (*b*): an alternate bar pattern obtained in a flume experiment. The pools and the bar fronts (dashed line) are highlighted. The bar unit wave length, λ^*, is shown in both pictures.

Bars are ubiquitous in rivers and are important for a number of reasons. In fluvial morphodynamics, they play a crucial role in the triggering of meandering and braiding patterns (Lewin, 1976; Parker, 1976; Blondeaux & Seminara, 1985) and, in general, drive localized bank erosions (Visconti *et al.*, 2010). Bars have an impact on the river conveyance of water, sediments and ice, and interfere with navigation, fishery and water supply. The modeling of bar dynamics is therefore fundamental in the design of fluvial structures, such as bank protections and bridges. Bars are also important for river ecology: they interact with the fluvial biotic processes to a great extent (Brown, 1997; Ward *et al.*, 2002; Gilvear & Willby, 2006; Marzadri *et al.*, 2010) and induce hyporheic fluxes that are responsible for exchange processes between stream and bed sediments (Jones & Mulholland, 2000).

The early theoretical works on the dynamics of bars used the linear stability theory (Callander, 1969; Parker, 1976; Fredsøe, 1978; Olesen, 1983; Blondeaux & Seminara, 1985) and explained bar formation as a morphological instability of the water-sediment interface, controlled by the balance between the destabilizing action of secondary flows induced by bed forms and the stabilizing action of gravity. The main results of these works concerned the dispersion relation and its dependence on the parameters of the physical problem. The Shields parameter and the width-depth ratio, in particular, play key roles; thus, very narrow channels do not develop bars, while alternate bars can arise in larger channels and multiple rows of bars can be observed in wide channels. In order to describe the saturation process, due to nonlinearities, and to make the evaluation of bar wavelength and migration celerity more precise, different weakly nonlinear theories, developed in the neighborhood of critical conditions, have been proposed (Colombini *et al.*, 1987; Fukuoka, 1989; Schielen *et al.*, 1993). These works elucidated the role of nonlinear mode competition and the possible instability of the periodic alternate bar pattern. In the last few years, Federici & Seminara (2003) have demonstrated the convective, rather than absolute, nature of bar instability, while Hall (2004) has investigated the effect of flow unsteadiness, and observed the ability of periodic flows to fix bars. He also described the effects of non-parallelisms on the river bottom stability (Hall, 2005). Very recently Colombini

& Stocchino (2012) have developed a comprehensive 3D linear theory of bed forms, elucidating the competition between 2D dunes, 3D dunes, diagonal bars and alternate bars. Two aspects shared by all the previously theoretical studies are worth stressing: (i) the flow field is assumed to adapt instantaneously to the bed evolution. This is the so-called quasi-steady hypothesis and it allows one to omit the time derivatives in the flow equations; (ii) disturbances do not change the wavelength during their evolution.

The role of the full non-linearities has been investigated by means of numerical methods (Nelson & Smith, 1989; Colombini & Tubino, 1991; Defina, 2003) which show the impact of the initial conditions and the occurrence of strongly nonlinear interactions. Moreover, experimental research (Chang *et al.*, 1971; Ikeda, 1982; Fujita & Muramoto, 1985; Lanzoni, 2000) has proved to be fundamental to describe the complexity of bar dynamics and to provide data to test model outcomes.

In spite of these remarkable efforts and progresses, some features of bar dynamics are still not understood. One of the most fascinating and unexplored aspects concerns the transient dynamics from the very preliminary stages of the bed instability to the emergence of the typical wavelengths of well-formed bars. Experiments have rarely focused on this aspect, but the few available data depict non trivial behaviors (Fujita & Muramoto, 1985; Lanzoni, 2000). Figure 2.2 refers to one of the first laboratory studies on bars and shows that short wave bed forms are dominant during the initial stage of bars formation. They then tend to decay and merge with longer waves. Consequently, it is possible to observe a progressive growth in the dominant wavelength, until the asymptotic one emerges and becomes stable. Some conjectures and numerical works suggest that this wave amalgamation process is due to nonlinear effects (Nelson & Smith, 1989; Defina, 2003; Wu *et al.*, 2011), but no decisive quantitative explanation has ever been given and the wavelength selection process remains an open question (Lanzoni, 2000).

We were inspired by these experimental findings to investigate bar dynamics from a different point of view, with respect to the usual stability analysis, in order to shed light on transient bar dynamics before asymptotic behaviour is attained. More precisely, we have tackled bar dynamics as an initial boundary problem rather
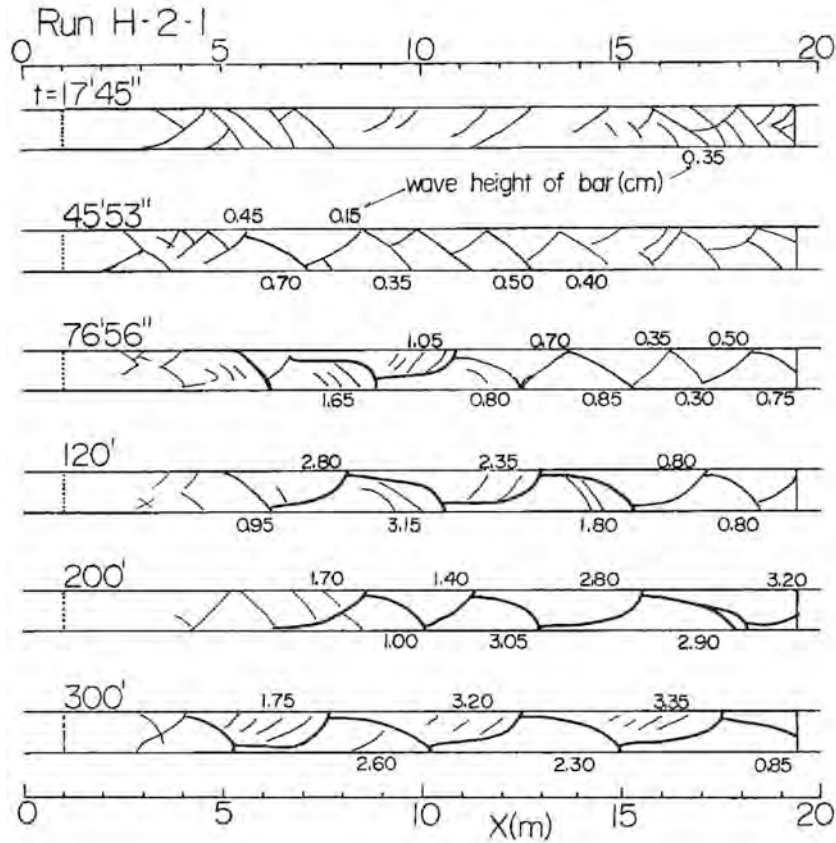
Figure 2.2. Time evolution of bar wavelengths, as reported in the experiments by Fujita & Muramoto (1985). The time the sketch of the bottom refers to is reported in the top left corner of each panel.

than the usual eigenvalue problem. This has allowed us to follow a non-normal (or nonmodal) approach, to demonstrate the existence of strong transient growths and to give a (quantitative) alternative explanation of wave amalgamation, based on only linear processes.

Asymptotic linear stability analysis is a powerful mathematical tool that has been extensively used in fluid mechanics for a century. Its steps are well-known: an infinitesimal periodic perturbation of the basic state is introduced in the differential equations system – in our case, the shallow water equations and the Exner equation – that governs the dynamical system; the perturbed system is then

linearised, solved, and the dispersion relationship that relates the growth factor to the wavenumber vector is obtained. The zero growth factor condition allows one to obtain the neutral (marginal) stability condition as a function of the problem parameters and to discern stability and instability regions.

The main feature of such an approach is that it focuses on the asymptotic temporal fate of the disturbances (i.e., for $t \to \infty$). However, no information is gained on the behaviour of the system at finite times and, in particular, the stability of the system is evaluated regardless of the way the disturbance tends to zero. Three emblematic qualitative temporal evolutions of perturbation are shown in the left panel of figure 2.3. The analysis of asymptotic behaviour by means of eigenvalues allows the stable cases A and B (the perturbation decays to zero for $t \to \infty$) to be distinguished from the unstable case C, where the disturbance tends to diverge. However, curves A and B exhibit very different behaviour for finite times: while the perturbation in system A decays monotonically to zero, it shows a transient growth in system B. The mathematical reason of this non-monotonic behaviour lies in the nonnormality of the differential (or algebraic) operator which governs the perturbation temporal evolution. This aspect is illustrated in the right panel of figure 2.3 for a simple two-dimensional algebraic problem: the non-orthogonality of the eigenvector set entails that, although all the eigenvalues are negative and single eigenvectors decay monotonically in time, their resultant experiences a transient growth. As disturbances can be written as linear combinations of eigenvectors, non-orthogonality causes disturbances to experience transient growths similar to case B shown in figure 2.3, and the stronger the nonnormality the more remarkable are the transient growths.

From the previous picture, it emerges that although the long-term asymptotic fate of the system is correctly driven by the least stable mode, the eigenvalue analysis is not a good descriptor of the transient behaviour of the fluctuations when eigenvectors do not form an orthogonal set. This explains why the concept of non-orthogonality of the eigenvectors is so closely related to the existence of transient growths in the stability analysis.

The difference between monotonic and non-monotonic temporal perturbation dynamics is not a mere mathematical detail, but is fundamental for several reasons. Firstly, the transient growth
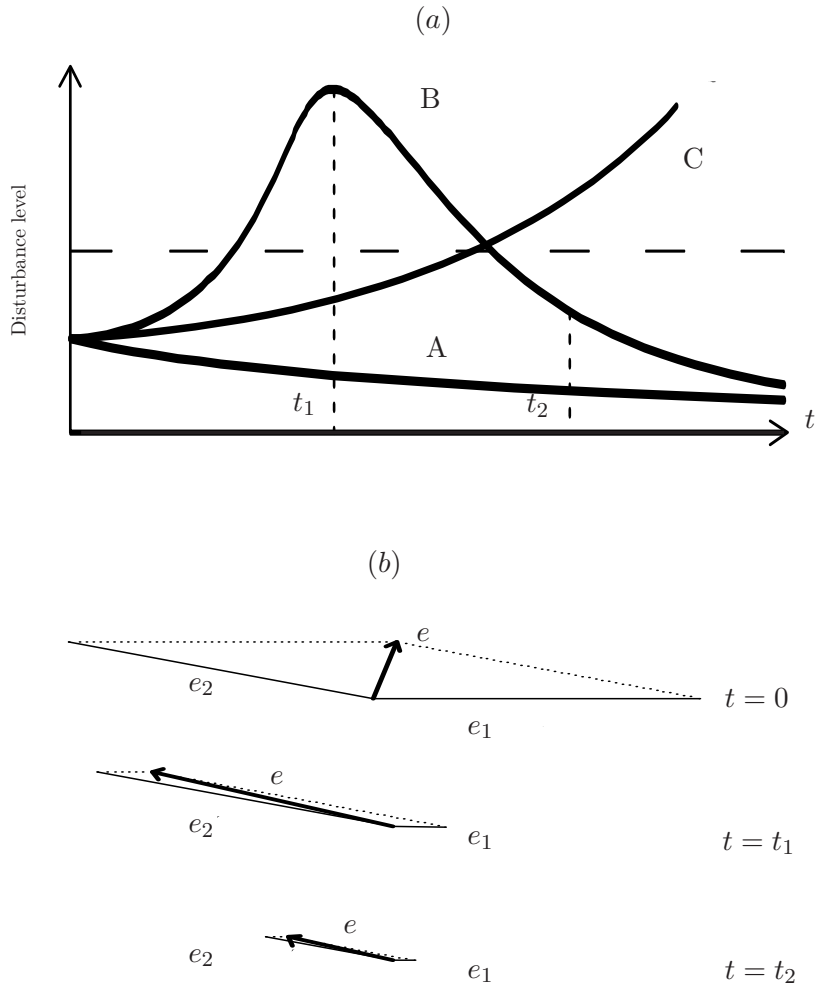
Figure 2.3. Three possible linear evolutions of an initial, infinitesimal perturbation are reported in the panel (a): monotonic asymptotic decay (A), transient growth before asymptotic decay (B), and monotonic indefinite growth (C). The dashed line indicates a schematic possible threshold of the perturbation amplitude beyond which nonlinear terms start to be non negligible. Panel (b) refers to a two-dimensional perturbation dynamics, where the non-normality of eigenvectors causes a transient growth: even though both eigenvectors, e_1 and e_2, decay in time, their non-orthogonality leads the norm of the resultant to be larger at time t_1 with respect to $t = 0$ and $t_2 > t_1$ (Schmid, 2007).

can trigger nonlinear instabilities. Therefore, although the problem would be asymptotically stable according to a normal mode analysis, it could result unstable because the disturbances amplify (linearly) to such an extent that they make the nonlinear terms significant (e.g., the dashed line in figure 2.3 is overcome). This process – called by-pass transition (Rempfer, 2003; Lee & Wu, 2008) – has been invoked in shear flow stability to explain the discrepancies between experimental results and analytical forecasts by means of normal modes (Trefethen *et al.*, 1993). The second key point is that transient growths can occur at time scales that are comparable with those of interest for the study of the process; as a result, the system appears unstable, although disturbances decay over much longer time scales. Thirdly, the characteristics of transient growths (timescales, growing rate, etc.) can depend to a great extent on the perturbation wavenumber; it is therefore possible that, during the first stages of perturbation evolution, the system exhibits temporarily growing disturbances with wavelengths that are also very different from the asymptotically unstable ones. Finally, this type of transient amplification of the initial disturbance is due to linear mechanisms and no nonlinear mechanism has to be invoked.

Over the last two decades, the nonnormal approach has been applied successfully in a growing number of scientific topics (Trefethen & Embree, 2001) and, in particular, in fluid mechanics (Schmid, 2007), where this approach has elucidated the role of linear mechanisms on the triggering of instability in simple shear flows (e.g. Reddy & Henningson, 1993; Olsson & Henningson, 1995; Malik & Hooper, 2007). In the field of morphodynamic problems, first applications were proposed by Camporeale e Ridolfi and concerned the de Saint-Venant-Exner model (Camporeale & Ridolfi, 2009) and the fluvial dune formation problem (Camporeale & Ridolfi, 2011). They demonstrated that nonnormality is ubiquitous in morphodynamics and that significant transient growths are expected to occur in the dynamics of one-dimensional long bed waves and in those of river dunes. This chapter is aimed to proceed further in the exploration of transients in morphological processes, in particular we expect: (i) to analytically show that the operator describing the bar dynamics is characterized by a high nonnormality in significant regions of the parameter space, (ii) to show that strong transient growths of bed perturbations are possible, and

(iii) to demonstrate that the progressive growth of the dominant wavelength observable before the asymptotic state is attained, can be ascribed to nonnormality and therefore explained by linear processes. For this last purpose, new experimental results that were collected paying particular attention to the initial transitory will be used. As the classical eigenvalue problem is embedded in the more general initial boundary problem, the study of the latter will also offer the opportunity of evaluating how the quasi-steady assumption (that is typical of the morphodynamic studies) affects the asymptotic stability analysis.

This chapter is organized as follows. The mathematical model of bar dynamics is recalled in section 2.2, where the perturbation energy is defined and the corresponding differential model is obtained. The eigenvalue problem is then solved, the impact of quasi-steady assumption is discussed, and the asymptotic stability of the free surface is analyzed, too. The nonmodal approach is developed in section 2.3 and the existence of strong transient growths in bar dynamics is shown. The effects of transient growths in the time evolution of bars wavelengths are discussed in detail in section 2.4, where the theoretical results are compared with experimental data collected for this study. Finally, the main conclusions are drawn in section 2.5.

2.2 Formulation of the problem

2.2.1 Mathematical modelling

The dynamical system considered in this study is a straight free-surface turbulent water stream flowing on a cohesionless bed of uniform granular material. The fluid is incompressible and the flow is bounded laterally by fixed and impermeable walls. The sediment motion is supposed to be only driven by bed-load mechanisms (saltation, rolling or sliding of particles in a layer as thin as two-three particle diameters), while suspended sediment transport (entraining of sediment particles in the bulk of the stream) is assumed negligible.

The channel (see figure 2.4) is $2B^*$ wide and the water depth is D^* (the star indicates dimensional quantities). An orthogonal reference system $\{s^*, n^*, z^*\}$ is set. The longitudinal coordinate s^*

(a)

(b)
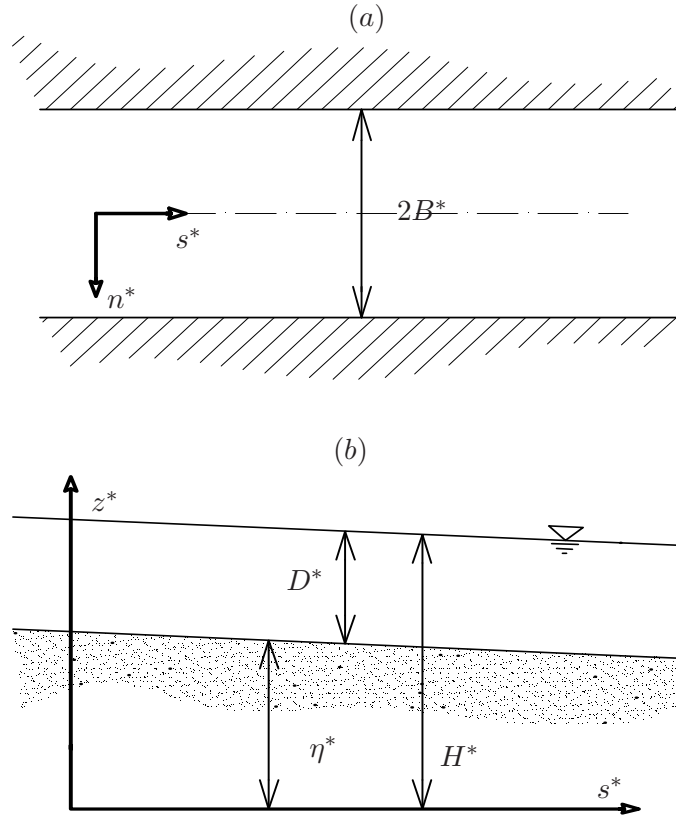
Figure 2.4. Panel (a): plane view of the channel. Panel (b): longitudinal cross section of the channel. The reference system and the main geometrical variables involved are displayed.

and the transversal coordinate n^*, with origin on the channel axis, lie on a horizontal plane, while z^* is vertical and points upwards. The bed elevation η^* and the free-surface elevation H^* are defined with respect to the $\{s^*, n^*\}$ plane, while $D^* = H^* - \eta^*$ is the local stream depth.

Shallow water equations and the Exner equation (Blondeaux & Seminara, 1985; Colombini *et al.*, 1987; Federici & Seminara, 2003) are commonly adopted for describing bar dynamics. This is justified if we assume the channel width to be large compared to the flow depth and noticing that bars exhibit wavelengths significantly larger than $2B^*$. If the quantities are made dimensionless by the

following relations (Colombini *et al.*, 1987)

$$(U^*, V^*) = U_0^* (U, V), \quad (H^*, D^*) = D_0^* (F_0^2 H, D), \quad (2.1a,b)$$
$$(s^*, n^*) = B^* (s, n), \quad (\tau_s^*, \tau_n^*) = \rho U_0^{*2} (\tau_s, \tau_n), \quad (2.1c,d)$$
$$(Q_s^*, Q_n^*) = d_s^* [(\rho_s/\rho - 1) g d_s^*]^{1/2} (Q_s, Q_n), \quad (2.1e)$$
$$t^* = B^*/U_0^* t, \quad (2.1f)$$

the mathematical model reads

$$\frac{\partial U}{\partial t} + V \frac{\partial U}{\partial n} + U \frac{\partial U}{\partial s} + \frac{\partial H}{\partial s} + \beta \frac{\tau_s}{D} = 0 \quad (2.2)$$

$$\frac{\partial V}{\partial t} + V \frac{\partial V}{\partial n} + U \frac{\partial V}{\partial s} + \frac{\partial H}{\partial n} + \beta \frac{\tau_n}{D} = 0 \quad (2.3)$$

$$\frac{\partial D}{\partial t} + \frac{\partial (UD)}{\partial n} + U \frac{\partial (VD)}{\partial s} + \Pi \frac{\partial (F_0^2 H - D)}{\partial t} = 0 \quad (2.4)$$

$$\frac{\partial (F_0^2 H - D)}{\partial t} + Q_0 \left(\frac{\partial Q_s}{\partial s} + \frac{\partial Q_n}{\partial n} \right) = 0, \quad (2.5)$$

where U and V are the depth-averaged fluid velocity components in the longitudinal and transversal direction, respectively, $\beta = B^*/D^*$ is the aspect ratio, τ_s and τ_n are the bottom shear stresses, and Q_s and Q_n are the sediment flow rates, where the subscripts s and n indicate the longitudinal and transversal direction, respectively. Moreover, d_s^* and ρ_s are the (uniform) sediment diameter and density, ρ is the fluid density, g is the gravitational acceleration, and D_0^*, U_0^* and F_0 are the stream depth, the bulk velocity and the Froude number in uniform and unperturbed conditions, respectively.

Equations (2.2) and (2.3) describe the momentum balance of the liquid phase in the longitudinal and transversal direction. Equation (2.4) is the continuity equation for the liquid phase, where Π is a parameter in the $[p, 1]$ range taking into account the sediment porosity, p, the particle Reynolds number, and the Shields stress (Lanzoni *et al.*, 2007; Cao & Hu, 2008; Lanzoni *et al.*, 2008). In a similar way to some previous morphodynamic studies (Lanzoni *et al.*, 2008; Camporeale & Ridolfi, 2009), we have observed that the precise value of Π plays a marginal role in the bar dynamics; therefore, $\Pi = p = 0.4$ has been assumed in the following. Finally, equation (2.5) is the Exner continuity equation for the solid phase,

where Q_0 is the ratio between the scale of sediment discharge and the flow rate discharge, and reads

$$Q_0 = \frac{d_s^* \left[(\rho_s/\rho - 1) \, g d_s^* \right]^{1/2}}{(1-p) \, D_0^* U_0^*}. \tag{2.6}$$

It should be noted that, in all the previous works on bar dynamics, the time derivatives in the equations involving the liquid phase were disregarded. The bed evolution in fact exhibits timescales much longer than the water stream one. As a result, the stream can be assumed in equilibrium with the bed geometry, the flow field can be regarded as quasi steady and, consequently, the only temporal derivative in the Exner equation (2.5) can be retained. This approach is suitable for usual linear stability analysis, but it is insufficient for the nonmodal analysis, where the interactions among the time evolutions of all the perturbation components – i.e., perturbations of U, V, D, and H – play a crucial role in determining the transient behaviour of the dynamical system. For this reason, we have kept all the time derivatives in the system (2.2-2.5).

Model (2.2-2.5) is completed with the boundary conditions

$$V = Q_n = 0 \quad (n = \pm 1), \tag{2.7a,b}$$

which state impermeable and fixed lateral walls.

In order to close the mathematical problem, the bed shear stresses and sediment flow rates have to be related to the variables (U, V, H, D). The bottom shear stress can be expressed (see Parker, 1976; Blondeaux & Seminara, 1985) as $(\tau_s, \tau_n) = (U, V)C(U^2 + V^2)^{1/2}$, where C is a friction coefficient. As bars (which are large scale bed forms) can emerge from both a plane or from a dune covered bed, both scenarios are considered. If the unperturbed bed is flat, the Einstein (1950) formula is adopted

$$C = \left[6 + 2.5 \ln \left(\frac{D}{2.5 d_s} \right) \right]^{-2}, \tag{2.8}$$

where $d_s = d_s^*/D^*$ is the non-dimensional diameter of the sediment particles, while, if the bed is dune covered, Engelund & Hansen (1967) proposed

$$C = \left[6 + 2.5 \ln \left(\frac{\theta'}{\theta} \frac{D}{2.5 d_s} \right) \right]^{-2} \frac{\theta}{\theta'}, \tag{2.9}$$

with $\theta' = 0.06 + 0.4\theta^2$ (see Leopold *et al.*, 1964) and

$$\theta = \frac{\tau_0^*}{(\rho_s - \rho)\,gd_s^*}, \quad \tau_0^* = \rho g D_0^* S, \qquad \text{(2.10a,b)}$$

where θ is the Shields parameter, S is the channel slope, and τ_0^* is the bed shear stress.

The bed load rates are written as $(Q_s, Q_n) = (\cos\delta, \sin\delta)\Phi$, where Φ is the total sediment flow magnitude and δ is its angle of deviation from the longitudinal direction. In a horizontal bed, the direction of the sediment particles coincides with the shear (i.e., flow) direction, but if the plane is inclined, deviations due to gravity have to be considered. To this aim, Engelund (1981) proposed

$$\sin\delta = \frac{V}{\sqrt{U^2 + V^2}} - \frac{r}{\beta\sqrt{\theta}}\frac{\partial}{\partial n}\left(F_0^2 H - D\right) \qquad \text{(2.11)}$$

where r is an experimental constant. Olesen (1983) and Colombini *et al.* (1987) suggested the value $r = 0.3$, which was confirmed theoretically by Sekine & Parker (1992).

Meyer-Peter and Muller formula, in the form proposed by Chien (1956) $\Phi = 8(\theta - \theta_c)^{3/2}$, and the formula by Engelund & Hansen (1967), $\Phi = 0.05\theta^{5/2}/C$, are used for the sediment flow rate in the plane bed dune covered bed regimes. The threshold value of the Shields parameter for sediment motion inception, θ_c, is expressed by means of the Brownlie (1981) relation. Finally, the Chabert & Chauvin (1963) criteria is adopted to distinguish a plane bed low regime from dune covered bed regime , while the limit for a ripple bed regime is defined by the Engelund & Hansen (1967) diagram.

In short, bar evolution is modelled using four partial differential equations (2.2-2.5), boundary conditions are applied at the lateral walls, and the mathematical problem is closed by empirical relations which define shear stresses and sediment transport. The four dimensionless parameters that determine the system behaviour of the system are β, d_s, θ, and θ_c; the Froude number, F_0, can be used in place of d_s or θ.

2.2.2 Perturbation energy and asymptotic stability analysis

In order to study the behaviour of the system, when a small disturbance breaks the uniform flow condition, the variables are replaced

with perturbed ones

$$(U, V, D, H) = (1,0,1, H_0) + \epsilon\, (U_1, V_1, D_1, H_1)\,, \qquad (2.12)$$

$$(\tau_s, \tau_n, Q_s, Q_n) = (C_0,0, \Phi_0,0) + \epsilon\, (\tau_{s1}, \tau_{n1}, Q_{s1}, Q_{n1})\,, \qquad (2.13)$$

where $\epsilon \ll 1$, and subscripts "0" and "1" indicate the unperturbed state and perturbations, respectively. After linearization, the differential system (2.2-2.5) becomes

$$\frac{\partial U_1}{\partial t} + \frac{\partial U_1}{\partial s} + \frac{\partial H_1}{\partial s} + \beta\, (\tau_{s1} - D_1 C_0) = 0, \qquad (2.14a)$$

$$\frac{\partial V_1}{\partial t} + \frac{\partial V_1}{\partial s} + \frac{\partial H_1}{\partial n} + \beta \tau_{n1} = 0, \qquad (2.14b)$$

$$\frac{\partial}{\partial t} \left[p F_0^2 H_1 - (p-1)\, D_1 \right] + \frac{\partial U_1}{\partial s} + \frac{\partial V_1}{\partial n} + \frac{\partial D_1}{\partial s} = 0, \qquad (2.14c)$$

$$(1-p) \frac{\partial}{\partial t} \left(F_0^2 H_1 - D_1 \right) + Q_0 \left(\frac{\partial Q_{s1}}{\partial s} + \frac{\partial Q_{n1}}{\partial n} \right) = 0, \qquad (2.14d)$$

while the closure relations read

$$\tau_{s1} = C_0\, (s_1 U_1 + s_2 D_1)\,, \quad \tau_{n1} = C_0 V_1, \qquad (2.15a,b)$$

$$Q_{s1} = \Phi_0\, (f_1 U_1 + f2 D_1)\,, \qquad (2.15c)$$

$$Q_{n1} = \Phi_0 \left[V_1 - R \frac{\partial}{\partial n} \left(F_0^2 H_1 - D_1 \right) \right], \qquad (2.15d)$$

with

$$s_1 = \frac{2}{1 - C_T}, \quad s_2 = \frac{C_D}{1 - C_T}, \qquad (2.16a,b)$$

$$f_1 = \frac{2\Phi_t}{1 - C_T}, \quad f_2 = \Phi_D + \frac{C_D \Phi_t}{1 - C_T}, \qquad (2.16c\text{-}d)$$

$$R = \frac{r}{\beta\, \sqrt{\theta_0}}, \qquad (2.16e)$$

where θ_0 is the Shields parameter at the unperturbed state and

$$C_D = \frac{1}{C_0} \frac{\partial C}{\partial D}, \quad C_T = \frac{\theta_0}{C_0} \frac{\partial C}{\partial \theta}, \qquad (2.17a\text{-}b)$$

$$\Phi_D = \frac{1}{\Phi_0} \frac{\partial \Phi}{\partial D}, \quad \Phi_T = \frac{\theta_0}{\Phi_0} \frac{\partial \Phi}{\partial \theta}. \qquad (2.17c\text{-}d)$$

In order to reduce system (2.14a-2.14d) to a system of (temporal) ordinary differential equations, we introduce the mathematical structure of the solution along the s and n coordinates, which is usually assumed to describe the longitudinal and transversal shape of bars (Blondeaux & Seminara, 1985). The system now reads

$$(U_1, V_1, D_1, H_1) = S_m \left(u_1, \frac{C_m}{S_m} v_1, d_1, h_1 \right) e^{miks} + \text{c.c} \quad (m \text{ odd}),$$
(2.18a)

$$(U_1, V_1, D_1, H_1) = C_m \left(u_1, \frac{S_m}{C_m} v_1, d_1, h_1 \right) e^{miks} + \text{c.c} \quad (m \text{ even}),$$
(2.18b)

where $u_1 = u_1(t)$, $v_1 = v_1(t)$, $d_1 = d_1(t)$, and $h_1 = h_1(t)$ are the time dependent perturbation amplitudes, $S_m = \sin(\pi mn/2)$, $C_m = \cos(\pi mn/2)$, $\text{i} = \sqrt{-1}$, c.c is the complex conjugate, m is a positive integer number that defines the solution mode (for alternate bars $m = 1$), and k is the longitudinal wave number of the perturbation. It should be noted that this sinusoidal structure satisfies the boundary conditions (2.7).

In order to study how perturbations evolve in time, it is necessary to choose a physically relevant norm that is able to summarize the behaviour of the whole system. A natural and common choice is the total energy of the perturbation (Reddy & Henningson, 1993; Olsson & Henningson, 1995; Camporeale & Ridolfi, 2009). In the present problem, such (dimensionless) energy is made up of a kinetic component, K, and a potential component, P, the latter being formed by two contributions that derive from the water surface (P_s) and the bed fluctuations (P_b), i.e., $P = P_s + P_b$. In the wavenumber space, the three components are defined as $K = (|u_1|^2 + |v_1|^2)/2$, $P_s = |h_1|^2/(2F_0^2)$ (capillarity is neglected due to the turbulent flow), and $P_b = \xi |\eta_1|^2/(2F_0^2)$. In these relations, the null potential has been set on the undisturbed water surface, h_1 and η_1 are the fluctuations of the water surface and bed, respectively, with respect to the undisturbed state (i.e., $H = H_0 + h_1$ and $\eta = \eta_0 + \eta_1$), and $\xi = (1 - p)(\rho_s - \rho)/\rho$ represents the submerged sediment density.

The total energy density of the perturbation is therefore equal to

$$E = \frac{1}{2} \left(|u_1|^2 + |v_1|^2 + \frac{|h_1|^2}{F_0^2} + \frac{\xi |\eta_1|^2}{F_0^2} \right) = ||\boldsymbol{q}||^2, \qquad (2.19)$$

where $|| \cdot ||^2$ indicates the l^2 norm $(=(\sum_i q_i^2)^{1/2})$ and $\boldsymbol{q}$ is defined as (superscript "T" indicates the transpose)

$$\boldsymbol{q}^T = (q_1, q_2, q_3, q_4) = \frac{\sqrt{2}}{2}\left(u_1, v_1, \frac{h_1}{F_0}, \frac{\eta_1 \sqrt{\xi}}{F_0}\right). \qquad (2.20)$$

In order to obtain the algebraic operator which describes the time evolution of $\boldsymbol{q}$, system (2.14) is rewritten in terms of bed elevation η instead of water depth D, recalling that $d_1 = F_0^2 h_1 - \eta_1$, and after some algebra one obtains

$$\frac{\mathrm{d}\boldsymbol{q}}{\mathrm{d}t} = \mathbf{A}\boldsymbol{q}. \qquad (2.21)$$

where

$$\mathbf{A} = \frac{-\mathrm{i}k}{F_0^{-3}} \cdot$$

$$\begin{bmatrix} \frac{k - \mathrm{i}\chi_0 s_1}{kF_0^3} & 0 & \frac{1}{F_0^2} - \frac{\mathrm{i}\chi_0(s_2 - 1)}{k} & \frac{\mathrm{i}\chi_0(s_2 - 1)}{kF_0^2\sqrt{\xi}} \\ 0 & \frac{k - \mathrm{i}\chi_0}{kF_0^3} & \frac{-\mathrm{i}\pi}{2kF_0^2} & 0 \\ \frac{f_1 Q_0 \Phi_0 + 1}{F_0^6} & \frac{\mathrm{i}\pi(Q_0\Phi_0 + 1)}{2kF_0^6} & \frac{f_2 Q_0 \Phi_0 + 1}{F_0^3} & \frac{-4f_2 Q_0\Phi_0 k - k - \mathrm{i}\pi^2 Q_0\Phi_0 R}{4kF_0^5\sqrt{\xi}} \\ \frac{f_1 Q_0 \Phi_0 \sqrt{\xi}}{\bar{p}F_0^4} & \frac{\mathrm{i}\pi Q_0 \Phi_0 \sqrt{\xi}}{2\bar{p}kF_0^4} & \frac{f_2 Q_0 \Phi_0 \sqrt{\xi}}{\bar{p}F_0} & \frac{-Q_0\Phi_0(\mathrm{i}\pi^2 R + 4f_2 k)}{4\bar{p}kF_0^3} \end{bmatrix},$$

$$(2.22)$$

with $\chi_0 = \beta C_0$ and $\bar{p} = (1 - p)$.

The matrix $\mathbf{A}$ fully describes the time evolution of $\boldsymbol{q}$, and not only its asymptotic behaviour. In the next section, we will study the nonnormality of this algebraic operator in detail and show its effects on the dynamics of disturbances u_1, v_1, h_1 and η_1 contained in the components of $\boldsymbol{q}$.

First, however, it is interesting to focus on the usual asymptotic behaviour by setting the temporal structure $\boldsymbol{q} \sim \exp(\Omega t)$. Such behaviour is controlled by eigenvalues of the matrix $\mathbf{A}$ and, as all the time derivatives have been retained, four eigenvalues, corresponding to the four components of $\boldsymbol{q}$, are expected. It is interesting to compare our results with previous stability analyses where only one eigenvalue (corresponding to the bed perturbation mode) was focused on. We have investigated a wide range of parameter values and we have found that:
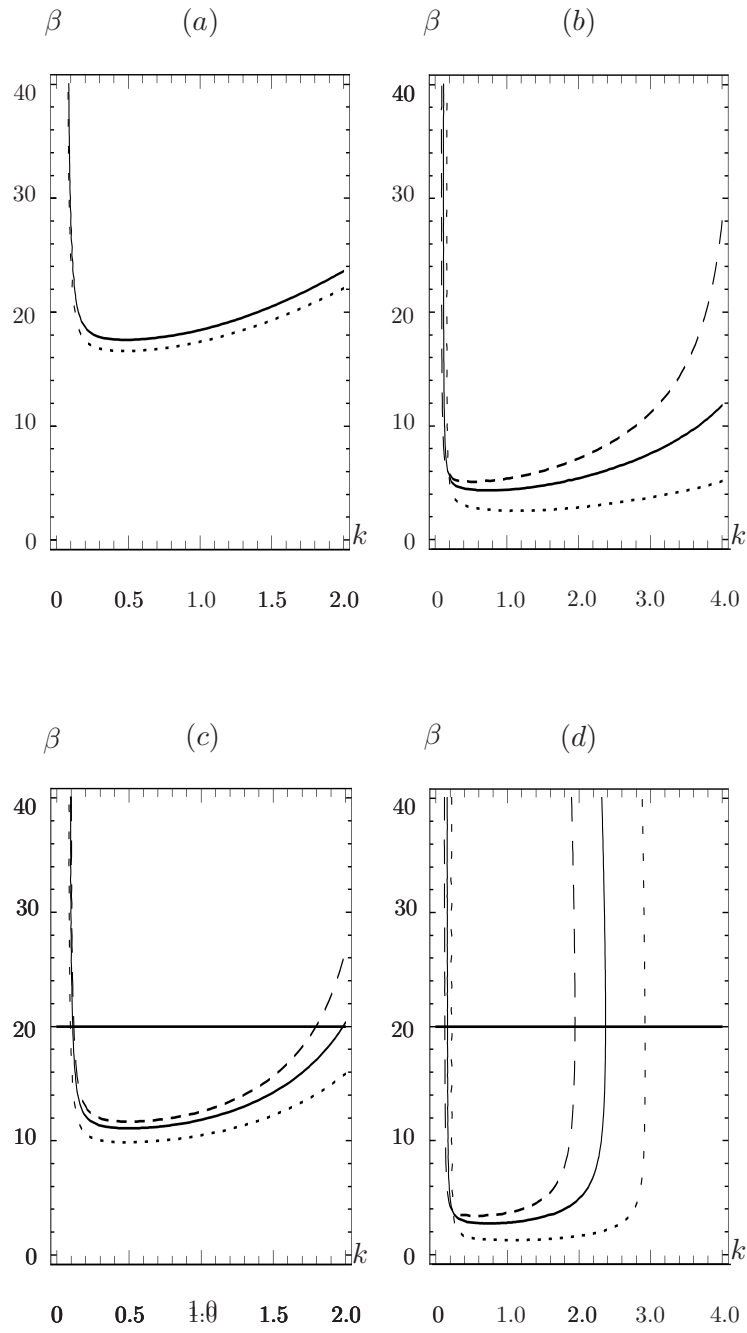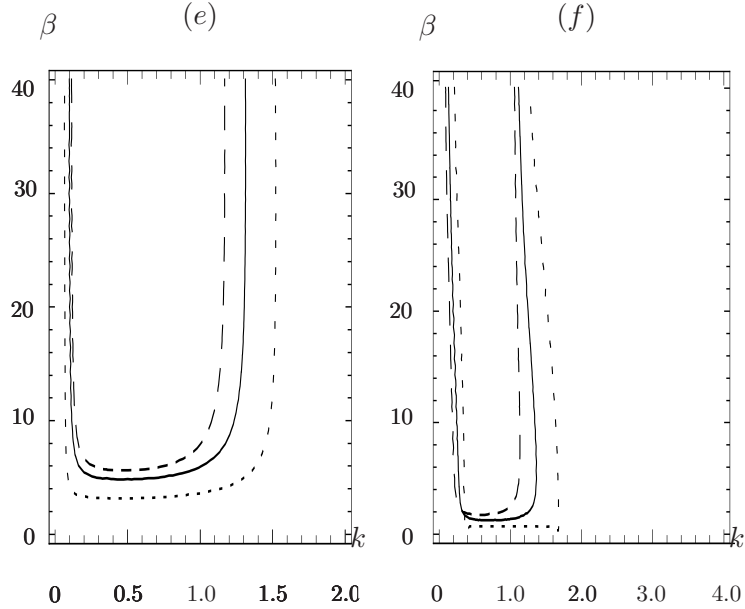
Figure 2.5.   Examples of marginal stability curves for the bar dynamics, where d_s is equal to 10^{-3}, 10^{-2}, and 10^{-1} in the first, second and third panel rows, respectively. Flat bed conditions are considered in the panels on the left, where: $\theta = 0.04$ (dotted line), $\theta = 0.05$ (continuous line), $\theta = 0.06$ (dashed line). The panels on the right refer to dune covered bed condition, where: $\theta = 0.2$ (dotted line), $\theta = 0.3$ (continuous line), $\theta = 0.4$ (dashed line). The solid straight lines in panels (b) and (e) mark the β-level chosen to trace the dispersion relations shown in figure 2.6.

1. the most unstable mode always results to be the morphodynamic one that is physically related to q_4, and the marginal stability curves (some of which are plotted in figure 2.5 for different parameter combinations) match perfectly with those obtainable under a quasi-steady assumption[1]. It follows that

---

[1]During the study of previous works on bar stability analysis, we noted a number of typos in the equations and inconsistencies with the marginal stability curves shown in the diagrams. Obviously they do not have an impact on the scientific value of these works, but we suggest the reader refers to the dispersion

the asymptotic stability of the morphological mode is not affected by the other three modes and the results of previous stability analysis (e.g., Blondeaux & Seminara, 1985; Colombini *et al.*, 1987; Tubino *et al.*, 1999) are confirmed;

2. if the dispersion relation is focused on, some differences between the two approaches emerge. An example is shown in figure 2.6, where it is possible to observe that the most (asymptotically) unstable wavenumber does not depend on the number of time derivatives retained, but that the corresponding growth rate does. In general, we have observed greater growth rates when all the derivatives are taken into account. Namely, the interplay between different temporal mode evolutions makes the (linear) growth of the unstable wave numbers faster;

3. previous works on bar stability usually only focused on the $m = 1$ case only, namely the alternate bar case. We have also investigated the system dynamics for greater values of m, and observed that the marginal stability curves corresponding to $m > 1$ are always inside the instability region for $m = 1$ (see figure 2.7). Therefore, alternate bars are more unstable than other more complex transversal patterns (Schielen *et al.*, 1993). Conversely, such patterns develop on a basic bed modelled by alternate bars;

4. finally, it is worth noticing that the four time-derivative differential system (2.21) allows one to study the occurrence of other (possibly coexistent) unstable modes linked to the flow field and free surface, while this is impossible under the quasi-steady hypothesis, where only one eigenvalue is investigated. It would be interesting to study how free surface instability – usually described on a rigid flat bed (e.g., Balmforth & Mandre, 2004) – is influenced by a deformable bed.

---

relation (3.7) reported in Federici & Seminara (2003) which does not contain errors.

(a)

(b)
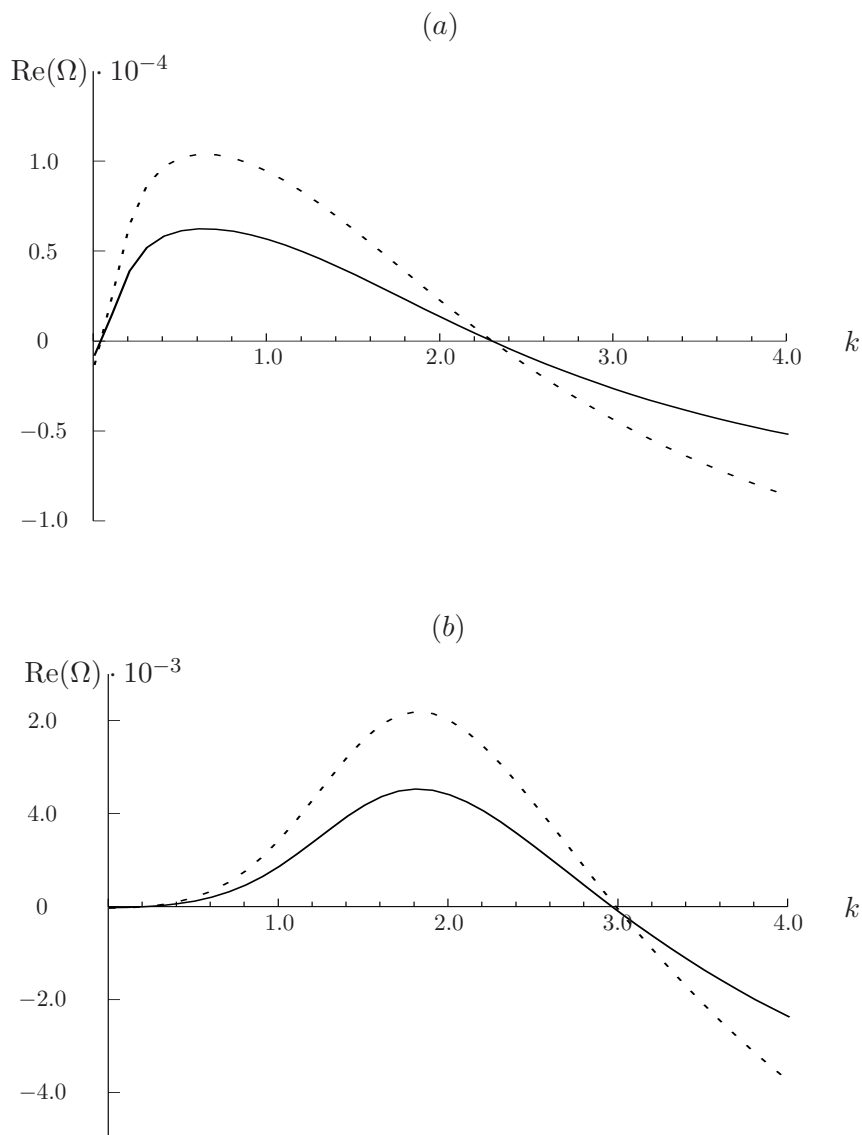
Figure 2.6.   Examples of the dispersion relation in flat (a) and dune covered (b) bed conditions. The curves corresponding to the four time-derivative model (dotted line) and to the quasi-steady model (solid line) are shown. In both panels $d_s = 0.01$, and $\beta = 20$, while $\theta = 0.06$ and $\theta = 0.20$ in panels (a) and (b), respectively.
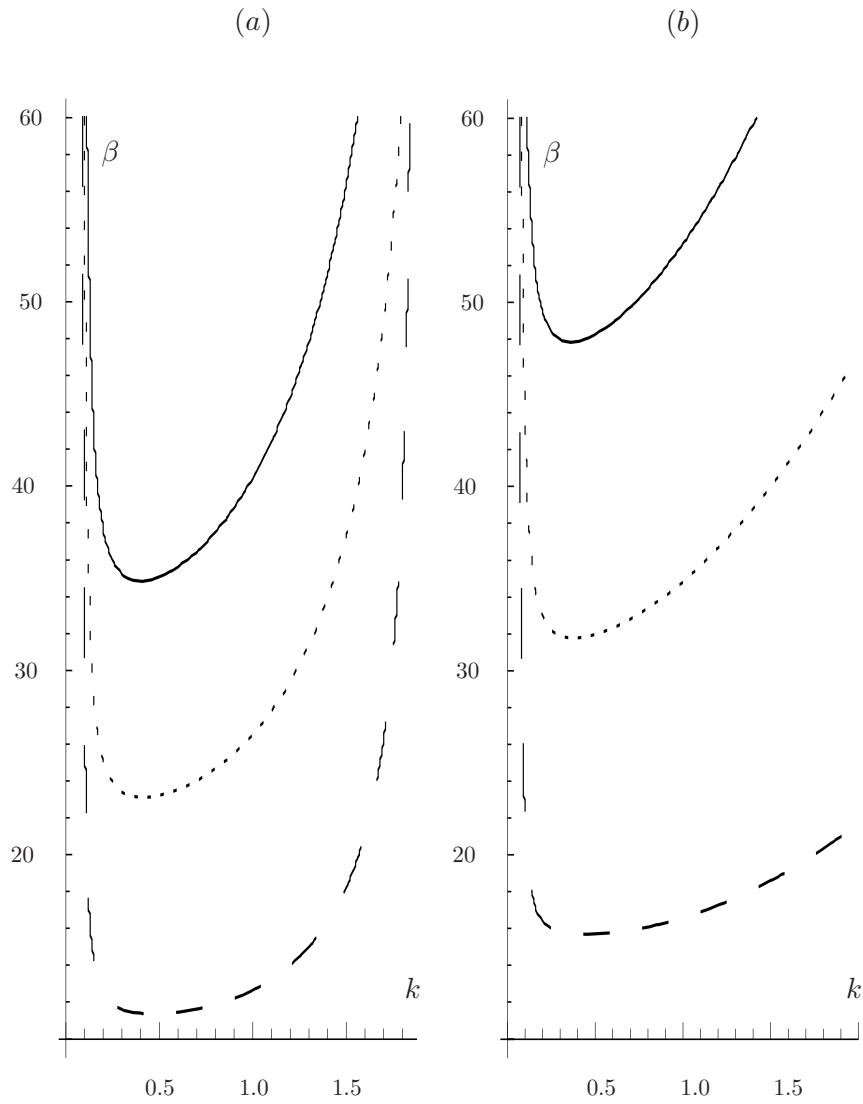
Figure 2.7.   Examples of neutral stability curves for flat (a) and dune covered (b) bed conditions. The curves correspond to $m = 1$ (dashed lines), $m = 2$ (dotted lines), and $m = 3$ (solid lines). $d_s = 0.001$, $\theta = 0.05$ in panel (a) and $d_s = 0.01$, $\theta = 0.05$ in panel (b).

2.3   Transient behavior analysis

In this section, we explore the dynamics of perturbation before it attains its asymptotic fate. As we are interested in transient growths, the region of the parameter space where the dynamical system is asymptotically stable will be focused on. The object of our analysis is the growth function $\hat{G}(t)$, defined as the upper envelope of the evolution, $G(t)$, of the normalized energy density for all possible initial conditions; namely (Trefethen & Embree, 2001)

$$\hat{G}(t) = \max_{\boldsymbol{q_0}} G(t) = \max_{\boldsymbol{q_0}} \frac{\|\boldsymbol{q}(t)\|^2}{\|\boldsymbol{q_0}\|^2} = \left\|e^{\mathbf{A}t}\right\|^2 \qquad \forall \boldsymbol{q_0}, \qquad (2.23)$$

where $\boldsymbol{q}_0$ is the initial disturbance. In the following, we will indicate, with $\hat{G}_{\max}$ and $t_{\max}$, the supremum value of the $\hat{G}(t)$ and the corresponding time when $\hat{G}(t_{\max}) = \hat{G}_{\max}$, respectively. As transient behaviour is driven by the nonnormality of the operator, our investigation begins by evaluating some quantities that are able to detect the nonnormality of $\mathbf{A}$.

2.3.1   Measures of nonnormality: condition number and pseudospectra

The starting point of the measuring of the nonnormality is the evaluation of condition number, $\kappa(\mathbf{V})$, of matrix $\mathbf{V}$ of the eigenvectors of $\mathbf{A}$. The condition number is defined as the product between the norm of a matrix and the norm of its inverse (i.e., $\kappa(\mathbf{V}) = ||\mathbf{V}|| ||\mathbf{V}^{-1}||$). Mathematically, it indicates how close a matrix is to a singular matrix. In the case of eigenvector matrix $\mathbf{V}$, the condition number indicates how far from normal are the eigenvectors: $\kappa(\mathbf{V}) = 1$ corresponds to orthogonality, while the higher is the difference between $\kappa(\mathbf{V})$ and 1, the higher is the expected degree of nonnormality.

The condition number can be conveniently evaluated in terms of singular values. If matrix $\mathbf{V}$ is written as $\mathbf{V}\mathbf{U_r} = \mathbf{U_l}\boldsymbol{\Sigma}$ by singular value decomposition – where $\mathbf{U_r}$ and $\mathbf{U_l}$ are right and left unitary matrices (i.e., $||\mathbf{U_r}|| = ||\mathbf{U_l}|| = 1$) and $\boldsymbol{\Sigma}$ is the diagonal matrix that collects the singular values – it is possible to show (Golub & Van Loan, 2001) that $||\mathbf{V}|| = s_{\max}(\mathbf{V})$ where $s_{\max}(\mathbf{V})$ is the largest

singular value. It follows that

$$\kappa(\mathbf{V}) = \frac{s_{\max}(\mathbf{V})}{s_{\max}(\mathbf{V}^{-1})} = \frac{s_{\max}(\mathbf{V})}{s_{\min}(\mathbf{V})}. \qquad (2.24)$$

The condition number is plotted in figure 2.8 as a function of the problem parameters for some exemplifying cases. High values (of the order of 10^2) occur, especially for small values of θ and d_s. Strong nonnormal behavior of the bar dynamics is therefore expected in fine sediment beds characterized by low Shields stress.

The study of operator nonnormality by means of the condition number has the advantage of being simple, but does not describe the transient behaviour in detail. The condition number in fact only gives an upper estimation of the maximum transient growth over time, as $\hat{G}_{\max} \leq \kappa^2 e^{2t\Lambda_\uparrow(\mathbf{A})}$, where $\Lambda_\uparrow(\mathbf{A})$ is the largest eigenvalue of $\mathbf{A}$ (Spijker, 1991). A more comprehensive description of nonnormality can be obtained using pseudospectra, which are an extension of the usual eigenvalue spectra.

The ordinary differential system (2.21) that describes the temporal evolution of the perturbations has the solution

$$\boldsymbol{q}(t) = \boldsymbol{q_0}e^{\mathbf{A}t} = \boldsymbol{q_0}\mathbf{V}\left[e^{\Lambda(\mathbf{A})t}\right]\mathbf{V}^{-1}, \qquad (2.25)$$

where $\Lambda(\mathbf{A})$ is the spectrum of $\mathbf{A}$, namely the collection of the eigenvalues of the dynamical system. The spectrum is formally defined as the set of complex numbers z where the norm of the resolvent set, $(z\mathbf{I} - \mathbf{A})^{-1}$, is equal to infinity; namely

$$\Lambda(\mathbf{A}) = \left\{ z \in \mathbb{C} : \left\| (z\mathbf{I} - \mathbf{A})^{-1} \right\| = \infty \right\}. \qquad (2.26)$$

Similarly, the pseudospectrum is defined as

$$\Lambda_\epsilon(\mathbf{A}) = \left\{ z \in \mathbb{C} : \left\| (z\mathbf{I} - \mathbf{A})^{-1} \right\| \leqslant \epsilon^{-1} \right\}, \qquad (2.27)$$

with $\epsilon \ll 1$. If operator $\mathbf{A}$ is normal, the resolvent set is large only very close to the eigenvalues and the pseudospectrum is the union of circles of radius ϵ centred on the eigenvalues. Instead, when the matrix is non-normal the norm of the resolvent is also very large far from the eigenvalues, and the pseudospectra forms a much larger set than in the case of a normal operator.
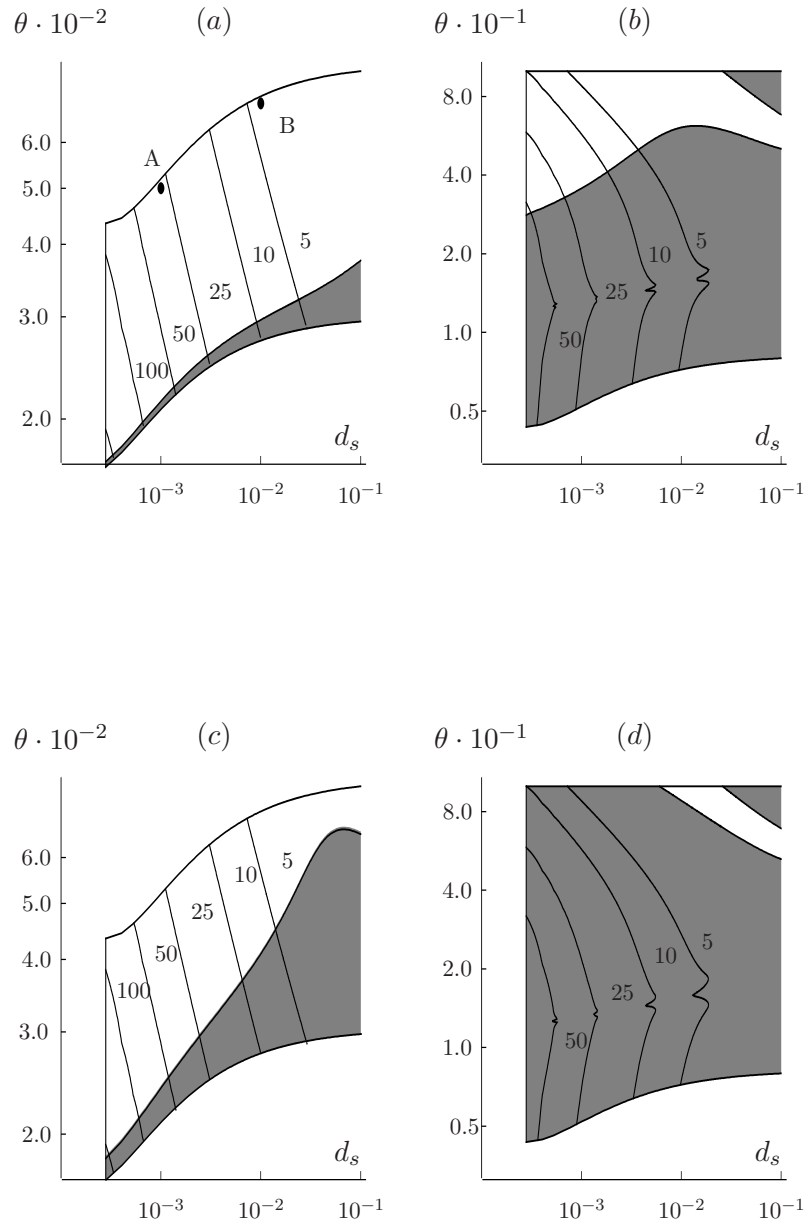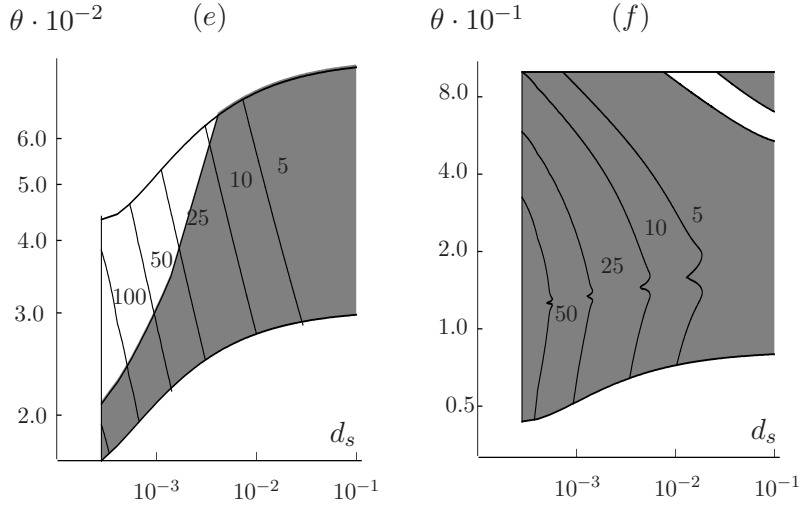
Figure 2.8. Condition number (the value is reported as iso-κ lines) as a function of the parameters d_s and θ for wave number $k = 1$, which is representative of bars. The panels on the left and right refer to a plane bed and a dune covered bed, respectively. The aspect ratio is $\beta = 5$ (first row), 10 (second row), and 15 (third row). The shaded zones correspond to asymptotically unstable regions.

Relation (2.27) gives the spectrum when $\epsilon = 0$, while for $\epsilon \to \infty$ it provides the numerical range, $W(\mathbf{A})$, of the matrix operator. The numerical range contains all the Rayleigh quotients of $\mathbf{A}$, namely

$$W(\mathbf{A}) = \left\{ z \in \mathbb{C}^N : z = \boldsymbol{x}^* \mathbf{A} \boldsymbol{x}, \|\boldsymbol{x}\| = 1 \right\}, \qquad (2.28)$$

and plays an important role in investigating the evolution of perturbation. The initial growth rate of $\boldsymbol{q}(t)$ is determined from the supremum of the real part of the numerical range, the so-called numerical abscissa $\omega(\mathbf{A})$. The Hille-Yoshida and Lummer-Philips theorems (Trefethen & Embree, 2001) state that

$$\frac{\mathrm{d}}{\mathrm{d}t} \sqrt{\left\| \hat{G} \right\|} \bigg|_{t=0} = \omega(\mathbf{A}) = \Lambda_\uparrow \left[\mathbf{H}(\mathbf{A}) \right] = \Lambda_\uparrow \left[\frac{1}{2}(\mathbf{A} + \mathbf{A}^*) \right], \quad (2.29)$$

where $\mathbf{H}\left(\mathbf{A}\right)$ is the Hermitian part of operator $\mathbf{A}$ and $\mathbf{A}^{*}$ is the transpose conjugate. The same formula (2.29) can be conveniently used to compute the numerical range: just rotating the original matrix according to $\mathbf{A} \rightarrow \mathrm{e}^{i\phi}$, with $\phi \in [0, \pi]$, and to calculate the Rayleigh quotient of the original matrix using the principal eigenvector of its Hermitian part (Schmid & Henningson, 2001). The evaluation of the numerical range is important, because its intrusion into the right half of the complex plane (i.e., $\omega\left(\mathbf{A}\right) > 0$) is a proxy of nonnormality and entails the occurrence of transient growths. On the contrary, the numerical range of a normal operator is always confined to the left half of the complex plane and the perturbations decay monotonically.

Two examples of pseudospectrum portraits are shown in figure 2.9. The panels on the left and right refer to the conditions indicated in the diagram of figure 2.8*a* with points A and B, respectively. The corresponding eigenvalues are reported in table 2.1; all of them have a negative real part and therefore correspond to asymptotically stable cases. Case A is characterized by a high condition number ($\kappa = 28.6$, see figure 2.8) and the high degree of nonnormality of operator can be confirmed through an analysis of the pseudospectrum portrait: it appears as a set of complex numbers much larger than the union of ϵ-radius disks centred in the eigenvalues. The parameters used in the panels on the right of figure 2.9 instead lead to a low condition number ($\kappa = 4.1$), which predicts a low degree of nonnormality. Again in this case, quasi-normal behaviour can be confirmed by observing the pseudospectrum portrait, which essentially coincides with the union of the circles centred on the eigenvalues.

Table 2.1.   Eigenvalues for cases A and B reported in figure 2.8*a*.

	Case A	Case B
σ_1	$-6.6 \cdot 10^{-3} - 10.8\mathrm{i}$	$-9.9 \cdot 10^{-3} - 4.6\mathrm{i}$
σ_2	$-8.0 \cdot 10^{-3} + 8.7\mathrm{i}$	$-1.8 \cdot 10^{-2} + 2.6\mathrm{i}$
σ_3	$-1.9 \cdot 10^{-2} - 1.0\mathrm{i}$	$-3.7 \cdot 10^{-2} - 1.0\mathrm{i}$
σ_4	$-1.5 \cdot 10^{-5} - 6.9 \cdot 10^{-5}\mathrm{i}$	$-2.5 \cdot 10^{-4} - 1.5 \cdot 10^{-3}\mathrm{i}$

The corresponding numerical range is shown in figures $2.9c - d$.

In panel 2.9*c*, it is possible to observe that the numerical range protrudes deeply into the right half of the complex plane, thus a strong transient growth of the perturbation can be predicted. On the contrary, the numerical range in figure 2.9*d* displays a moderate value of the numerical abscissa, indicating a weak transient growth.

2.3.2   Transient behavior

Some strong clues about the existence of large transient growths in the dynamics of the perturbation energy were found in the previous subsection: the condition number is high over a wide range of parameters, the pseudospectra show a typical portrait of a non-normal operator, and, finally, the numerical range exhibits deep intrusions into the real positive part of the complex plane. A more detailed analysis of the growth function, $\hat{G}(t)$ is now required, with the aim of evaluating the entity of the transient energy amplification.

An optimization procedure, based on the singular value decomposition, can be conveniently used to evaluate the growth function (2.23). Observing that $\mathbf{A} = \mathbf{V}\Lambda(\mathbf{A})\mathbf{V}^{-1}$, it is possible to write (Trefethen & Embree, 2001)

$$\hat{G}(t) = \left\| e^{\mathbf{A}t} \right\|^2 = \left\{ s_{\max} \left[\mathbf{V} e^{t\Lambda(\mathbf{A})} \mathbf{V}^{-1} \right] \right\}^2. \qquad (2.30)$$

The growth function behaviour, for cases A and B already mentioned in figure 2.9, are plotted in figure 2.10 using relation (2.30). The operator with highest condition number and numerical abscissa exhibits the strongest transient growth which, we emphasize, is due to a purely linear mechanism. The effective maximum grow rate, $\hat{G}_{\max}$, can be compared with the upper bounds obtainable from the condition number ($\hat{G}_{\max} \leq \kappa^2 e^{2t\Lambda_{\uparrow}(\mathbf{A})}$) and the numerical abscissa ($\hat{G}_{\max} \leq e^{2t\omega(\mathbf{A})}$) (Trefethen & Embree, 2001), which result to be quite realistic. In fact, they give $(784, 5.8 \cdot 10^5)$ for case A and $(16, 181)$ for case B, while the values deducible from the plot of $\hat{G}(t)$ are $\hat{G}_{\max} = 764$ and $\hat{G}_{\max} = 15.6$ in the first and second case, respectively. A further estimate is given by means of the Kreiss constant, $K(\mathbf{A})$, which allows a lower bound to be assessed. In this case, the bounds are $K(\mathbf{A}) \leq \sqrt{\hat{G}_{\max}} \leq eNK(\mathbf{A})$ (Trefethen & Embree, 2001), where N is the matrix dimension (here $N = 4$)
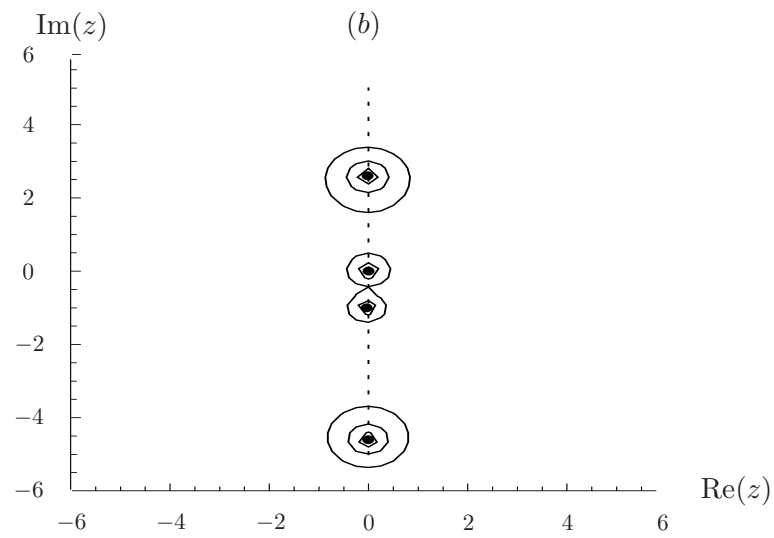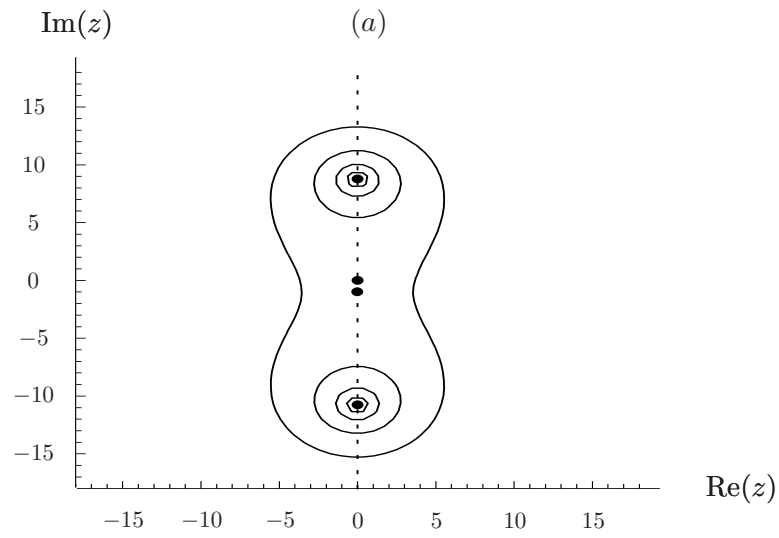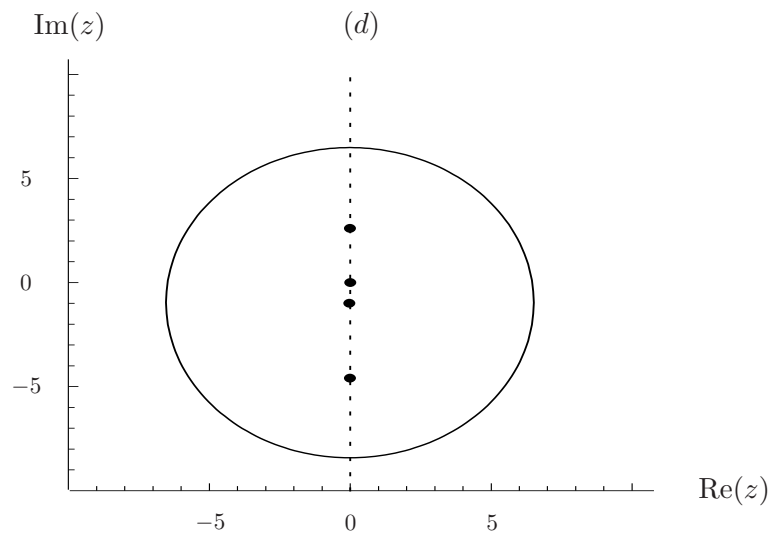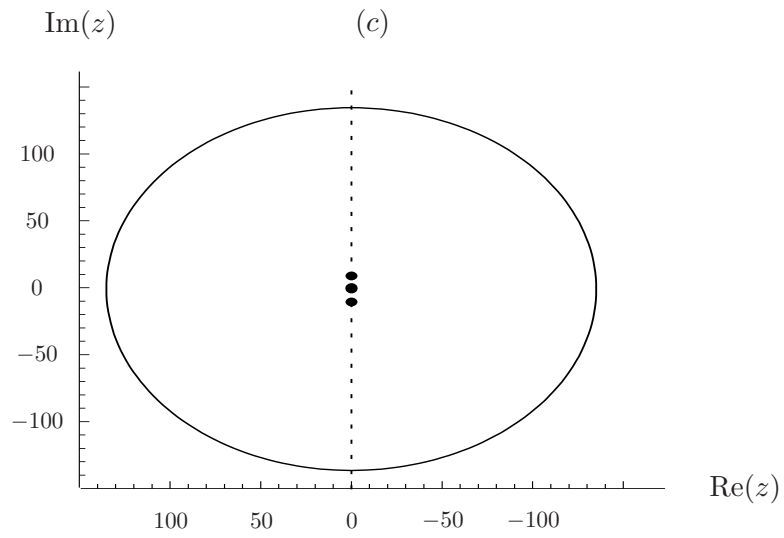
Figure 2.9.   Pseudospectra plots (panels (a) and (b)) and numerical range (panels (c) and (d)) corresponding to points A and B displayed in figure 2.8. In the panels on the left $k = 1$, $\beta = 5$, $ds = 10^{-3}$, $\theta = 0.05$, $\theta_c = 0.02$ (case A). In the panels on the right $k = 1$, $\beta = 5$, $ds = 10^{-2}$, $\theta = 0.07$, $\theta_c = 0.03$ (case B). The pseudospectrum contours are computed (from outer to inner) for $\epsilon = 0.4$, 0.2, 0.1, 0.05. The eigenvalues are shown by the dots in the centre of the circles. The numerical range is plotted with a continuous line in the lower panels, where the eigenvalues (dots) are also displayed. The numerical abscissa is $\omega = 135.1$ in panel (c) and $\omega = 6.5$ in panel (d).

and the Kreiss constant reads $K(\mathbf{A}) = \sup\left[\mathrm{Re}(z) \cdot \left\|(z\mathbf{I} - \mathbf{A})^{-1}\right\|\right]$, where $z \in \mathbb{C}$ and $\mathbf{I}$ is the unitary matrix. For case A the inequality reads $13.9 \leq 27.8 \leq 554.4$, while for case B $2.1 \leq 3.9 \leq 8.4$.

A typical periodic oscillation is superimposed onto the transient growth plot. Its period, T_{osc}, can be estimated from the absolute value of the smallest imaginary part of the eigenvalues,

$$T_{\mathrm{osc}} = \frac{\pi}{\left|\min\{\mathrm{Im}\left[\Lambda\left(\mathbf{A}\right)\right]\}\right|}. \tag{2.31}$$

In case A and case B shown in figure 2.10, the previous relation gives $T_{\mathrm{osc}} = 0.29$ and $T_{\mathrm{osc}} = 0.70$, respectively, while the values obtained from the $\hat{G}(t)$ plots are equal to $T = 0.31$ and $T = 0.87$. The agreement between the values predicted by means of the eigenvalues and the real ones is good, and confirms other similar findings, observed in falling liquids, by Coppola & de Luca (2006), in two fluids channel flow, by Yecko (2008), in the de Saint-Venant-Exner equations, by Camporeale & Ridolfi (2009), and in non Newtonian fluid layers (Camporeale *et al.*, 2009).

2.3.3 Analysis of energy components

In the previous subsections, we focused on the total energy, E, of the perturbation. More information about the physical behaviour of the system can be gained by studying the time evolution of the single components of the energy, namely K, P_s, and P_b. This allows one (i) to elucidate the interactions among the perturbation components and (ii) to find the dominant energy components. Vector $\boldsymbol{q}(t)$ contains all the information we are searching for, in fact $K = |q_1|^2 + |q_2|^2$, $P_s = |q_3|^2$, and $P_b = |q_4|^2$. Therefore, once the initial condition $\boldsymbol{q_0}$ is chosen and $\boldsymbol{q}(t)$ is computed by (2.25), the evolution of its components gives the dynamics of the energy components.

As growth function $\hat{G}(t)$ represents the upper envelope of the evolutions of all the possible initial disturbances with the unit energy norm, it follows that different initial conditions maximize the amplification factor at different times. The specific initial condition, $\boldsymbol{q_0}^{(t_*)}$, which maximizes the energy at a generic time $t = t_*$ can be obtained through two steps: firstly, the exponential matrix can be written by means of eigenvalue decomposition

$\hat{G}(t)$ (a)

10^2

10^1

t

0 1 2 3 4 5

$\hat{G}(t)$ (b)

10^2

10^1

10^0

t

0 100 200 300 400 500 600
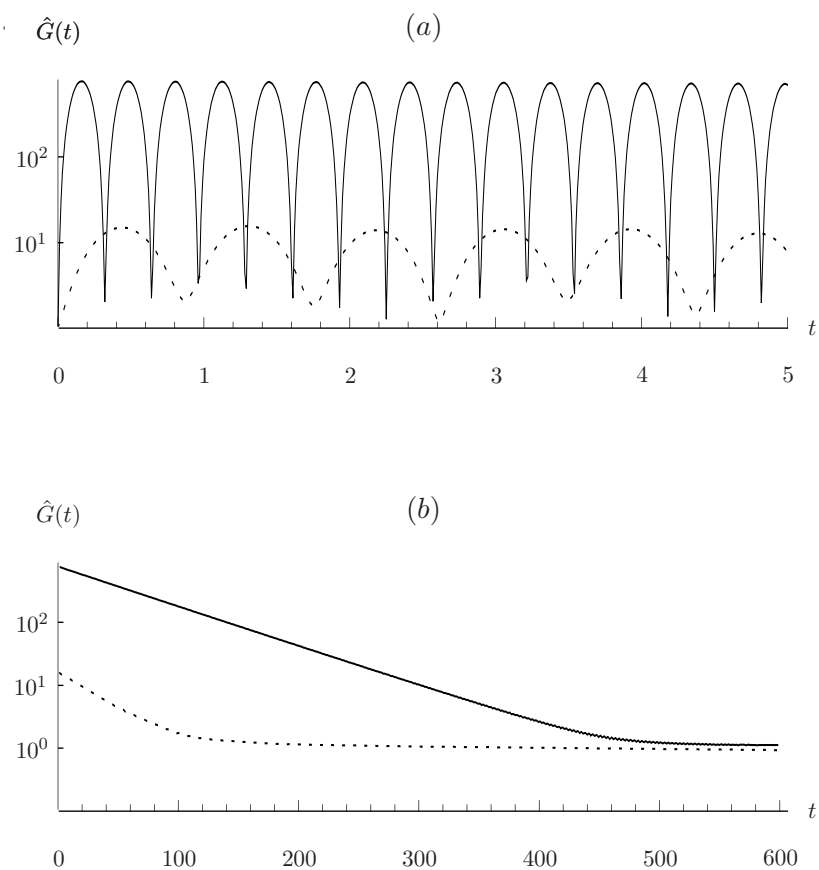
Figure 2.10. Plots of growth functions for case A (solid lines) and case B (dotted lines) considered in figure 2.9 (see the caption for the data). The growth functions during the first stages of perturbation dynamics are reported in the upper panel, while only the envelope of the peaks is shown in the lower panel. This is done to clarify the $\hat{G}$ behaviour for longer times.

(a)

(b)

(c)

(d)
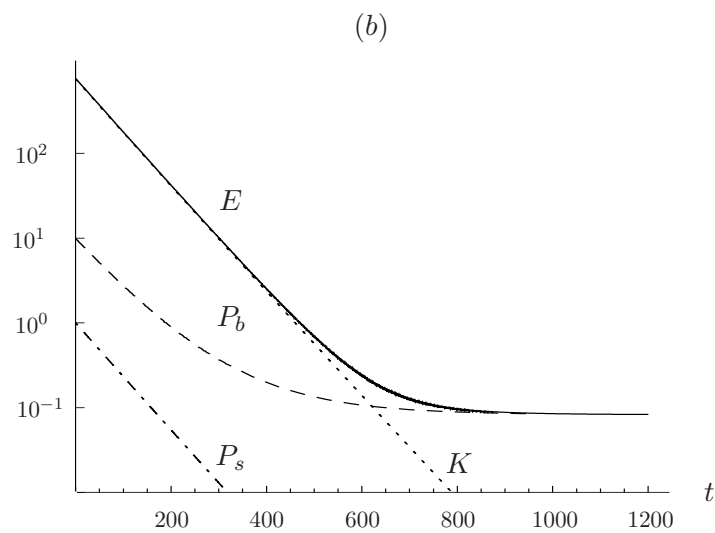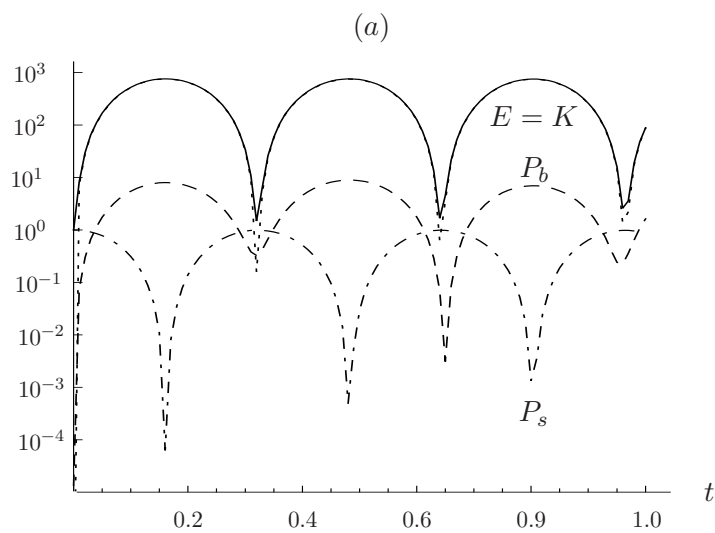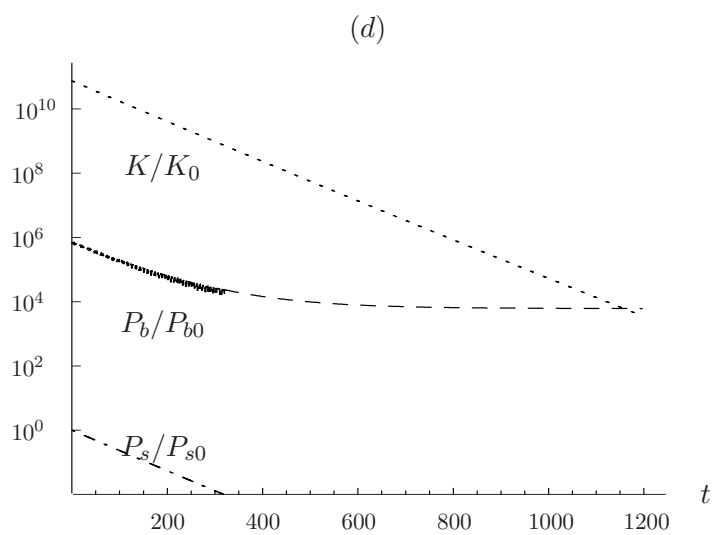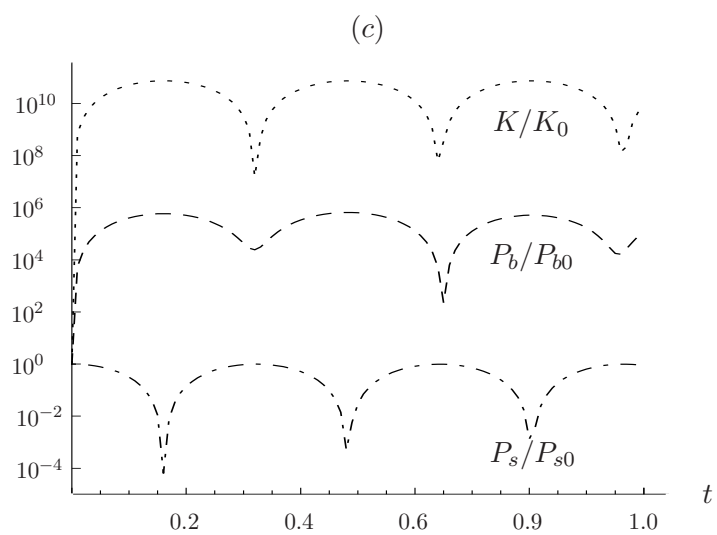
Figure 2.11. Plots of the time evolution of the perturbation energy components for case A with $k = 1$. The optimal initial condition is chosen. In panels $(a - b)$, the energy components are scaled so that their sum is equal to G (thus $G(t = 0) = 1$). In panels $(c - d)$, the energy components are scaled with their initial value. The behaviour of the total energy E (continuous lines), the kinetic energy K (dotted lines), the potential energy of the free surface P_s (dot-dashed lines), and the potential energy of the bed surface P_b (dashed lines) are shown. For the sake of clarity, only the peak envelope of the curves are reported in the panels on the right and the oscillations are disregarded. in logarithmic scale and, in panel (a), $E(t)$ and $K(t)$ result to be practically coincident.

$e^{t_* \mathbf{A}} = \mathbf{V} e^{\Lambda(\mathbf{A}) t_*} \mathbf{V}^{-1}$, where $\mathbf{V}$ is the eigenvector matrix. Secondly, it can be shown that the initial condition $\boldsymbol{q_0}^{(t_*)}$ is the column of the right unitary matrix $\mathbf{U_r}$ of the singular value decomposition of the right hand side of $\mathbf{V} e^{\Lambda(\mathbf{A}) t_*} \mathbf{V}^{-1}$ associated with the maximum singular value (Schmid & Henningson, 2001).

It is interesting to evaluate the initial condition that gives the maximum of the energy amplification over time, namely $t_* = t_{\max}$. For instance, in case A shown in figure 2.10, $\hat{G}_{\max}$ occurs at $t_{\max} = 0.16$ and the corresponding initial condition (called optimal initial condition) results to be

$$\hat{\boldsymbol{q}}_0 \equiv \boldsymbol{q_0}^{(t_{\max})} =$$
$$\left(2.5 \cdot 10^{-5}, (-6.1 - \mathrm{i}7.6) \cdot 10^{-5}, -0.72 - \mathrm{i}0.69, (2.4 + \mathrm{i}2.8) \cdot 10^{-3} \right).$$
$$(2.32)$$

Using (2.20), this initial condition can be written in terms of optimal disturbances of fluid velocity, stream surface, and bed elevation as

$$\left(|\hat{u_0}|, |\hat{v_0}|, \left|\hat{h_0}\right|, |\hat{\eta_0}| \right) =$$
$$\left(3.5 \cdot 10^{-5}, 1.4 \cdot 10^{-4}, 2.7 \cdot 10^{-1}, 9.9 \cdot 10^{-4} \right),$$
$$(2.33a)$$

$$\left(\arg\left(\hat{u_0}\right), \arg\left(\hat{v_0}\right), \arg\left(\hat{h_0}\right), \arg\left(\hat{\eta_0}\right) \right) =$$
$$(0, -2.24, -2.37, -0.87).$$
$$(2.33b)$$

The initial water depth perturbation that gives $\hat{G}_{\max}$ therefore results to be much larger (by about three orders of magnitude) than the initial perturbation of the flow field and bed elevation. The corresponding time evolutions of the energy components are shown in figure 11. Two representation are reported, in order to highlight different aspects. The energy components are reported in figures $2.11a - b$ so that, at any time, $K + P_s + P_b = G$. In this way, the contribution of the single energy components to the transient growth is clear: in the case shown in figures $2.11a - b$ most of the perturbation energy is kinetic energy. Therefore, the initial perturbation (2.32) only triggers a purely hydrodynamic instability, while the energy associated with the morphodynamic instability is lower by several orders of magnitude.

The component evolution normalized to its initial values, i.e. $K(t)/K_0$, $P_s(t)/P_{s0}$, and $P_b(t)/P_{b0}$ is instead reported in figures $2.11c - d$. This representation clearly shows which components of the perturbation undergo a higher amplification. In the case shown in figure $2.11b$, it can be observed that the growth of the kinetic energy is extremely large ($> 10^{10}$) compared to the growth rate of the bed potential-energy ($< 10^6$). This means that, even though some energy is transferred to the morphodynamic instability, the hydrodynamic instability is strongly prevalent.

Although figure 2.11 suggests that the morphodynamic mode experiences negligible transient growths, it is wrong to draw the conclusion that the nonnormality of operator $\mathbf{A}$ has no significant impact on the bed dynamics. The key point is in fact to focus on the appropriate initial conditions that maximize the energy related to the morphodynamic instability (P_b). To this aim, we introduce a different definition of the energy density in which the components corresponding to the kinematic and water potential energy are penalized by a coefficient $c \ll 1$. This new morphodynamics oriented energy reads

$$E_M = \frac{1}{2} \left[c \left(u_1^2 + v_1^2 + \frac{h_1^2}{F_0^2} \right) + \frac{\xi \eta_1^2}{F_0^2} \right], \qquad (2.34)$$

where the subscript M stands for morphodynamics. This approach was successfully used by Camporeale & Ridolfi (2009) in the analysis of one dimensional morphodynamic instabilities. In this way, all the components of the system are formally considered, but only the bed energy is actually taken into account. Following the same steps described in subsection 2.2.2, a vector

$$\boldsymbol{q}_M^T = \frac{c\sqrt{2}}{2} \left\{ u_1, v_1, \frac{h_1}{F_0}, \frac{\eta_1 \sqrt{\xi}}{cF_0} \right\} \qquad (2.35)$$

is introduced, so that its l^2 norm is equal to E_M. This vector only differs from $\boldsymbol{q}$ because it has $\sqrt{\xi}/c$ instead of $\sqrt{\xi}$ in the fourth component; thus, the sediment density results to be magnified and bed potential-energy is overestimated. The differential operator describing the time evolution of components, $\mathbf{A}_M$, can easily be derived from $\mathbf{A}$ (2.22) by putting ξ/c^2 in place of ξ. It should be

67

noted that the eigenvalues are not affected by this change; therefore, the penalization coefficient c has an impact on the transient growth, but the asymptotic fate remains unaltered.

The same measures of nonnormality used for $\mathbf{A}$ can be adopted for $\mathbf{A}_M$ and the picture remains almost the same, that is $\mathbf{A}_M$ also exhibits a high degree of nonnormality in a relevant portion of the parameter space. This is confirmed by the behavior of $\hat{G}_M(t)$ (figure 2.12 shows an example corresponding to the previously considered case A). It is possible to observe that strong transient growths occur; they are characterized by longer time scales than those observable for A and oscillations that have a larger period, T_{osc}. Both of the last features are due to the fact that the strong amplifications are now mainly ascribable to transient growths of the bed elevation, whose dynamics is characterized by a greater timescales than those of the hydrodynamic modes. For the example shown in the figure 2.12, the maximum $\hat{G}_{M,\text{max}}$ occurs at $t_* = t_{\text{max}} = 3.05$ and the corresponding optimal initial condition is

$$
\boldsymbol{q_0}_M^{(t_{\text{max}})} = \hat{\mathbf{q}}_{0,M} =
$$
$$
\left(-0.98, -0.004 - \mathrm{i}0.64, -1.97 - \mathrm{i}0.59, -10^{-3} - \mathrm{i}10^{-5} \right) \cdot 10^3,
$$
$$(2.36)$$

from which, using the definition of $\boldsymbol{q_0}_M$, one obtains

$$
\left(|\hat{u}_{0M}|, |\hat{v}_{0M}|, \left|\hat{h}_{0M}\right|, |\hat{\eta}_{0M}| \right) =
$$
$$
\left(1.41 \cdot 10^3, 8.9 \cdot 10^2, 5.5 \cdot 10^2, 2.71 \cdot 10^{-7} \right),
$$
$$(2.37a)$$

$$
\left(\arg\left(\hat{u}_{0M}\right), \arg\left(\hat{v}_{0M}\right), \arg\left(\hat{h}_{0M}\right), \arg\left(\hat{\eta}_{0M}\right) \right) =
$$
$$
(3.14, -1.56, -2.85, -3.07),
$$
$$(2.37b)$$

where the initial perturbation components have been rescaled so that $||\boldsymbol{q_0}_M|| = 1$.

It is now possible to evaluate the evolution of the single energy components by adopting the vector $\hat{\boldsymbol{q}}_{0\,M}$ as the initial condition in the differential system (2.21). It should be noticed that the modified operator $\mathbf{A}_M$ is only used to select the initial conditions that are prone to developing strong morphological transient growths, but the dynamics of the energy components is evaluated according
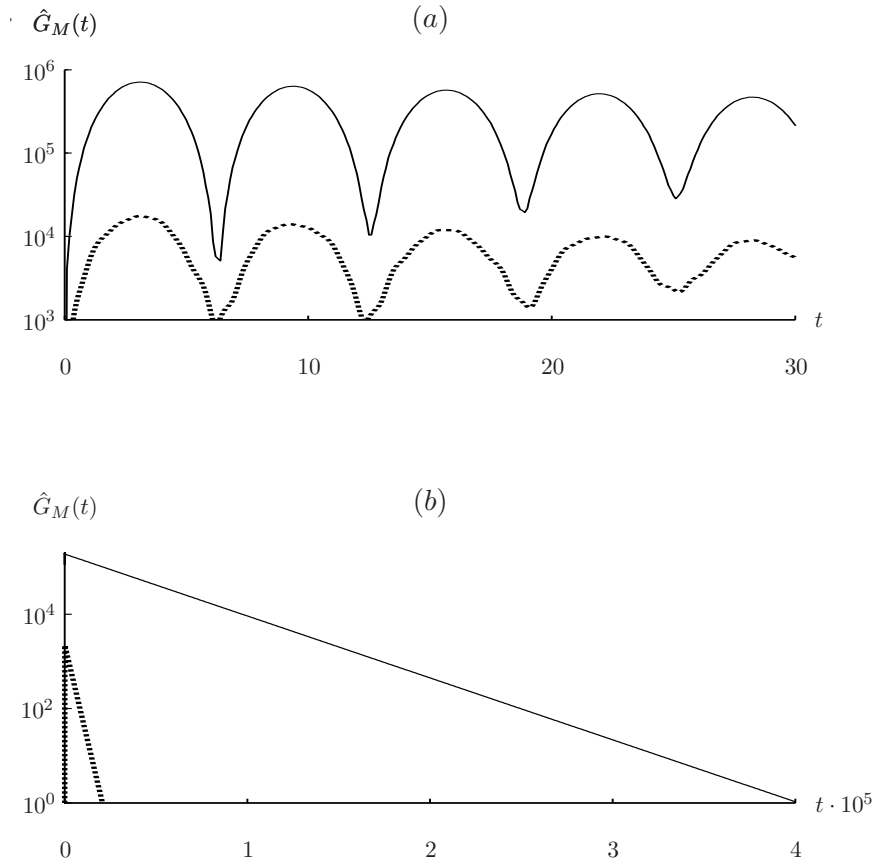
Figure 2.12. Plots of growth functions of the bed potential-energy using a reduction coefficient $c = 10^{-6}$ for case A (solid lines) and case B (dotted lines) considered in figure 2.9 (see the caption for the data). The growth functions during the first stages of perturbation dynamics are reported in panel (a), while only the envelope of the peaks is shown in the panel (a). This is done to clarify the $\hat{G}_M$ behavior for longer times.

to the true **A** operator. The energy components, scaled with the initial perturbation, are reported in figure 2.13 and the scenario is very different from what is shown in figure 2.11. The growth rate of the bed potential-energy is now extremely high ($\approx 10^8$), compared to the growth rate of the kinetic energy ($\approx 10^3 - 10^4$). This means that, with initial condition (2.37), the perturbations of the bed potential-energy are the ones that undergo the greatest growth rate and form the skeleton of the E_M transient growth. The modified energy (2.34) allows one to select initial conditions that have the corresponding evolutions of the perturbation characterized by a temporary transfer of energy from hydrodynamic and free surface modes to the morphodynamic one. Although the growth function $\hat{G}(t)$ always remains lower than the one shown in figure 2.11, the single bed mode experiences a much greater amplification. As a consequence, the nonnormality of operator **A** can drive transient growths that can play a role in bar morphodynamics, as will discussed in the next section.

First, however, it would be useful to evaluate the timescales involved in the morphological transient growth. We focus on two scales: the time when the maximum amplification of energy occurs (i.e., $t_{\max}$) and a time that represents the portion of the growth function where $\hat{G}(t) > 1$. We define this second timescale to be equal to the first-order moment of the area subtended by $\hat{G}(t)$, that is

$$T = \frac{1}{\int_0^{t_1} \hat{G}(t)dt} \int_0^{t_1} t\hat{G}(t)dt, \qquad (2.38)$$

where t_1 is the time when $\hat{G}(t_1) = 1$. For example, for case A and $c = 1$: $t_{\max} = 0.16$ and $T = 396$. For $c = 10^{-6}$: $t_{\max} = 3.1$ and $T = 3.29 \cdot 10^4$.

The timescales evaluated for different wave-numbers are reported in figure 2.14 for case A. It is possible to notice that the timescales corresponding to bed perturbations are considerably longer (one or two orders of magnitude) than the timescales associated with the hydrodynamic perturbations. In both cases, the time associated with the peak of the growth function tends to decrease with the wave number. A weak decrease of T is observable in the case of morphological perturbation, while a strong increment characterizes the hydrodynamic perturbations. It follows that bed

(a)

P_b/P_{b0}

K/K_0

P_s/P_{s0}

10^6

10^4

10^2

10^0

10^{-2}

10^{-4}

0.2   0.4   0.6   0.9   1.0

t

(b)

P_b/P_{b0}

K/K_0

P_s/P_{s0}

10^6

10^4

10^2

10^0

200   400   600   800

t
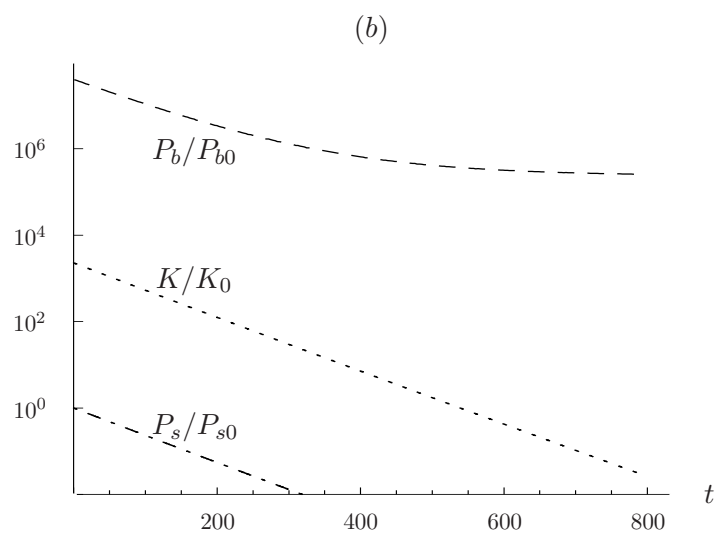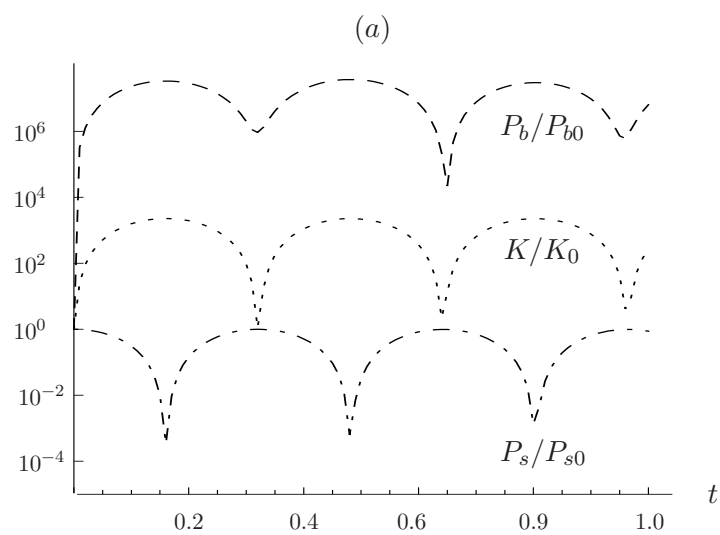
Figure 2.13.   Time behaviour of the different components of perturbation energy, E, scaled to their initial values. The initial condition is the optimal morphodynamic one, $\boldsymbol{q_0}_M$, and the data refers to case A. The evolutions of K/K_0 (dotted lines), P_s/P_{s0} (dot–dashed lines) and P_b/P_{b0} (dashed lines) are shown. Only the peak envelope is shown in the panel on the right.
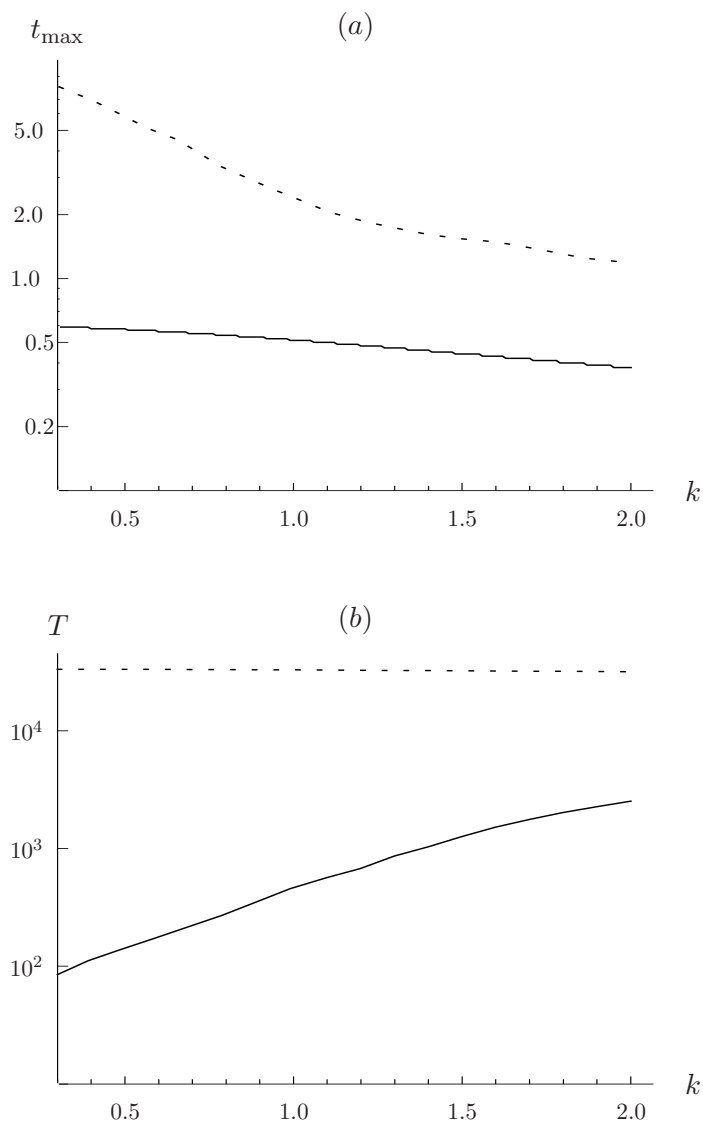
Figure 2.14. Plots of the time scales of the perturbation energy versus the wave number. The panels refer to case A, adopting $c = 1$ (solid lines) and $c = 10^{-6}$ (dotted lines).

perturbations characterized by long wavelength are more persistent than those characterized by short wavelength.

2.4   Bar wavelength evolution

An open question in the field of bar dynamics is the explanation of the progressive increment of the wavelength observed in flume experiments during the first stages of bar formation (Fujita & Muramoto, 1985; Lanzoni, 2000). This increment is also found in numerical simulations of full nonlinear problems (Defina, 2003) and it is generally conjectured to be due to nonlinear interaction between unstable modes. However, conclusive proof is lacking in this sense. In this section, we provide a different purely linear explanation (possibly cooperative with nonlinear processes), based on the strong nonnormality of the algebraic operator governing the linear dynamics of the bed-oriented perturbation energy, E_M.

The key point of our approach is as follows. In the previous sections, we showed that bar dynamics exhibit remarkable transient growths for asymptotically stable wave numbers. If the typical timescales of such transient behaviours are lower than the time that the asymptotically unstable perturbations need to grow and dominate the dynamics (like qualitatively shown in figure 2.3), the dynamical system will show (at least in its linear behaviour) different dominant wavelengths at different times: the wavelengths corresponding to transient growths will occur first, then the asymptotically unstable wavelengths will start to emerge until the most unstable mode remains the only one. If the asymptotically unstable wave numbers are lower than those exhibiting the strongest transient growths, then the dynamical system will exhibit a wavelength that grows in time.

According to this picture, purely linear mechanisms are able to explain the experimental and numerical observations on bar inception. Evidently, the nonlinear processes are necessary for the saturation of the exponential disturbance growth and they can alter the quantitative details of the linear picture, but the core of the wavelength evolution should be dictated by linear wave interactions.

In this section, the region of the parameter space where bar

formation is expected will be focused on (i.e., one positive eigen-value exists). We will show that the previously outlined picture is reasonable, can be borne out by theoretical findings and is coherent with some of our experiments that have been expressly carried out in order to investigate the first stages of bar dynamics.

2.4.1 Description of the experiments

The experiments were carried out in a sediment-fed flume situated in the "G. Bidone" Hydraulics Laboratory at the Politecnico di Torino. For details about the experiemntal facility, see Appendix A The experiments were run as follows. The sand scraper was used to obtain a flat surface with constant slope, the water level in the upstream stilling tank was then increased to supply the prescribed fluid discharge. After a short transitory (about one minute), during which the flowing water filled the entire flume, we observed a uniform flow in the channel. The flow was manteined until the bar pattern reached its asymptotic equilibrium condition (i.e., no significant evolution of the wavelength or amplitude of the bars were observed).

Four cameras, fixed above the flume, recorded the bed configuration at the t_j^* instants. We chose a time interval between two recordings equal to 2.5 minutes. Because of the lack of suspended sediments, the bar pattern was acquired with pixel-precision, which corresponds to 1-1.5 mm, depending on the run. The four pictures recorded by the cameras for each t_j^* instant were merged, and a picture of the entire channel was thus obtained. At this point we measured the N_j wavelengths, $\lambda_{i,j}^*$, occurring at time t_j^* and defined, we recall, as the distance between two consecutive pools or fronts (see figure 2.1). The subscript "j" refers to the time t_j^* at which the bed configuration is recorded, while subscript "i" marks the i-th wavelength measured at the instant t_j^* and varies in the $[1, N_j]$ range . It should be pointed out that in these experiments, it was difficult to monitory the initial evolution of the bed forms with an amplitude of a few sediment grains along the 20 m long channel. During these first stages, the camera resolution, the shadows and the light reflexion due to the water free surface made the identification of the bar front difficult in the aerial pictures taken from the laboratory ceiling. In order to overcome this problem,

(a)

(b)
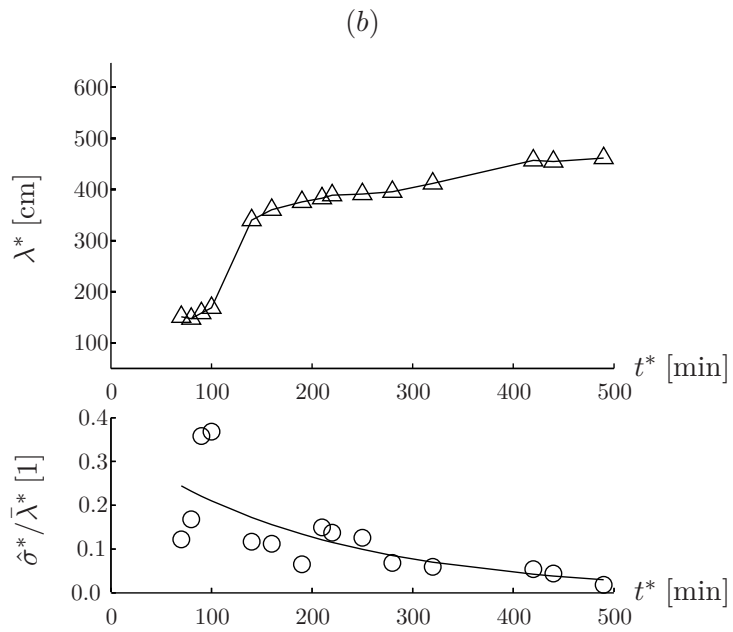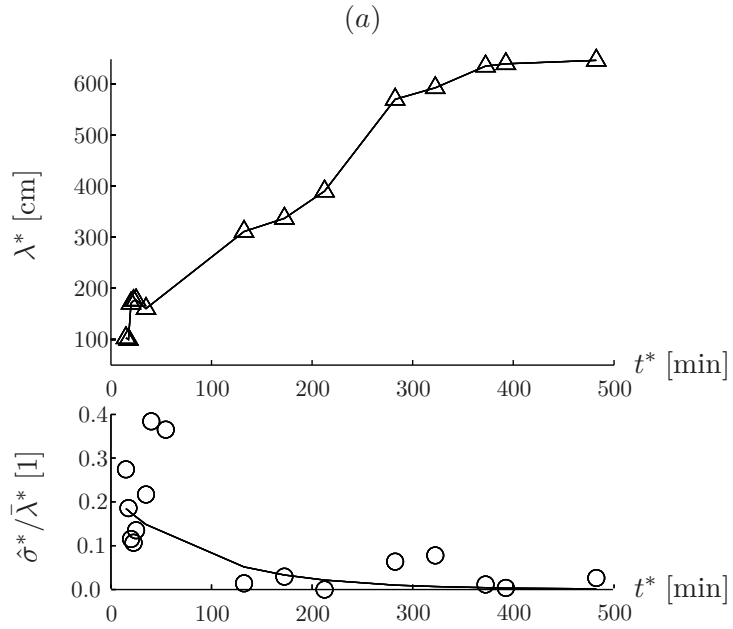
(c)
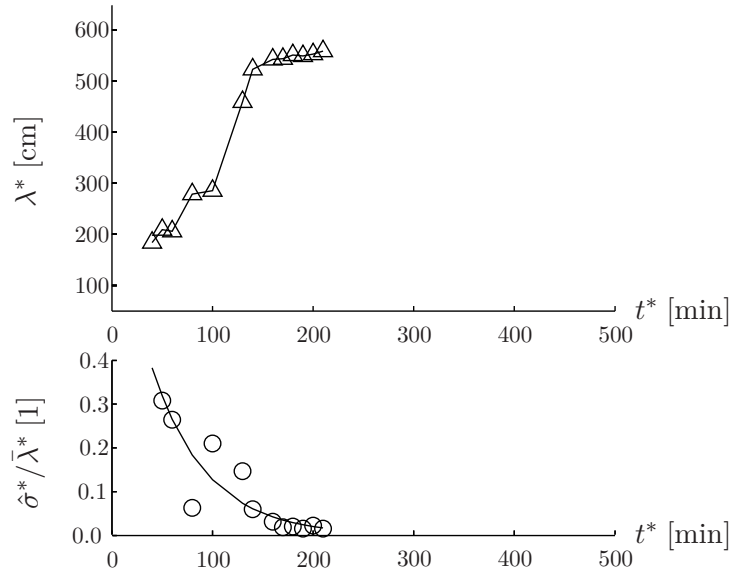
(d)
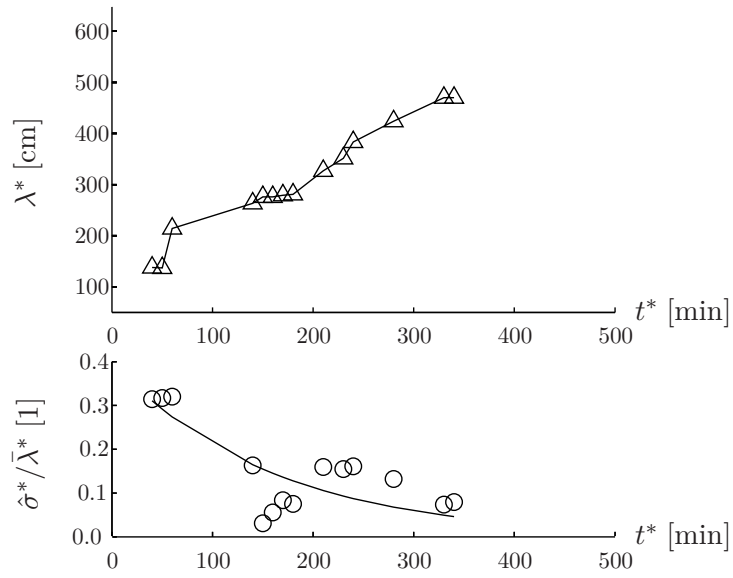
(e)
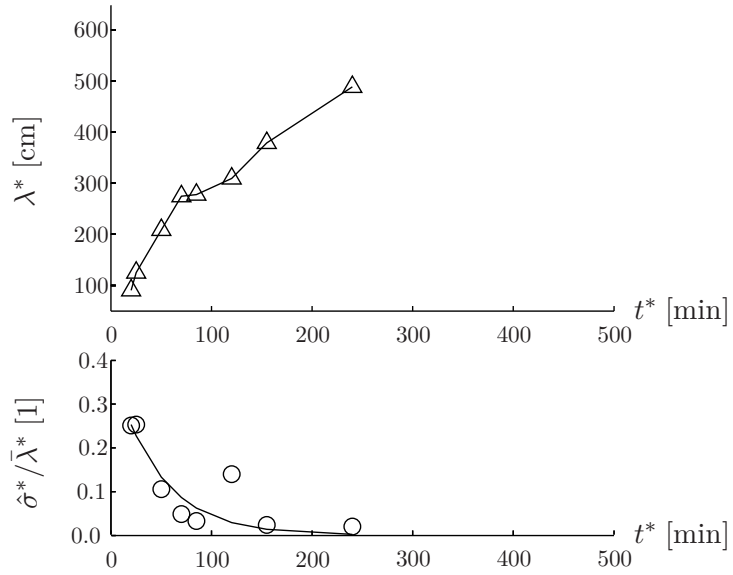
(f)
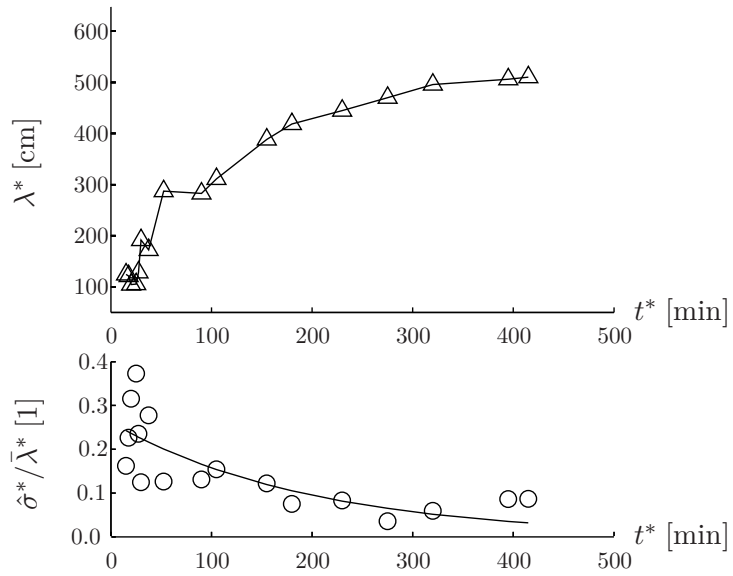
Figure 2.15. Evolution of the wavelengths in the bar pattern. Each panel refers to the corresponding experiments (a-f) reported in table 2.2. In the upper charts the time evolution of the flume-averaged bars wavelength $\bar{\lambda}^*$ (triangles) is reported; in the lower charts the time behavior of the coefficient of variation $\hat{\sigma}^*/\bar{\lambda}^*$ (circles) is shown, and its tendency line, obtained by an exponential fitting of the measured data, is plotted.

the bar fronts were detected (thanks to better illumination conditions) by monitoring the bed form evolution through a direct observation performed standing beside the channel. A reference mark was then placed outside the channel near the front just before each camera recording, so that it could be recognized in the aerial pictures. However, the longer the experiment, the higher the bar amplitudes: this means that when the bar amplitude exceeded about 5 mm, fronts could be detected in aerial pictures without the help of lateral marks. However, it should be pointed out that we were only able to detect bed forms visible to the naked eye, and we therefore missed the very first perturbations, which consisted of a very slight unevenness (fraction of sediment diameters) of the transversal slope of the bed.

We recall that the key parameters that regulate bar dynamics are: (i) the aspect ratio $\beta = 2B^*/D^*$; (ii) the dimensionless sediment diameter d_s, and;(iii) the Shields parameter θ. Operatively, the set of key parameters β, θ, d_s can be modified by varying the liquid discharge Q_l^*, the channel slope S and the channel width $2B^*$ in the experimental setup. Because of (i) the equipment available in the laboratory, (ii) the requirement of turbulent flow and, (iii) the requirement of a sufficiently high aspect ratio to ensure that alternate bars can arise, we were able to vary the key parameters in the following ranges: $\beta \in [14.2, 24.8]$, $\theta \in [0.071, 0.095]$, and $d_s \in [0.025, 0.045]$. It should be noted that the suitability of the aspect ratio was assessed using the simple predictor proposed by Crosato & Mosselman (2008).

We performed several experiments focusing on the investigation of the first stages of alternate bar dynamics. Several runs were repeated to achieve a clear understanding of the investigated phenomena. The initial bar inception mechanism was not always clearly detectable, because it started from a very slight bed deformation with a very small bar amplitude. In addition, the bar growth process during the first phases of the bar dynamics was very sensitive to the bed-load feeding and to the initial bed unevenness. In particular, a bed-load input rate in excess of the equilibrium value can propagate downstream and immediately form a mature bar pattern, skipping all the first stages of bar formation. As a consequence, the results that are shown hereafter correspond to a careful selection of the best runs, in which it was possible to

observe the first phase of bar development. The set of parameters used for the six best flume experiments which produced useful data for the investigation of the bar inception and wavelength selection mechanisms is reported in table 2.2.

Table 2.2.   Set of hydraulic parameters used in the six best runs (in all runs $2B^*$=500 mm).

RUN	θ	β	$10^2 \cdot d_s$	Q_l^*	$10^3 \cdot S$	$10^2 \cdot U_0^*$
	[-]	[-]	[-]	[l·s^{-1}]	[-]	[m/s]
a	0.087	15.4	2.8	2.5	4.0	31
b	0.081	20.8	3.7	1.7	5.0	28
c	0.081	20.8	3.7	1.7	5.0	28
d	0.095	24.8	4.5	1.5	7.0	30
e	0.090	24.3	4.4	1.5	6.5	29
f	0.089	18.9	3.4	2.0	5.0	30

2.4.2   Results
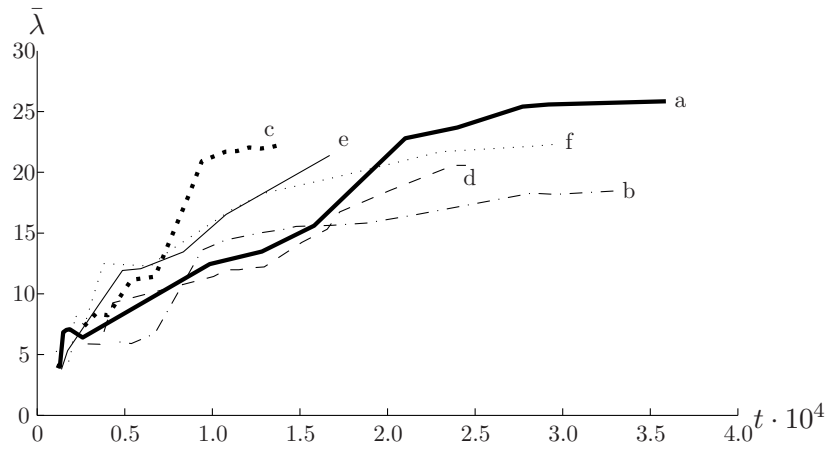
Figure 2.16.   Evolution of the dimensionless flume-averaged wavelength as a function of the dimensionless time, for the six experiments listed in table 2.2.

Our experimental investigation was focused on the dynamics of
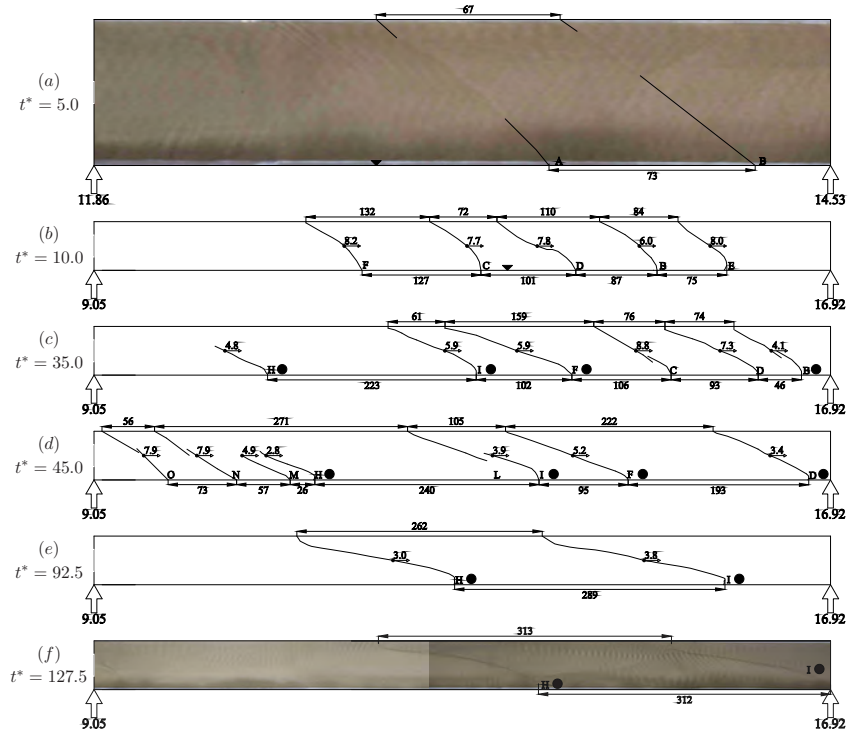
Figure 2.17. Schematic evolution of the channel bottom occurred during run "a". The flow is from left to right. The progressive coordinates (m) of the channel are reported under each photograph. The celerity of each front (cm min^{-1}) is reported above the arrow placed in its midpoint. The bar wavelengths are also indicated (cm). Dimensional time t^* is given in minutes. The slow migrating fronts are highlighted with black circles. In panel (a) we report an enlarged view of the channel, where the early perturbations start to be visible. The black lines in panel (a) are used to highlight the front where the visibility from aerial picture is poor. In order to compare panels (a) and (b) (reported at different scales), a black triangle marking the same point on the channel is placed in the lower edge of the two panels. The short-wave disturbances in panel (a) are not dunes (which were never present in our runs), but small-amplitude instabilities of the free surface.

the bars from their initial occurrence (visible to the naked eye) to the achievement of the asymptotic wavelength. Figure 2.15 reports the experimental results on the wavelength evolution for the six experiments listed in table 2.2. The upper chart in each panel shows the flume-averaged bar wavelength $\bar{\lambda}_j^* = 1/N_j \sum_{i=1}^{N_j} \lambda_{i,j}^*$ at different times t_j^*. The lower charts report the coefficient of variation $\hat{\sigma}_j^*/\bar{\lambda}_j^*$ as a function of time t_j^*, where $\hat{\sigma}_j^* = [1/N_j \sum_{i=1}^{N_j} (\lambda_{i,j}^* - \bar{\lambda}_j^*)^2]^{1/2}$ is the standard deviation of the wavelength distribution. All the data shown in the upper charts in figure 2.15 are displayed in a dimensionless form in figure 2.16, where $\bar{\lambda}_j = \bar{\lambda}_j^*/B^*$ and $t = t^* U_0^*/B^*$ (U_0^* is the bulk velocity in uniform and unperturbed bed conditions).

A careful visual inspection of the aerial photo sequences and the direct observation (standing besides the channel) of the experiments allowed us to identify four distinct phases which characterize the inception and the evolution of bar instability. In order to illustrate these phases, the synthetic and schematic evolution of the channel bottom that occurred during run "a" in table 2.2 is reported in figure 2.17 and is used as an exemplifying case. The complete evolution of the channel bottom, as visible from the original aerial pictures, can be found in Appendix B.

It should be pointed out that, in order to evaluate the average celerity of the bar fronts (which is a key feature of the bar evolution), the downstream displacements of the lower apex and the midpoint of the front (between two subsequent pictures) were measured, and were then averaged and divided by the time between the instants the two pictures were taken. A detailed description of each detected phase is given hereafter.

Phase I begins when the water starts to flow in the channel. Figure 2.17*a* shows the very first bar instabilities (fronts A and B) observable in run "a" and which occur after 5 minutes from the start of the run. The average wavelength of the first visible perturbations is $\bar{\lambda} = 2.8$ ($\bar{\lambda}^* = 70$ cm). After another 5 minutes (figure 2.17*b*), the pattern has expanded to a longer portion of the channel: front A has disappeared, but the new C,D,E and F fronts have become visible. These fronts have an average wavelength of $\bar{\lambda} = 3.9$ ($\bar{\lambda}^* = 98$ cm) and an amplitude of a few grain diameters. It is a key point to observe that these first bars propagate downstream with a rather uniform celerity. The average celerity is $v_p^* = 7.5$ cm

min^{-1}, while the maximum and minimum registered values are 8.2 and 6.0, respectively. The first phase ends when the bars start to exhibit very different celerities.

The qualitative sequence characterizing the first phase – i.e., single bars start to occur and then new bars with similar celerity and a short wavelength emerge – is the same sequence that is also observed in the other runs, even though the number of the first visible bars, their wavelengths and time occurrences vary significantly, according to the specific run. A data synthesis is given in table 2.3, where, for each run listed in table 2.2, we report: (i) the dimensionless time, t_{vis}, from the beginning of the run after which the first bars become visible, and (ii) the dimensionless wavelengths λ_i of all the bars that compose the first detectable pattern (i.e., measured at t_{vis}). It can be observed that the time required for the pattern to become visible varies significantly, and ranges from 370 to 4705 (in dimensional units, from 5 to 70 minutes). The sorting of wavelengths can also vary significantly. Let us consider, for instance, experiments "c" and "e": in the former, at $t = t_{\mathrm{vis}}$, a bar with a wavelength of 300 cm coexists with a bar with a wavelength of 110 cm, while in the latter the two extreme values of the wavelengths are 74 and 122 cm. This high variability in the characteristics of the early bar pattern are likely due to the different initial conditions that affect the system. Notice that a detailed explanation and comments on the effect and importance of the initial condition is given in section 2.4.3.

In order to contextualize our results in the frame of existing theories, table 2.3 also reports: λ_{asy}, namely the corresponding most unstable wavelength resulting from the linear stability theory presented in section 2.2.2 and λ_{min}, which is the shortest asympotically unstable wavelength, according to the same theory. The data in table 2.3 reveal that the average wavelength of the first emerging bars is generally lower than the equilibrium pattern (defined by λ_{asy}) and that several wavelengths of the first bar pattern should not emerge at all, since $\lambda_i < \lambda_{\mathrm{min}}$.

Figure 2.17 reveals that the first fronts have the same inclination, and that the disposition in alternate fronts is actually missing. This is due to a slight and imperceptible transversal unevenness of the bottom slope, which facilitates front growth in one direction, but only during the first stages. It should be emphasized that this

feature is common in experiments concerning alternate bars – for instance, the portion of channel between 8 and 14 m at $t^*=$17'45" reported in figure 2.2 and characterized by fronts inclined in the same direction – and that the well known alternate configuration is always recovered as time increases (see figure 2.17f).

Table 2.3. Features of the first detectable bar pattern for the corresponding a-f runs reported in table 2.2.

RUN	a	b	c	d	e	f
t_{vis}	370	4705	2690	2880	1390	1080
λ_1	2.68	5.52	12.00	7.96	2.96	5.16
λ_2	2.92	6.56	10.96	6.76	3.72	4.76
λ_3			7.76	4.84	4.88	4.96
λ_4			4.96	4.80	4.00	6.24
λ_5			4.40	5.00	3.32	
λ_6			5.04			
λ_{asy}	10.64	9.64	9.64	8.96	8.72	9.80
λ_{min}	5.24	5.12	5.12	5.44	5.48	5.24

Phase II begins when fronts with remarkably different celerities can be observed at the same time in the channel. For instance, consider panel (c) in figure 2.17: fronts H, I, F and B (marked with a black circle) migrate downstream with an average celerity $v_p^* = 5.1$ cm min^{-1}, while fronts C and D move with an almost double celerity: $v_p^* = 8.1$ cm min^{-1}. Slowly migrating fronts generally correspond to long wavelengths ($\lambda_{\text{slow}} \simeq 7.6$, $\lambda_{\text{slow}}^* \simeq 190$ cm), while fast moving fronts have a shorter wavelength ($\lambda_{\text{fast}} \simeq 3.7$, $\lambda_{\text{fast}}^* \simeq 95$ cm) that is similar to that measured during phase I. Since $\lambda_{\text{slow}} > \lambda_{\text{fast}}$, it follows that slower bars are much closer to the equilibrium wavelength foreseen by the linear theory (in this case $\lambda_{\text{asy}}=10.6$). It should also be noted that some fronts can disappear during phase II, as does front A which was detected in phase I. In the next section, this behavior will be explained in detail, as a result of the nonnormality that affects the dynamical system.

The celerity difference in the fronts entails that fast migrating fronts are destined to reach and amalgamate with the slower

bar front downstream. The effects of the celerity difference is evident if we compare panel (c) in figure 2.17 with panel (d). It can be observed that: (i) front C has disappeared; (ii) front D has reached a wavelength close to λ_asy, and it has slowed down, becoming a slowly moving front; (iii) fronts I and F, despite being quite close to each other ($\bar\lambda$=4.0), are still migrating downstream together with an average celerity $v_p^* = 4.6$ cm min^{-1}; (iv) a new emerging front L has appeared upstream from front I. Front L was likely already between fronts H and I in panel (c), but the aerial pictures did not detect it because of its very modest amplitude. In panel (d), front L has almost reached front I, with which it will soon be amalgamated; (v) three distinct fronts, characterized by a short wavelength ($\bar\lambda$=2.1), have appeared upstream from front H. As they have a higher celerity ($\bar v_p^* = 6.9$ cm min^{-1}) than front H ($v_p^* = 2.8$ cm min^{-1}), they soon reach and amalgamate with the latter.

Details of the amalgamation of a fast front reaching a slow one are shown in figure 2.18. The pictures were taken using a camera placed by the channel walls. Because of the favorable light conditions and the short distance between the camera and the channel, the bar fronts are clearly visible. It is possible to observe that the fast bars amalgamate with the slow bars, with a consequent rapid increase in the perturbation amplitude.

The results of the amalgamation processes are shown in figure 2.17e, where it is possible to observe that the average wavelength ($\bar\lambda$=11.0) is very close to the value given by the linear theory. The agreement can be considered very good as the amplitude of the perturbations (despite a marked increment (compared to the perturbations visible in figures 2.17a - 2.17b) is still modest in this phase, and nonlinearities still play a minor role. Conventionally, phase II ends when all the fast moving fronts have been amalgamated or dissipated, and the remaining fronts move with uniform celerities (e.g., $\bar v_p^*$=3.4 cm min^{-1} in run "a").

The amalgamation of fast moving fronts entails an increase in the mean wavelength of the bar pattern (see the upper charts in figure 2.15). During our experiments, we observed both abrupt and regular increases. A remarkable example of abrupt increase can be seen in figure 2.15 for run "b": the average wavelength is about 1.5 m ($\bar\lambda = 6.0$) for the first 100 minutes (t=6720), then

the amalgamation process occurs and the average wavelength has jumped to 3.50 m ($\bar{\lambda} = 14.0$) after only 20 minutes. The same behavior is also detectable for run "f" about time $t = 3600$ (50 min). An example of a more regular increase is instead detectable for runs "a" and "d". However, a key aspect common to all the runs is the drastic reduction in the coefficient of variation $\hat{\sigma}_j^* / \bar{\lambda}_j^*$, which is attributable to the amalgamation of the fast fronts with the slow ones (see the lower charts in figure 2.15). Let us consider, for instance, figure 2.17d. The presence of the three fronts upstream from front H means that long waves ($\lambda \simeq 10$) coexist with short waves ($\lambda \simeq 3$), and this leads to a high value of the coefficient of variation ($\hat{\sigma}_j^* / \bar{\lambda}_j^* = 0.4$). When all the fast fronts have dissipated (figure 2.15e), the pattern is much more regular and the coefficient of variation reduces sensibly ($\hat{\sigma}_j^* / \bar{\lambda}_j^* = 0.04$). It should be noted that, a rise in the hydraulic resistances, due to the increase in bar amplitude is observed after the amalgamation has taken place.

Phase III starts when the competition between the different wavelengths has finished (i.e., all the fast fronts have been amalgamated with the slower ones or have been dissipated), and only one class of bar characterizes the channel bed (figure 2.17e). During phase III, the wavelengths of such alternate bars increase regularly until an asymptotic value is reached and a uniform wavelength is selected along the whole channel (the coefficient of variation $\hat{\sigma}^* / \bar{\lambda}^*$ reduces to zero). It should be noted that the equilibrium wavelength reached at the end of the run is generally slightly longer than λ_{asy}. This is due to the nonlinearities that affect the system at longer times.

Phase IV is characterized by a statistical steady state, which exhibits a well-formed bar pattern in which the wavelengths fluctuate around an asymptotic value of about ten times the channel width (figure 2.16). It is worth noticing that the well-known tendency of the wavelength to weakly grow downstream along the channel (Lanzoni, 2000) is also present in our experiments.

Before concluding the description of the experimental results, it is worth stressing that short timescales are involved in phases I and II. A quick glance at figure 2.15 reveals that the time required for the bar pattern to reach its asymptotic equilibrium configuration is of the order of 400 minutes, while the inception of the early visible bar pattern and the successive bar front interactions takes place in

(a)

(b)

t

(c)

$t^* - t_a^* = 30 \text{ s}$

(d)

$t^* - t_a^* = 178 \text{ s}$

(e)

$t^* - t_a^* = 214$ s

(f)

$t^* - t_a^* = 272$ s
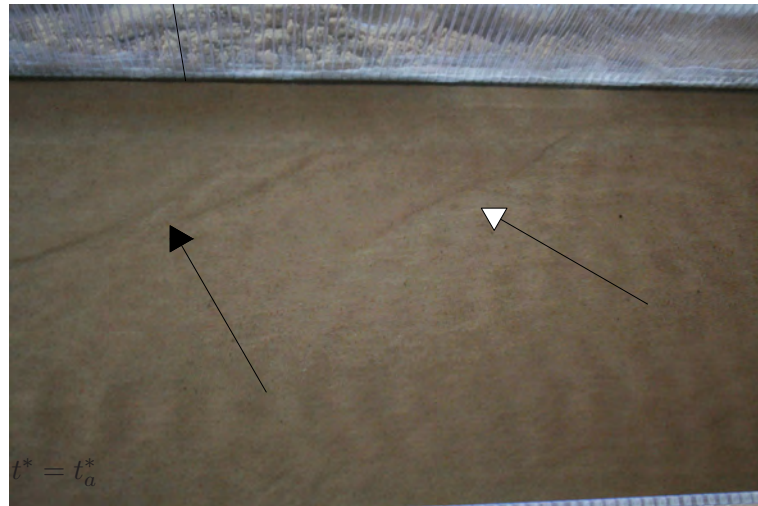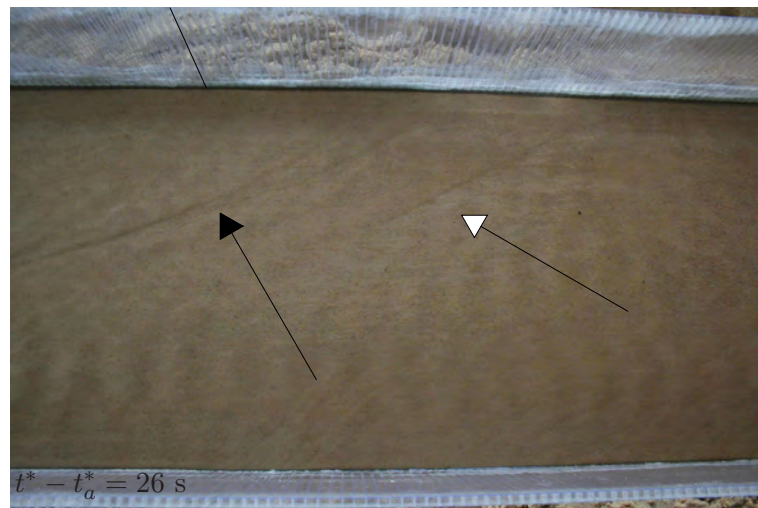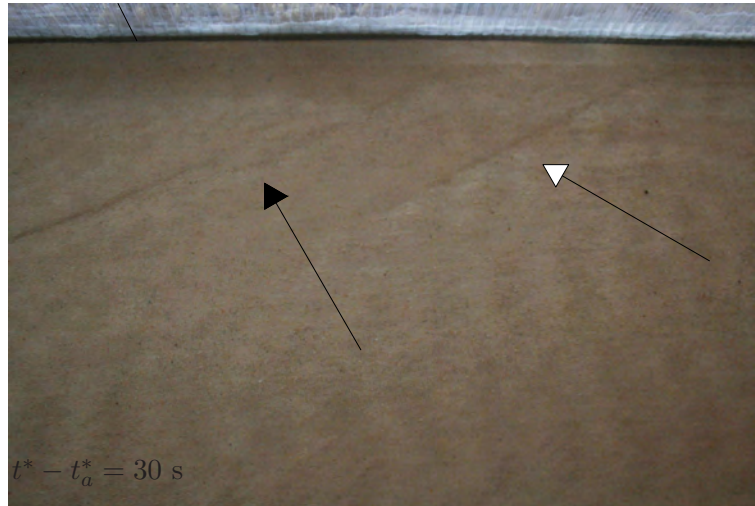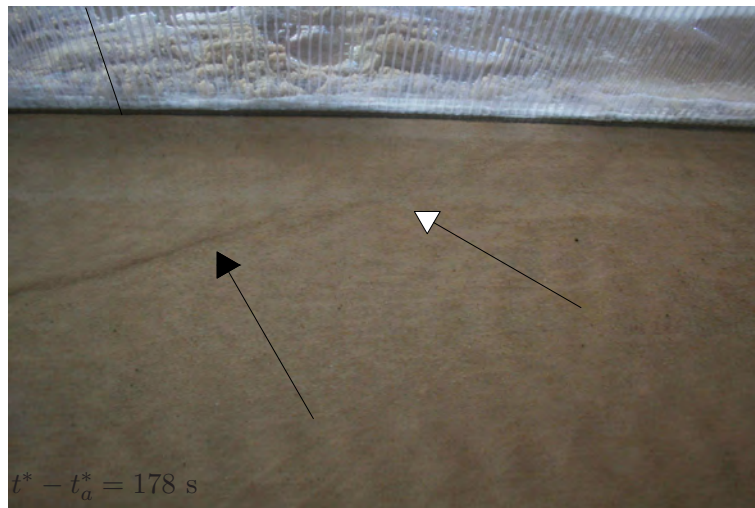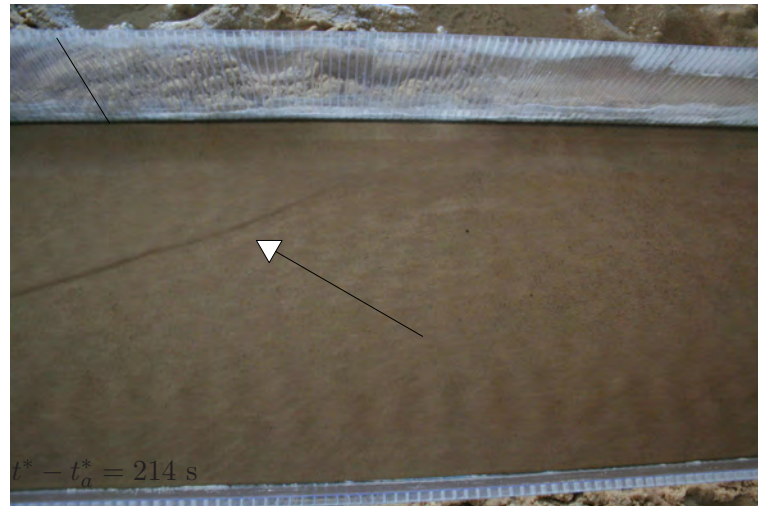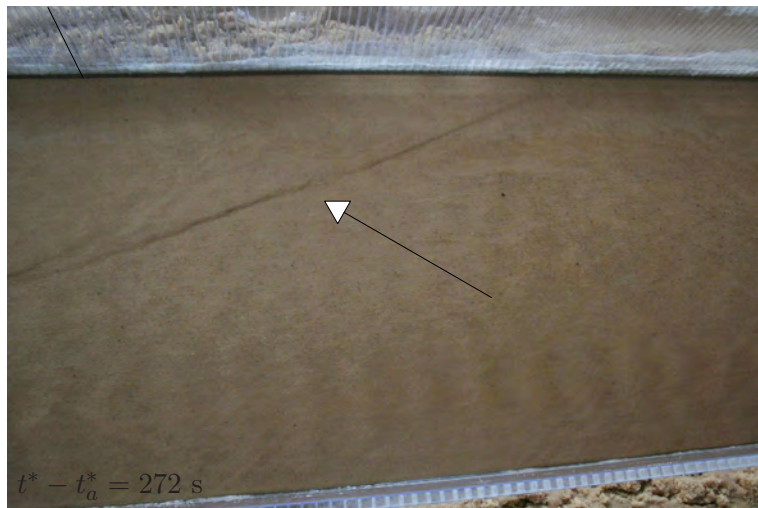
Figure 2.18. Details of an amalgamation process occurred during run "a". The arrows with a white head indicate a slowly moving front, while the arrows with a black head indicate a fast moving front. Flow is from left to right. A vertical black line painted on the right side wall marks a reference point useful to observe how the bed evolves while time is running. We recall that the channel is 0.5 m wide.

a time interval of the order of tens of minutes.

In the following sections, we provide a possible theoretical explanation for the experimental observations, based on the linear wave interaction triggered by the nonnormality of the differential system governing the bar dynamics introduced in section 2.3. A theoretical approach based on a linear analysis of the initial boundary value problem can explain the early stages of bar formation in a satisfactory way. On the contrary, one of the most common explanations for the lengthening of the bed forms involves the impact of nonlinearities of the flow field on the sediment transport dynamics, which become significant with an increase in the bed form amplitude. As a matter of facts, experiments have reported that wave lengthening is active soon after the inception of instability, where the core dynamics should not yet be affected by nonlinearities, and a linear analysis should be actually acceptable. On the contrary, the asymptotic wavelength predicted by linear models fits well the experimental outcomes .

2.4.3   Interpretation of the experimental results

In this section we provide an explanation of the phenomena presented in section 2.4.2, leading to the wavelength selection occurred during the bar instability inception, through the mathematical framework introduced in section 2.3. In particular, we show how the remarkable nonnormality – detected in the bar dynamics through the analysis of the algebraic operator governing the linear dynamics of the bed-oriented perturbation energy E_M – can explain the findings of the experiments discussed in the subsection 2.4.2.

In the previous section, we demonstrated that the nonnormality of bar differential operator leads to a significant transient transfer of energy among the hydrodynamic modes and the morphodynamic one. This causes remarkable transient growths of the bed potential energy even for asymptotically stable wavenumbers. As hydrodynamic modes are involved in such energy transfer, the typical timescales of transient behaviors are expected to be lower than the time that the asymptotically unstable bed perturbations need to grow, to become mature bars, and to dominate the dynamics. It follows that the dynamical system will show (at least in its linear

behavior) different dominant wavelengths at different times: the wavelengths activated by the transient exchange of energy between hydrodynamic and morphodynamic perturbation will occur first, then the asymptotically unstable wavelengths will start to emerge until the most asymptotically unstable mode remains the only one. If the asymptotically unstable wave is longer than those exhibiting the strongest transient growths, then the dynamical system will exhibit a wavelength that grows in time. According to this picture, purely linear mechanisms are therefore able to explain the experimental observations of section 2.4.2. Evidently, nonlinear processes are necessary for the saturation of the exponential disturbance growth and they can alter the quantitative details of the linear picture, but the core of the wavelength evolution should be dictated by linear wave interactions.

The key aspects of our explanation are illustrated in figure 2.19, which shows the dependence of the growth function $\hat{G}_M$ on the wave number k at different times, evaluated for the same set of parameters β, θ, d_s used in run "a" of figure 2.17 (notice that if the set of parameters β, θ, d_s are changed, the mechanisms remain unvaried). By plotting $\hat{G}_M$ as a function of k, evaluated at given time, we can detect which harmonics undergo the highest amplification. The growth function referring to the modified energy E_M (see relation 2.34) is chosen in order to focus on the bed modifications. Moreover, the analysis is restricted in the $k \in [0,4]$ range since higher values of wavenumber are not correctly accounted by shallow water equations. The wavenumber corresponding to the most asymptotically unstable mode (in this case: $k_{\mathrm{asy}} = 0.59$, $\lambda_{\mathrm{asy}} = 10.6$) is highlighted in each panel of figure 2.19 by a vertical dashed line, while the average bar wavenumber of the short-wavelength bars observed during phases I and II in the experiment of figure 2.17 (i.e., $\bar{k} = 1.7$) is marked by a downward arrow. The average bar wavenumber observed at the beginning of phases III (figure 2.17e, $\bar{k} = 0.57$) is marked by an upward arrow. The times $\hat{t} = t/t_{\mathrm{asy}}$ refer to the time t_{asy} when all the transient growths have faded away and only the asymptotically unstable modes remain and dominate the behavior of the linear system. We have assumed $t_{\mathrm{asy}} = 5000$ to be a reasonable value (but other choices do not lead to significant changes in our explanation). The parabola-like behavior of $\hat{G}_M(k)$, which can be observed in panel (i), corresponds to the

93

amplification of the asymptotically unstable modes, namely those detectable by the dispersion relation of the usual stability analysis. In order to clarify figure 2.19, the behavior of $\hat{G}_M(k, \hat{t}=1)$ – rescaled vertically so that $\hat{G}_M(k=k_{\text{asy}}, \hat{t}=1)=\hat{G}_M(k=k_{\text{asy}}, \hat{t})$ – is reported in all the other panels with a dotted line. In this way, the asymptotically unstable modes are immediately identified in any panel, while the wave numbers outside the parabola-like dashed line correspond to modes that are asymptotically stable (that is, they go to zero for $t \to \infty$). Notice the good agreement between the theoretical prediction and the measured (before the activation of strong nonlinearities) value of the asymptotic wavelength.

The figure clearly shows that the asymptotically unstable wave numbers do not dominate the dynamics in the first stages. On the contrary, a wide family of disturbances with lower wavelengths than those of the unstable waves exhibits very strong transient amplifications, due to the nonnormality of the dynamical system (it should be recalled that $\hat{G}_M(k, t)$ is proportional to the amplitude of the disturbance with wave number k). In particular, during the first phases of the bar inception process, short (asymptotically stable) waves amplify to such an extent that their amplifications exceeds those of the asymptotically unstable waves (see figures 2.19a-2.19c). This explains why in table 2.3 one can find wavelengths that are shorter than the shortest asymptotically unstable wave predicted by the asymptotic stability analysis, and, in general, much shorter than the most amplified asymptotically unstable waves. Then, while time increases, the wavenumber for which $\hat{G}_M(k)$ is maximum decreases (i.e., the peaks are $k \simeq 3$ in figure 2.19b, $k \simeq 2.5$ in 2.19c and $k \simeq 2$ in 2.19d). Notice that the maximum value of $\hat{G}_M(k)$ reduces as well. This process evolves until $\hat{G}_M(k)$ shows two approximately equal maxima (figure 2.19d): one very close to k_{asy} and the other practically coincident with the average value of the short-wavelength bars observed during the experimental run. From this point, the peak corresponding to k_{asy} begins to prevail, a weak knee in the behavior of $\hat{G}_M(k)$ occurs for a short period (see figure 2.19e), but the amplification of all the asymptotically stable waves tends to decay. This process continues until the transient growths disappears and only asymptotically unstable modes survive and dominate the (linearized) bar dynamics.

The picture that emerges from figure 2.19 is coherent with the

(a)

$\hat{G}_M(t) \cdot 10^8$　　　　$\hat{t} = 0.010$

(b)

$\hat{G}_M(t) \cdot 10^8$　　　　$\hat{t} = 0.015$

(c)

(d)

(e)

$\hat{G}_M(t) \cdot 10^8$ $\hat{t} = 0.040$

(f)

$\hat{G}_M(t) \cdot 10^8$ $\hat{t} = 0.050$

(g)

(h)

(i)
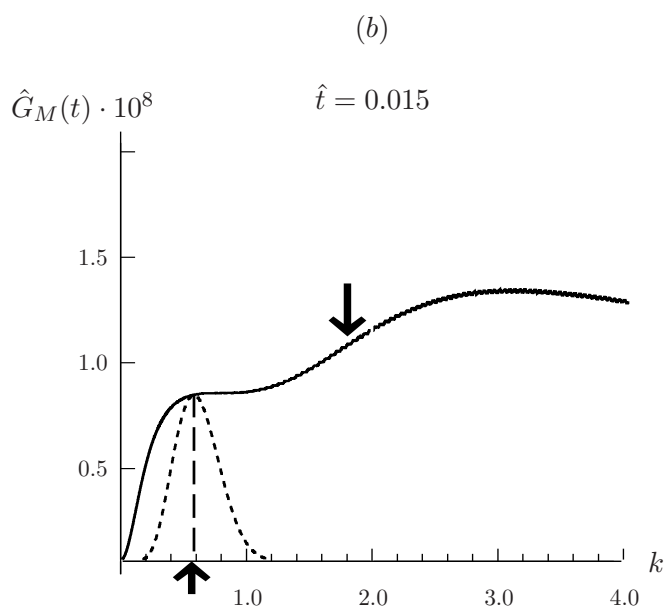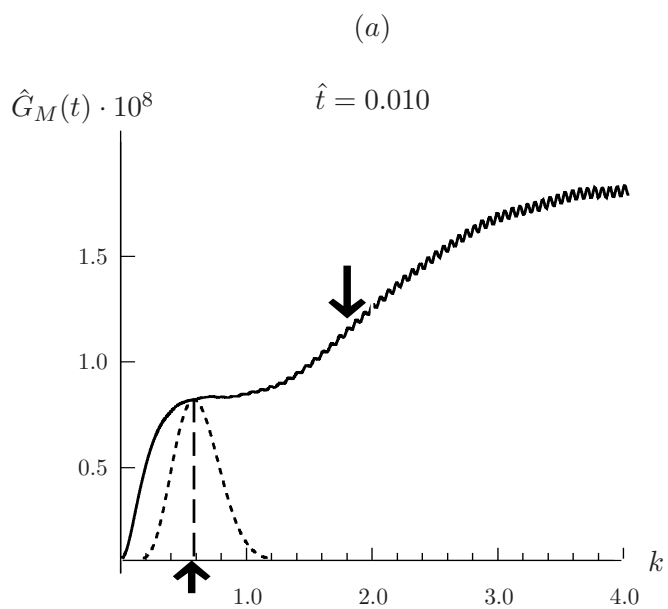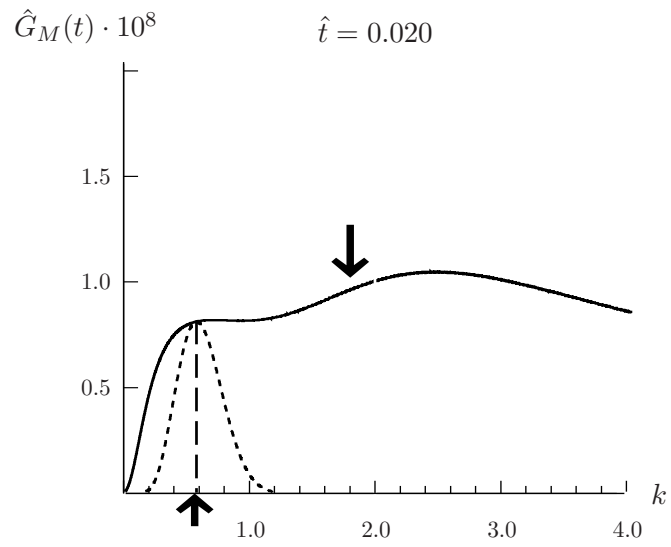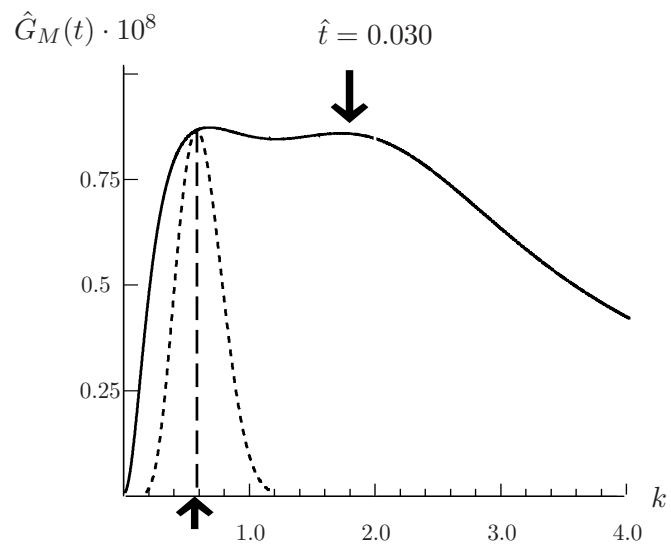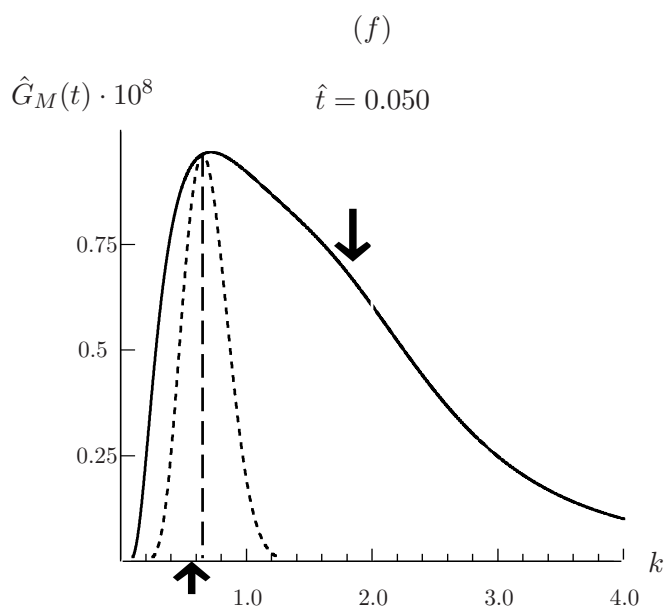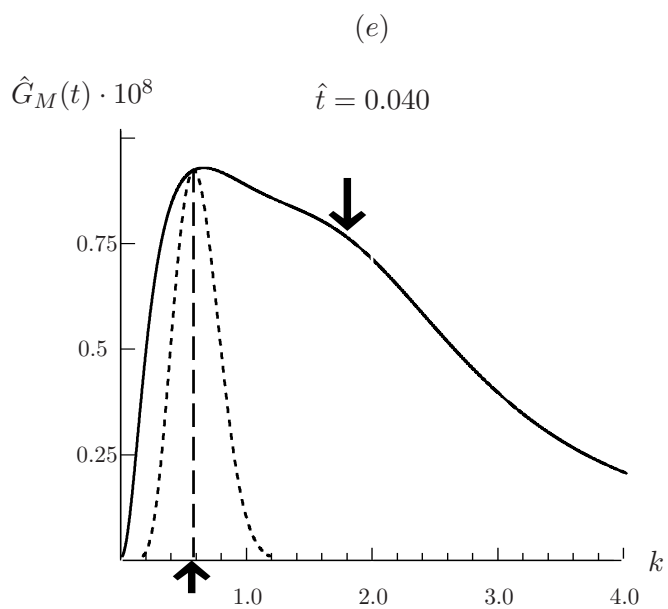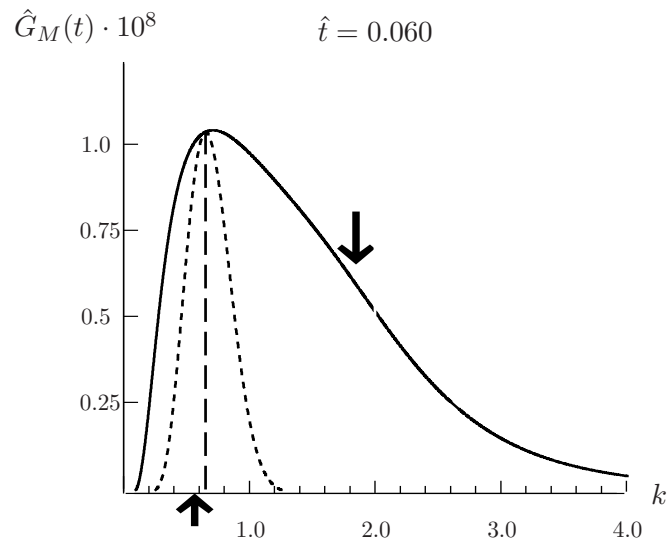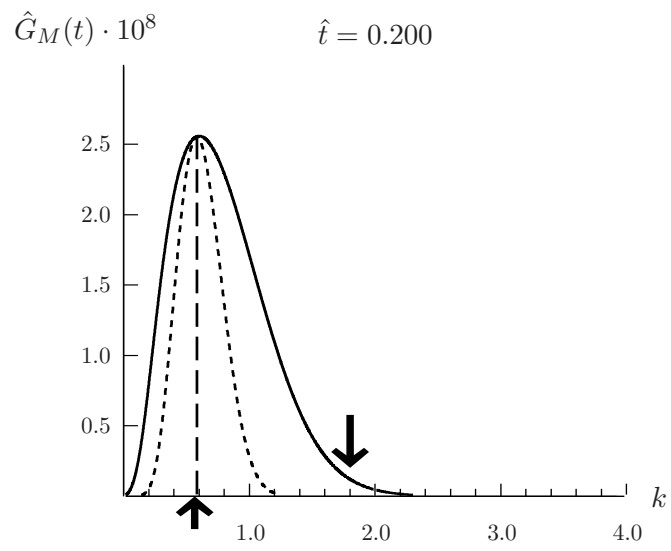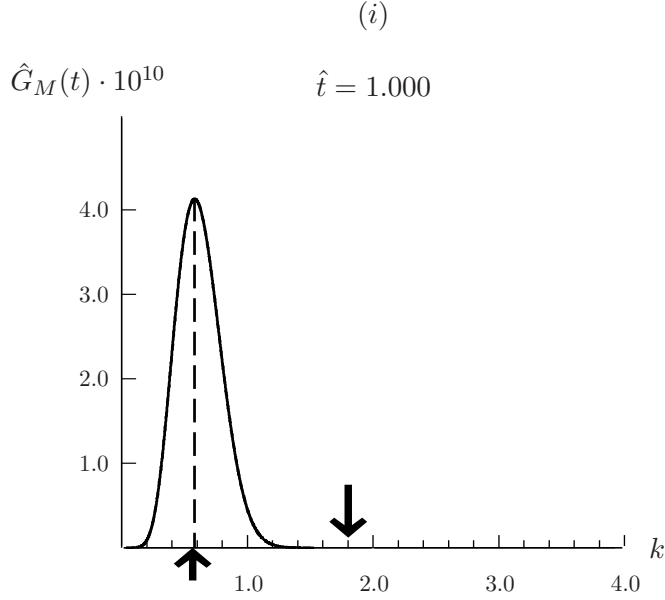
Figure 2.19.   Behavior of $\hat{G}_M$ as a function of the wave number, k, for fixed times. The vertical dashed line indicates the most asymptotically unstable wave number ($k_{\mathrm{asy}} = 0.59$). The downward arrow marks the average wave number ($\bar{k} = 1.7$) of the short-wavelength bars observable during phases I and II of run "a". The upward arrow marks the average wave number ($\bar{k} = 0.57$) of the bars observable during the beginning of the phase III of run "a". The parabola-like dotted line corresponds to the rescaled $\hat{G}_M(k, \hat{t} = 1)$ curve. Initial plane bed condition are considered and: $\beta = 15.4$, $\theta = 0.087$, $\theta_c = 0.050$, $d_s = 2.8 \cdot 10^{-2}$, $c = 10^{-6}$.

results of the flume experiments. It explains the evident increment of the wavelength from the first short low-amplitude bars until the final mature bars occur, as reported also in figure 2.16. The single short bars activated along the channel exhibit a range of wavelengths – remember the high coefficient of variation in the phase I and II (see figure 2.15) – that testifies the existence of an interval of wave number characterized by remarkable transient growths (see figures 2.19a-2.19e in figure 2.19). The same figure shows that a well defined peak is not expected in this interval. This means that: (i) the (time-dependent) most amplified wavenumber coexists with

a range of less amplified wavelengths, justifying the high value of coefficient of variation reported in figure 2.15 for the initial times; and (ii) different infinitesimal and uncontrollable initial conditions lead to a different selection of the initial wavelengths.

When comparing the theoretical results shown in figure 2.19 with the laboratory experiments, it should be taken into account that the linear theory describes the dynamics of infinitesimal perturbations, while only finite amplitude perturbations can be observed in the experiments. We have demonstrated that wavelength selection dynamics is the result of a linear process driven by the nonnormality of the system. Nevertheless, nonlinearities do affect the growth of perturbations from infinitesimal to a finite amplitude. The seed of the perturbation dynamics is therefore given by linear mechanisms, but nonlinearities control the perturbation growth up to a finite amplitude, which is the bar height detectable in experiments. This process can cause a delay between the actual evolution time visible in the experiments and with respect to the linear theory prediction and explains why transient growths at hydrodynamic timescales are experimentally detectable in the bed morphology at longer timescales. However, it should be noted that the nonnormality-induced bar wavelength dynamics observed in our experiments take times of the order of tens of minutes and mature bars evolve with timescales of several hours. The timescale ratio is therefore in good agreement with that foreseen by the theory.

It should be stressed that the scenario depicted in figure 2.19 would be totally different if the system had been normal: the asymptotically unstable waves would have been dominant since the initial times and the same (rescaled) parabola-like $G_M(k)$ behavior would have occurred at any time.

It is also useful to compare the experimentally measured bar celerity with the theoretical predictions. It has been observed (see figure 2.17 and 2.18) that bars with shorter wavelengths move downstream faster than bars with longer wavelengths and this promotes an amalgamation process among the different bars. Such a difference in the bar celerity is well described by means of the usual asymptotic stability analysis, once the reason why different wavelengths temporarily coexist in the dynamics has explained from a non-normal point of view (see figure 2.19). Consider for instance

figure 2.17c. The fast fronts (C,D) have an average wavenumber $\bar{k}_{\text{fast}} = 1.7$ and a celerity $\bar{v}^*_{p,\text{fast}} = 8.1$ cm min^{-1}. The slow front B, instead has an average wavenumber $\bar{k}_{\text{slow}} = 0.6$ and a celerity $\bar{v}^*_{p,\text{slow}} = 4.1$ cm min^{-1}. The ratio between such experimentally measured celerities is $\bar{v}^*_{p,\text{fast}}/\bar{v}^*_{p,\text{slow}} = 2.0$. The ratio between the corresponding theoretically computed celerities is $v_p(\bar{k}_{\text{fast}})/v_p(\bar{k}_{\text{slow}}) = 2.7$, which is quite in good agreement. A further example is contained in figure 2.17d. The fast fronts O,N have an average wavenumber $\bar{k}_{\text{fast}} = 2.5$ and a celerity $\bar{v}^*_{p,\text{fast}} = 7.9$ cm min^{-1} (front M is disregarded as it is too close to front H and a nonlinear amalgamation process has already started). The slow front H, instead provides $(\bar{k}_{\text{slow}}, \bar{v}^*_{p,\text{slow}}) = (0.6, 2.8$ cm min$^{-1})$. The ratio of celerities is $\bar{v}^*_{p,\text{fast}}/\bar{v}^*_{p,\text{slow}} = 2.8$, while its theoretical prediction is 3.8, which is reasonable.

We conclude this section by mentioning that the conceptual picture depicted in figure 2.19 is coherent with the experiments of Fujita & Muramoto (1985). For example, in figure 2.20, we report some plots of $\hat{G}_M(k)$, at a fixed time, for the parameters corresponding to the H-2 run described by Fujita & Muramoto (1985). The arrow marks the average wave number of the bar pattern ($\bar{k} = 1.2$) that Fujita and Muramoto indicated as the initial one visible to the naked eye (which corresponds to the second row shown in figure 2.2), while the vertical line indicates the most asymptotically unstable wave number. Exactly as in our experimental findings, strong transient growths of asymptotically stable wavelengths are activated by nonnormality during the first stages of bar formation. These disturbances then decay and asymptotically unstable longer waves emerge more and more until the final dominant wavelength is reached.

2.5   Conclusions

In this chapter, the wavelength selection that occurs during the inception of bar instability has been experimentally investigated and theoretically interpreted.

Firstly, we went beyond the classical linear stability analysis – carried out by means of normal modes (where only the asymptotic fate of the disturbances is focused on)– and we studied the transient

(a)

$\hat{G}_M(t) \cdot 10^8$ $\hat{t} = 0.020$

(b)

$\hat{G}_M(t) \cdot 10^8$ $\hat{t} = 0.030$

(c)

$\hat{G}_M(t) \cdot 10^8$ $\hat{t} = 0.060$
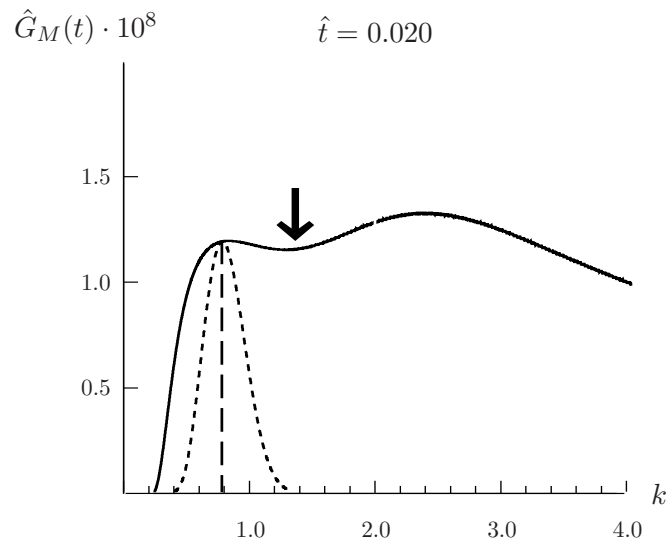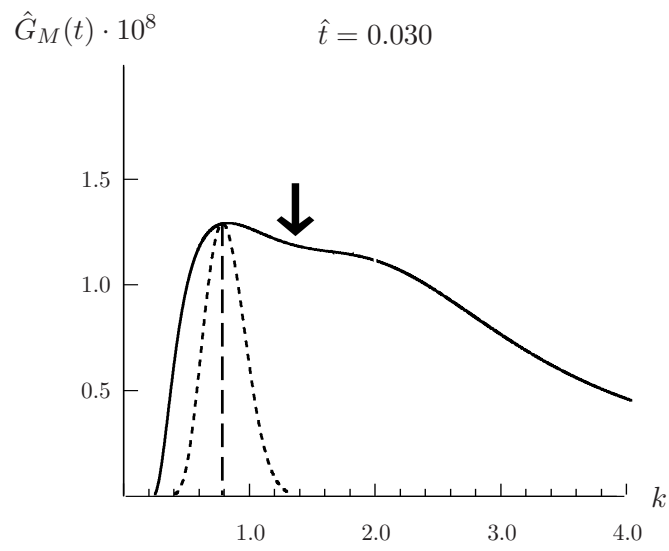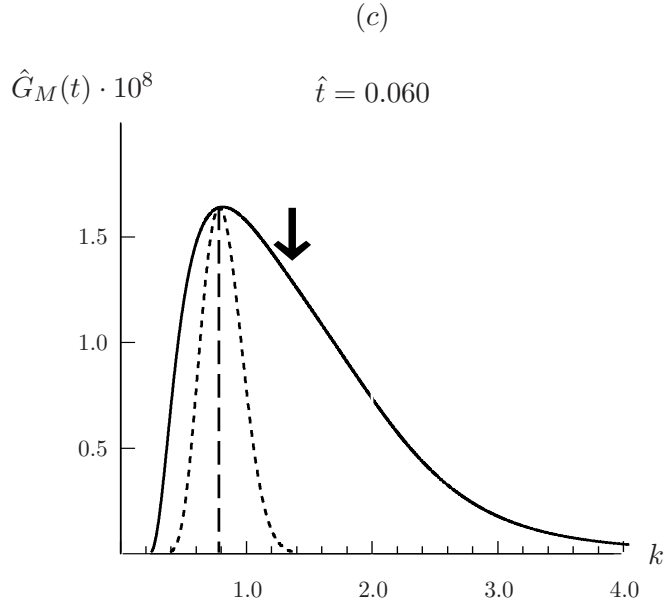
Figure 2.20. Plots of $\hat{G}_M$ as a function of the wave number k for the run H-2 which was experimentally investigated by Fujita & Muramoto (1985). The asymptotic wave number ($k_{asy} = 0.58$) is indicated with a vertical dashed line, and the arrow indicates the wave number of the first perturbation pattern which was possible to observe with the naked eye ($\bar{k} = 1.2$). The parameters are: $\beta = 12$, $\theta = 0.065$, $\theta_c = 0.050$, $d_s = 4.7 \cdot 10^{-2}$, $c = 10^{-6}$. Initial plane bed conditions are considered. For the meaning of the parabola-like dotted line, see figure 2.19.

behavior of the system. Our choice was motivated by the fact that, during the inception phase of bar instability, the amplitude of the perturbation is so small that the dynamics of the system is well represented by a linearized model. The inability of some previous analyses to justify the presence of short waves and fronts with different celerities is therefore not due to the model that was used, but rather to the mathematical analysis tools used to analyze it. By using a nonmodal approach, we have demonstrated that a non-negligible nonnormality of the eigenvector set is ubiquitous in the parameter space and, consequently, remarkable transient growths

103

of asymptotically stable modes are possible in the first stages of bar dynamics.

Secondly, in order to understand the core mechanisms that occur in the first stages of bar formation and to collect a sufficient amount of data for a quantitative explanation of the phenomena, we have performed a detailed experimental analysis of the pattern inception phase through a number of flume experiments. The main results of the experimental observations are: (i) the early stage bar patterns show a significantly lower average wavelength than the one that dominates asymptotically; (ii) asymptotically stable wavelengths (according to the classic linear stability theory of bars) emerge ; (iii) an amalgamation process occurs, due to different front celerities, thus inducing a strong increment in the average wavelength of bars in the pattern.

Considering the experimental evidences and the theoretical conjectures, we have drawn the following picture of the wavelength selection process that occurs during bar instability inception. The transient amplification of perturbations with a short-wavelength is much larger at the initial time than the amplification of the most asymptotically unstable wave. As time increases, the amplifications of the short waves and that of the asymptotically unstable waves first become comparable; as a result two distinct families of waves coexist at the same time in the channel. This justifies the presence of fronts with different celerities. As time passes, the most asymptotically unstable modes tend to dominate, as transient growths fade away. This picture allows one to obtain an explanation of the phenomena observed during the wavelength selection based only on linear processes. Nonlinearities certainly play a role (e.g., in the saturation of the exponential growth or in the wavelength evolution timescales), but the main reason for the wavelength evolution should be attributed to linear wave interactions.

Chapter 3

A shallow-water theory of river bed forms in supercritical conditions

A supercritical free-surface turbulent stream flowing over an erodible bottom can generate a characteristic pattern of upstream migrating bed forms known as antidunes. This morphological instability, which is quite common in fluvial environments, has attracted speculative and applicative interests, and has always been modeled in 2D or 3D mathematical frameworks. However, in this chapter we demonstrate that antidune instability can be described by means of a suitable one-dimensional model that couples the Dressler equations to a mechanistic model of the sediment particle deposition/entrainment. The results of the linear stability analysis match the experimental data very well, both for the instability region and the dominant wavelength. The analytical tractability of the 1D modeling allows us (i) to elucidate the key physical processes which drive antidune instability, (ii) to show the secondary role played by sediment inertia, (iii) to obtain the dispersion relation in explicit form, and (iv) to demonstrate the absolute nature of antidune instability.

Figure 3.1. Antidunes on the Arveyron river, a 3% slope gravel bed river in Chamonix (France). The wavelength was approximately 2m (Recking *et al.*, 2009).

3.1 Introduction

In this chapter, focus is on the micro-scale bed forms that are generated by supercritical streams, i.e. when the Froude number is greater than one. These bed forms are traditionally called *antidunes*. They are characterized by a periodic pattern that migrates upstream and induces the free surface to be in-phase with the bottom (see figure 3.1). The interest in antidunes lies in the impact of bed forms on human activities and environment preservation. Bed forms interfere with navigation (1989Lillycrop *et al.* 1989; Gao & Roelvink, 2010) and fluvial infrastructures (Amsler *et al.*, 2003), are important paleo-climatic proxies (Shaw & Kellerhals, 1977; Rust & Gostin, 1981; Fielding, 2006) and they also affect a number of key bio-geochemical processes that occur in river corridors (Jones & Mulholland, 2000; Corenblit *et al.*, 2011; Bardini *et al.*, 2012).

In the past, the fluid dynamics of a stream over antidunes were modeled using either irrotational or rotational 2D models. Basically, irrotational models assume that the evolution of an erodible bed depends on the flow velocity at the bottom and on an *ad hoc* phase-lag between the flow field and bed topography (Kennedy, 1963; Reynolds, 1965; Hayashi, 1970), the latter being introduced in order to take into account those processes that are not described by the potential flow (e.g., flow separation). However, the evaluation of the right phase-lag continued to remain an open question

until potential models were completely abandoned after the artificiality of the introduction of the phase lag was demonstrated by Coleman (Coleman & Fenton, 2000). Rotational models allowed important improvements in the antidune modeling. The first attempts adopted the vorticity equation with a constant eddy viscosity (Engelund, 1970; Fredsøe, 1974). However, a suspended load was necessary for the antidunes to occur, although several experiments demonstrated that a bedload alone is actually sufficient. Colombini (2004) has recently proposed a more refined antidune model that couples a mixing length approach with the classical Meyer-Peter-Müeller (MPM) formulation of the bedload. The key point of this model is that it evaluates the shear stress that is responsible for the sediment transport at the top of the bed-load saltation layer. This leads to the correct prediction of antidunes considering the only bed-load. More recently Camporeale & Ridolfi (2011) have performed a nonmodal analysis of such model, demonstrating that transient growth of stable modes are actually responsible of wavelength selection processes.

Summing up, antidunes have always been investigated in a two-dimensional mathematical framework, while the linear stability of the fully 3D problem has only recently been proposed (Colombini & Stocchino, 2012). Therefore, it is commonly assumed that the simplest hydrodynamic model that is able to predict antidunes has to be at least two-dimensional. Such a conjecture is motivated by evidence that bed form amplitude usually scales with the stream depth and, therefore, the vertical velocity and the non-hydrostatic component of pressure are assumed non negligible. The main aim of this chapter is to show that antidune instability can instead be correctly described by means of an appropriate one-dimensional depth-averaged model.

In this chapter, we propose a novel theory for antidunes, which is obtained by coupling 1D shallow-water equations with a mechanistic sediment transport formulation. We demonstrate that despite some simplifications in the modeling, the physical mechanisms required for the inception of the instability and for the correct selection of the dominant wavelength are preserved. Furthermore, the formulation of an analytically tractable theory allows us to obtain the dispersion relation in an explicit way. This important finding

107

opens the way to further theoretical analyses on antidunes, concerning, for example, non-parallelism effects (Schmid & Henningson, 2001) or the absolute/convective nature of instability (Huerre & Rossi, 2000). Such analyses in fact require sophisticated techniques that are precluded due to the mathematical complexity of the two-dimensional approaches used so far. In this thesis, in particular, we will demonstrate the absolute nature of antidune instability.

By now, no depth-averaged flow model, coupled with any bottom evolution, has been able to detect antidune instability (Gradowczyk, 1970). DiCristo *et al.* (2006) have recently proposed a morphodynamical model that couples the de Saint-Venant (dSV) shallow water equations with a modified MPM formula, and which takes into account sediment particle inertia. The bottom was found to be unstable in the supercritical regime, but the theory failed to correctly evaluate the marginal stability curves, thus any comparison with real data from measurements was hampered. Our model instead shows that two factors play a crucial role in the 1D modeling of antidune instability. The first factor concerns the non-hydrostatic component of the pressure distribution induced by bed curvature and its effect on the shear tresses. In order to describe this aspect, we adopt the flow modeling given by (Dressler, 1978). The second key point concerns sediment transport. In previous works, it was always modeled with empirical formulas derived from experiments in uniform equilibrium conditions (e.g., the MPM formula), that is, it is assumed that the particle deposition equals the entrainment at any point of the bed. However, this is an approximation in unstable conditions, the stream-bed system being far from the local equilibrium. For this reason, we do not assume any equilibrium conditions and instead adopt a mechanistic approach that is based on the the momentum exchange between the fluid and the sediment and on the (space- and time-dependent) balance of the forces acting on the sediment particles (Seminara *et al.*, 2002; Parker *et al.*, 2003). Such an approach allows the sediment transport rate to be modeled in terms of particle velocity and areal concentration of the moving particles, and the bed evolution results from the competition between the local entrainment and deposition processes. This chapter is organized as follows: in section 3.2 we introduce the hydrodynamic and sediment transport models

adopted; in section 3.3 we perform the linear stability analysis of the developed model; in section 3.4 we illustrate the physical mechanisms involved in the antidune formation; in 3.5 we expand our model in order to study the free surface stability, too. In section 3.6 we demonstrate the absolute nature of antidunes instability; finally in 3.5 we draw some quick conclusions.

3.2 Modeling aspects
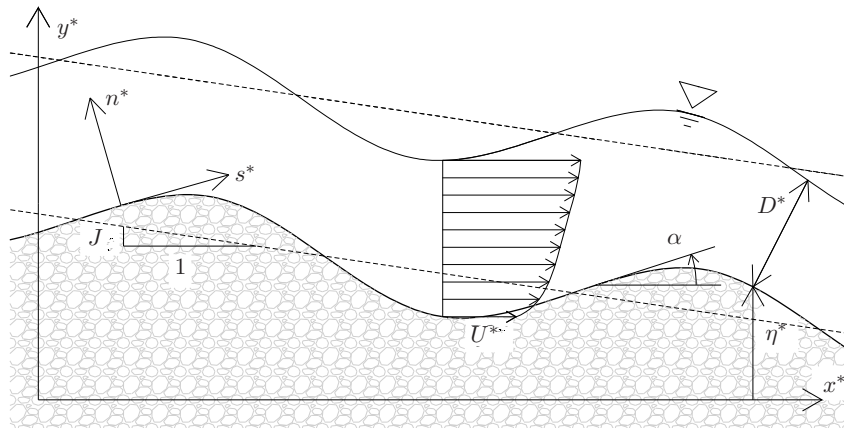
Figure 3.2. Scheme of a channel with antidunes, in which the absolute (x^*, y^*) and local (s^*, n^*) reference systems are reported. The continuous and dotted lines represent the flow condition with antidunes and the unperturbed condition, respectively.

Let us consider a turbulent open-channel flow over an undulated bed (see figure 3.2) in which $\{x^*, y^*\}$ and $\{s^*, n^*\}$ are the (global) Cartesian and the (local) boundary-fitted reference systems, respectively. Henceforth, the asterisk refers to dimensional quantities. The bottom is defined by the equation $y^* - \eta^*(x) = 0$, where the function $\eta^*(x)$ is assumed to be continuous up to its third derivative. The uniform unperturbed condition – referred to with the subscript '0' – features a flat bed inclined with a constant slope J and a depth equal to D_0^*.

109

According to Dressler (1978)[1] we introduce the channel shallowness, $\sigma=(D^*/L^*)^2$ – L^* being the longitudinal length scale of the problem – and consider the mass and momentum conservation equations for a two-dimensional irrotational flow written in curvilinear coordinates, flanked by suitable kinematic and dynamic conditions at the free surface as well as impermeability and non-slip conditions at the bottom. After expanding in term of σ – a suitable approach being $\sigma = \mathcal{O}(10^{-2})$ in the antidune problem here considered – and using D_0^* and U_0^* to make the equations dimensionless (with U_0^* the unperturbed flow velocity close to the bottom), Dressler obtained, from the kinematic condition at the order $\mathcal{O}(\sigma^0)$, the normal profile of the longitudinal velocity $\mathcal{U}(s,n,t)=U/\mathcal{C}$, where $\mathcal{C}=1-\kappa n$, κ is the local bed curvature and $U(s,t)=\mathcal{U}|_{n=0}$ is the tangential velocity at the bottom, which is still unknown. The continuity and vertical momentum equations, at $\mathcal{O}(\sigma^1)$, instead provide the vertical profiles of the dimensionless normal velocity, $\mathcal{V}(s,n,t)$, and pressure $\mathcal{P}(s,n,t)$, respectively,

$$\mathcal{V} = \frac{\log \mathcal{C}}{\kappa \mathcal{C}} \frac{\partial U}{\partial s} - \frac{\partial \kappa}{\partial s} \left[\frac{n}{\kappa \mathcal{C}^2} + \frac{\log \mathcal{C}}{\kappa^2 \mathcal{C}} \right], \qquad (3.1)$$

$$\mathcal{P} = \frac{\gamma \left[D - n \right]}{F_0^2} + \frac{U^2}{2} \left[\frac{1}{\mathcal{N}^2} - \frac{1}{\mathcal{C}^2} \right], \qquad (3.2)$$

where log indicates the natural logarithm, $F_0=U_0^*/(gD_0^*)^{1/2}$ is the Froude number, g is the gravity acceleration, $\mathcal{N}=\mathcal{C}_{n=D}$, D is the dimensionless depth measured perpendicular to the channel bed, and $\gamma=\cos \alpha$, with α the local bed slope (see figure 3.2). The first term on the r.h.s of (3.2) is the hydrostatic pressure distribution while the second term is the non-hydrostatic correction induced by the channel curvature. In Dressler's derivation, a resistive term, induced by drag, τ_B, between the flow and bed roughness, is added to the $\mathcal{O}(\sigma^1)$ longitudinal momentum equation computed at $n=0$, thus a shallow water equation suitable for open channel flows in rivers is obtained

$$\frac{\partial U}{\partial t} + \frac{U}{\mathcal{N}^2} \frac{\partial U}{\partial s} + \frac{\sin \alpha}{F_0^2} + \Pi + \frac{\tau_B}{D(1 - \kappa D/2)} = 0. \qquad (3.3)$$

---

[1] For the complete derivation of Dressler's equation, see Appendix C.

The first two terms in (3.3) account for flow acceleration, the third term is due to gravity and the fourth term accounts for the pressure gradient evaluated at the bottom which, from (3.2), reads

$$\Pi = \frac{\partial \mathcal{P}}{\partial s}\bigg|_{n=0} = \left(\frac{\gamma}{F_0^2} + \frac{\kappa U^2}{\mathcal{N}^3} \right) \frac{\partial D}{\partial s} - \left(\frac{\kappa \sin \alpha}{F_0^2} - \frac{U^2}{\mathcal{N}^3} \frac{\partial \kappa}{\partial s} \right) D. \quad (3.4)$$

The last term in equation (3.3), taking into account the drag on the bed, contains a curvature-dependent correction (Dressler & Yevjevich, 1978). The Chezy formula $\tau_B = CU^2$ can be assumed, where C is the friction coefficient that is achievable from Einstein (1950) relation as a function of a relative roughness, $d_s = d_s^*/D_0^*$ being d_s^* the mean grain diameter (usually in the range $[10^{-2} - 10^{-4}]$). Finally, the first-order approximation of the kinematic condition at the free surface provides the continuity equation

$$\frac{\partial D}{\partial t} + \frac{U}{\mathcal{N}^2} \frac{\partial D}{\partial s} - V = 0, \quad (3.5)$$

where $V = \mathcal{V}|_{n=D}$. It should be recalled that, for $\kappa \to 0$, equations (3.3,3.5) reduce to the standard dSV equations, with a flat distribution of the longitudinal velocity, zero normal velocity, and a hydrostatic pressure distribution.

With the aim of proposing a 1D theory for bed forms, the above shallow water hydrodynamic formulation has to be coupled to a morphodynamic model. In order to do so, we consider a mechanistic approach, which extends the formulation by Seminara *et al.* (2002) and Parker *et al.* (2003), to a non-uniform case. The key point of the mechanistic approach is

$$q = \xi v, \quad (3.6)$$

where $q = q^*/(Rgd_s^3)^{1/2}$ is the dimensionless sediment transport rate, $\xi = \xi^*/D_0^*(1-p)$ is the areal concentration of the moving particles, v is their dimensionless velocity, p is the bed porosity (set to the usual value $p = 0.4$), $R = \rho_s/\rho - 1$, and ρ_s and ρ are the sediment and fluid densities, respectively (a typical value for silicate sediments is $R = 1.65$).

We neglect the suspended and wash load, so that the overall sediment transport is concentrated in the so-called 'bedload layer' ($0 < n < h_s$, see figure 3.3a), in form of rolling, sliding and salting.

The bedload layer thickness h_s is assumed equal to $2.5d_s$ (Seminara *et al.*, 2002). The hypothesis of considering bedload only allows us to focus our analysis on antidunes. In supercritical flow conditions two competing bed forms can arise: antidunes and cyclic steps (Kostic *et al.*, 2010). However, a recent experimental study (Yokokawa *et al.*, 2011) has indicated that antidunes develop when the sediment transport is concentrated on the bedload, differently, cyclic steps arise in the case of prevalent suspended sediment transport.

The concentration and velocity of the moving particles are determined by considering a balance between the forces acting on the sediment particle, the exchange of momentum between the fluid and the particles in the bedload layer, and erosion/deposition processes.

Let us specify the shear stresses involved in the bed load layer. Referring to figure 3.3*b*, τ_I^* is defined as the shear stress exerted by the fluid at the interface with the bedload. If the drag force insufficient to overcome the resistance forces acting on the particles, the total shear stress exerted on the bottom of the bed load layer is split into two components: the (dimensionless) stress exerted by the sediments, τ_s, and the stress exerted by the fluid, τ_f, so that $\tau_I = \tau_s + \tau_f \sim \tau_B$, provided $h_s \ll D$. By imposing a quadratic dependence between τ_s and the relative velocity of the particle with respect to the fluid, and imposing a standard velocity distribution near the bottom, it is straightforward to obtain the relationship

$$\theta_f = \theta_B - T_\mu \xi \left(\frac{f}{F_0} \sqrt{R d_s \theta_B} - v \right)^2 , \qquad (3.7)$$

where $\theta = F_0^2 \tau / R d_s$ is the Shields stress and $f = 11.5$. The coefficient T_μ is reported in Appendix D.1 together with the coefficients R_μ and S_μ that are introduced later on.

According to the standard literature, we can assume that the erosion rate, $\mathcal{E}$, of the particles from the bottom ($n=0$) is proportional to the fluid shear stress in excess of a threshold quantity θ_c of incipient mobilization. The deposition rate of the particles on the bottom, $\mathcal{D}$, can instead be assumed to be proportional to the shear stress exerted by the solid, τ_s (thus decreasing with the increase in τ_f) and the particle concentration. Both the erosion and the deposition are instead inversely proportional to the grain diameter. On

(a)

bulk of the stream

n^*

Flow

h_s^*

τ_I^*

bedload layer

τ_B^*

(b)

n^*

τ_I^*

τ_I^*

h_s^*

τ_s^*

τ_f^*

τ_B^*
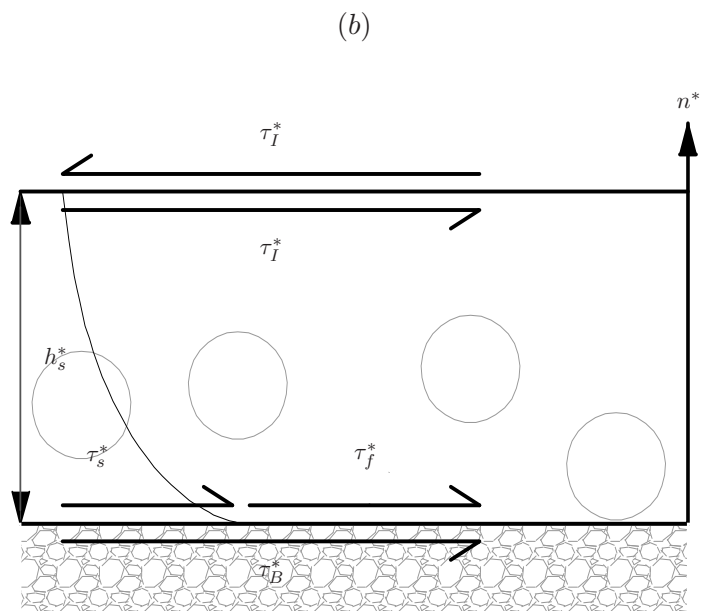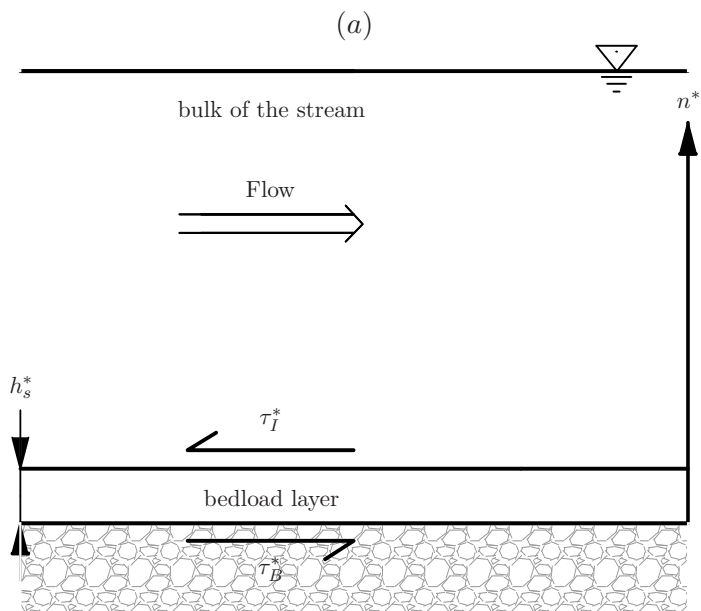
(c)
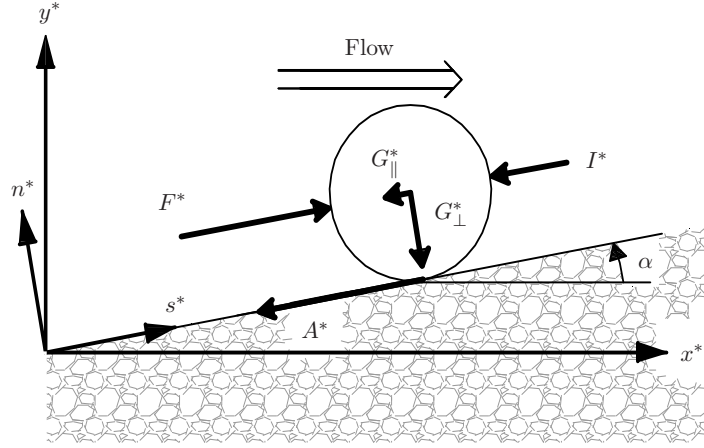
Figure 3.3.   In panel (a), the conceptual subdivision of the system in bulk of the stream and bedload layer. In panel (b), the subdivision of shear stresses at the bottom: as a result of momentum transfer from fluid to sediment by drag, τ_I^* splits between a component exerted by the fluid, τ_f^*, and a component exerted by the solid particles, τ_s^*; for equilibrium, $\tau_B^* = \tau_f^* + \tau_s^*$. In panel (c), the forces acting on a single particle moving on the bed load layer are shown: the drag force due to fluid motion F^*, the dynamic friction A^*, the inertia I^*, and the component of the particle weight parallel to the slope $G_\parallel^*$. In panel (c) are visible the Cartesian (x, y) and the curvilinear (s, n)reference systems.

the basis of experimental and dimensional considerations, Parker *et al.* (2003) assumes the following relationships

$$\mathcal{E} = \frac{r_e A_e}{d_s} \left(\theta_f - \theta_c\right)^{3/2}, \quad \mathcal{D} = (1 - p)\frac{r_s A_s}{d_s^2}\theta_s^{1/2}\xi, \qquad (3.8a, b)$$

where A_e=0.028, A_s=0.068, and r_e and r_s are reported in Appendix D.1. If the erosion and deposition rates do not balance (i.e., non-uniform conditions), the mutual dependence between the spatial

change in sediment transport and the temporal change in the bottom elevation can be described – after using(3.6) – by means of the following equations

$$\frac{\partial(v\xi)}{\partial x} = \Theta(\mathcal{E} - \mathcal{D}), \qquad \frac{\partial \eta}{\partial t} + \frac{\partial(v\xi)}{\partial x} = 0, \qquad (3.9a, b)$$

where $\Theta = (Rd_s^3)^{1/2}/(1-p)$ and $F_0 = \mathcal{O}(10^{-3} - 10^{-4})$. Equation (3.9$a$) imposes the sediment balance in the bedload layer, while (3.9b) is the kinematic condition for the bottom boundary, namely the well-known Exner equation.

Finally, we need a further equation for v, which is provided by imposing the dynamical equilibrium of the forces acting on the sediment grain (see figure 3.3c)

$$I^* = F^* - A^* - G_\parallel^*, \qquad (3.10)$$

where F^* is the drag force (proportional to $[f\sqrt{\theta_B} - v]^2$, as in (3.7)), $A^* = \mu_d G_\perp^*$ is the resistive force due to friction (μ_d is the dynamical friction coefficient, see Appendix D.1), $\{G_\perp^*, G_\parallel^*\} = G^*\{\cos\alpha, \sin\alpha\}$ are the normal- and parallel- to the bottom components of the submerged weight of the particles, respectively, and I^* is the particle inertia. In dimensionless form, relation (3.10) reads

$$\frac{\partial v}{\partial t} + v\frac{\partial v}{\partial x} + R_\mu - S_\mu \left(\frac{f}{F_0}\sqrt{Rd_s\theta_B} - v\right)^2 = 0. \qquad (3.11)$$

It should be noticed that the first two terms in (3.11), which account for the inertial effects that arise in non-uniform conditions, have remained almost unexplored so far.

Summing up, the complete hydro-morphodynamic model is composed of five PDE equations (3.3, 3.5, 3.9a, 3.9b, 3.11), flanked by three phenomenological relationships (3.7, 3.8a, 3.8b) for five unknowns: U, D, η, q, and ξ.

3.3 Stability analysis and experimental validation

Let us force the flat bed solution of the uniform flow condition, $\eta_0 = -Jx$, with a normal mode perturbation, $\eta_1 = \epsilon \exp(ikx + \Omega t)$

(a)

F_0

k

(b)

F_0

k
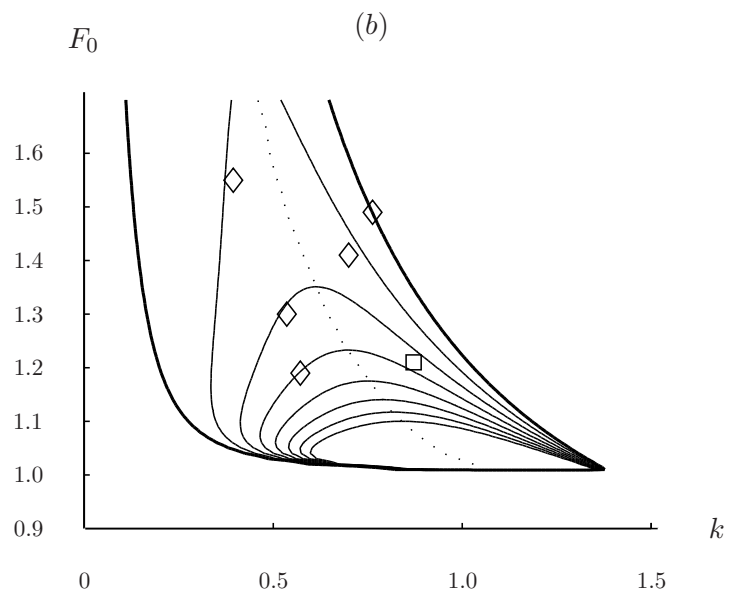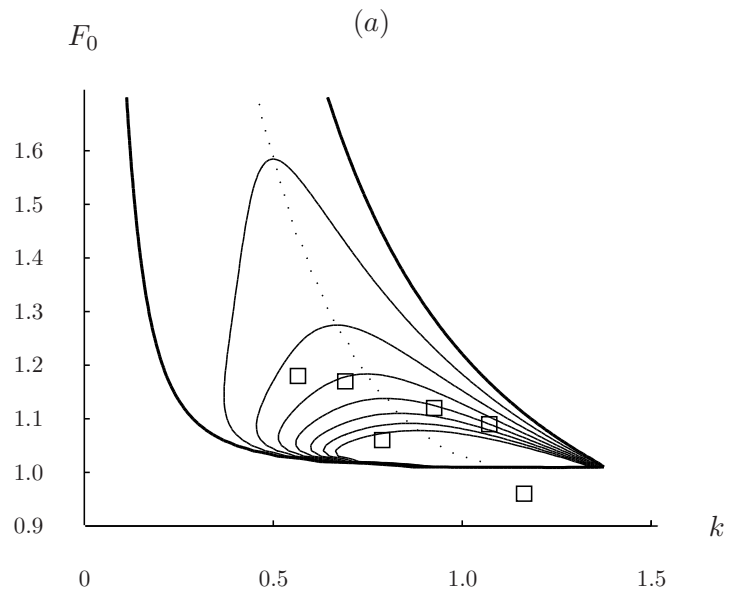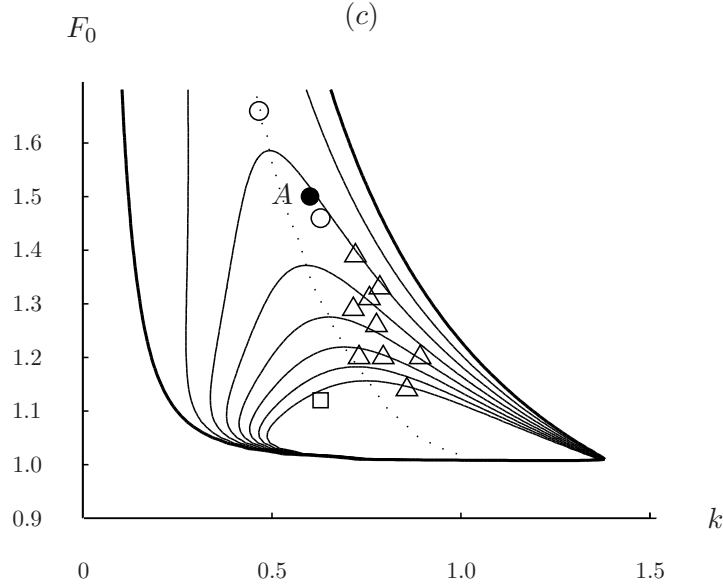
Figure 3.4.   Comparison of experimental data and theoretical previsions.   The marginal stability condition ($\Omega_r = 0$) is delimited by the thick continuous line. The thin continuous lines define iso-growrate points.   The values of grow rate are, from outer to inner, $(5,10,15,20,25,30,35) \cdot 10^{-4}$. The dotted line indicates, for each value of F_0, the most unstable wavelength. The control parameter d_s is $(1.5, 2.0, 3.5) \cdot 10^{-3}$ in panels from (a) to (c) , respectively. In the instability zone the condition $\Omega_i > 0$ is always satisfied. Physically, it indicates that the perturbation propagates upstream. Markers indicates experimental data (Guy *et al.*, 1966), in particular □ run set I64, ◯ run set I66, △ run set I72, △ run set I74.

(plus complex conjugate), where k and $\Omega=\Omega_r+i\Omega_i$ are the longitudinal wave number and the complex frequency of the perturbation, respectively, and $\epsilon \ll 1$ is the amplitude of the bed perturbation. Accordingly, the four variables of the morphodynamic model $\mathbf{X}=\{U, D, v, \xi\}$ respond with the following ansatz

$$\mathbf{X} = \{1,1, v_0, \xi_0\} + \epsilon \mathbf{X}_1 e^{(ikx+\Omega t)} \quad + \text{c.c}, \qquad (3.12)$$

117

where $\mathbf{X}_1 = \{u_1, d_1, v_1, \xi_1\}$. As known, $\Omega_r > 0$ ($\Omega_r < 0$) refers to the unstable (stable) conditions, whereas $c = -\Omega_i/k$ is the phase celerity of perturbations. As we are interested in studying the long-term response of the system, and the bed timescales are usually longer than the hydrodynamics timescales, we follow the quasi-steady approximation (Federici & Seminara, 2003; Colombini, 2004) and neglect the time derivatives in all the equations except in the Exner equation. The validity of this assumption will be discussed in the section 3.5, where we will investigate the effect of the neglected time derivatives on the morphological and free surface instability (i.e., roll waves). After introducing (3.12) into the above problem, recalling that $\partial/\partial s = \gamma \partial/\partial x$ and linearizing with respect to ϵ, at the leading order we obtain

$$v_0 = \frac{f\sqrt{J}}{F_0 \mathcal{J}} - \sqrt{\frac{R_0}{S_0} \frac{\mu - J}{\mu \mathcal{J}}}, \qquad (3.13)$$

$$\xi_0 = \frac{1}{\rho_0}\left(\frac{J}{Rd_s \mathcal{J}} - \frac{\mu - J}{\mu \mathcal{J}}\theta_{ch}\right), \qquad (3.14)$$

where θ_{ch} is the critical value for horizontal beds and $\mathcal{J} = \sqrt{1 + J^2}$, R_0, S_0, together with the coefficients ρ_0 toρ_{10}, and Γ_1 to Γ_6 are reported in Appendix D.1 At $\mathcal{O}(\epsilon)$, we instead obtain $\mathcal{A}\mathbf{X}_1 = b$, where

$$\begin{aligned}
\mathcal{A}(1,2) &= ik - J + c_D F_0^2 \mathcal{J}^2, \\
\mathcal{A}(2,1) &= 1, \\
\mathcal{A}(2,2) &= 1, \\
\mathcal{A}(3,1) &= \frac{2J}{F_0^2 \mathcal{J}^2}, \\
\mathcal{A}(3,2) &= c_D, \\
\mathcal{A}(3,3) &= -\frac{2\sqrt{J}}{f F_0 \mathcal{J}} - ik\rho_2, \\
\mathcal{A}(4,1) &= \rho_4 - \frac{\sqrt{J}\rho_6(F_0\rho_7 + f\rho_8)}{F_0 \mathcal{J}}, \qquad (3.15)\\
\mathcal{A}(4,2) &= \rho_5 - \frac{c_D F_0 \mathcal{J}\rho_6(F_0\rho_7 + f\rho_8)}{2\sqrt{J}}, \\
\mathcal{A}(4,3) &= \frac{ik\xi_0}{\Theta} + \rho_6\rho_8, \\
\mathcal{A}(4,4) &= \frac{ikv_0}{\Theta} + \frac{\rho_9 + \frac{JT_0\rho_8^2}{F_0^2 \mathcal{J}^2}}{A_s\Gamma_5 - A_e\Gamma_6}, \\
\mathcal{A}(1,3) &= \mathcal{A}(1,4) = \mathcal{A}(2,3) = \mathcal{A}(2,4) = \mathcal{A}(3,4) = 0, \\
b^T &= \left(-ik\rho_1, \frac{k^2}{2\mathcal{J}^3}, -ik\rho_3, \rho_{12}\right)
\end{aligned}$$

In equation (3.15) $C_D = \partial C/\partial D|_{D=1}$ and T_0 is reported in Appendix D.1. After solving the above algebraic system, it is possible to

substitute the values of v_0, v_1, ξ_0 and ξ_1 in the Exner equation (3.9b) written at the first order

$$\Omega = -\mathrm{i}k\left(\xi_0 v_1 + \xi_1 v_0\right), \qquad (3.16)$$

from which one finally obtains the dispersion relation.

The above problem is basically governed by four dimensionless parameters: k, F_0, J and d_s. By manipulating Einstein's and Chezy's equations at theleading order, the following relationship holds between the Froude number, the slope and the relative roughness

$$F_0\sqrt{\frac{1+J^2}{J}} + 2.5\log\left(2.5d_s\right) - 6 = 0. \qquad (3.17)$$

Without any loss of generality, we are free to choose three independent parameters: k, F_0 and d_s. By choosing F_0 in the range [1,3] and $d_s = \mathcal{O}(10^{-3})$, it follows $J = \mathcal{O}(10^{-3})$.

The contour plot of the growth factor, Ω_r, as predicted from the above theory, is reported in figure 3.4 on the (k, F_0) plane, for supercritical conditions $(F_0 > 1)$and three different values of the relative roughness, d_s (panels *a-c*). In order to validate our theory, we have also reported a set of experimental data, taken from a celebrated benchmark of laboratory analyses on dunes and antidunes (Guy *et al.*, 1966). The same dataset has also been adopted to test other analytical models (Colombini, 2004; Colombini & Stocchino, 2008). The single experimental values are superimposed onto the (k, F_0) plane with a marker, where k is the wave number of the antidune that was experimentally observed for a given value of the Froude number, F_0.

The comparison appears very satisfactory, since almost all the points from the experiments are enclosed within the marginal stability curve, defined by $\Omega_r{=}0$ (thick lines). The model is therefore able to predict the pattern formation correctly. Furthermore, most of the data are very close to the dotted line, which refers to the most unstable wave number versus F_0 and corresponds to the pattern selected when the linear theory is used. We also emphasize that the contour plots reported in figure 3.4 resemble the results obtained by means of other more sophisticated two-dimensional rotational models (Colombini, 2004; Camporeale *et al.*, 2012). Finally, it is worth noticing that the phase velocities of all the cases considered

here are negative, i.e., the perturbations propagate upstream, in agreement with consolidated evidence on rivers under supercritical conditions.

3.4 The physical mechanisms that drive the antidune instability

The response of the sediment transport rate, q_1, to the bed perturbation, η_1, is the key point that can help one to understand the physical mechanisms driving the antidune formation. We recall that $q_1 = \xi_0 v_1 + \xi_1 v_0$ and two components therefore require attention: the particle velocity, v_1, and the particle concentration, ξ_1. Figures $3.5a - b$ show the spatial structure of the v_1, ξ_1 and q_1 responses to an arbitrary bed perturbation. We refer to the $(k, F_0, d_s) = (0.6, 1.5, 3.5 \cdot 10^{-3})$ case marked by the point A in figure $3.4c$, but similar results can be obtained with other values in the instability region. The $k\phi_{q_1}$ phase between the sediment transport rate and bed elevation is also highlighted in figure $3.5b$. The ϕ_{q_1} angle in fact plays a key role in the development of the bed forms, as it determines whether an infinitesimal perturbation of the bottom grows or decays (Hanratty, 1981). In particular, the $0 < \phi_{q_1} < \pi/2$ ($\pi/2 < \phi_{q_1} < \pi$) range identifies migrating bed forms growing downstream (upstream), while $\pi < \phi_{q_1} < 3\pi/2$ ($3\pi/2 < \phi_{q_1} < 2\pi$) characterizes migrating bed forms decaying upstream (downstream). Figure $3.5c$ shows the phase angle of v_1, ξ_1 and q_1 as a function of the wave number.

The phase of the particle concentration ξ_1 shows that a wave number interval where $\pi/2 < \phi_{\xi_1} < \pi$ exists in the $k \in [0.1, 0.8]$ range (see the dotted lines in panels a and c), while the phase angle outside this range is greater than π. The phase of the particle velocity, ϕ_{v_1}, instead remains higher than π for all the wavenumbers (see the dot-dashed lines in panels a and c). This means that the sediment transport rate component associated to the particle concentration perturbation, namely $\xi_1 v_0$, is actually responsible for the growth of the instability, while the particle velocity perturbation v_1 does not contribute to the generation of the instability. Its role is instead different: since ϕ_{v_1} is close to π in the instability range dictated by ϕ_{ξ_1} (see panel $3.5c$), the component of q_1 due to the particle

120

(a)

(b)

(c)
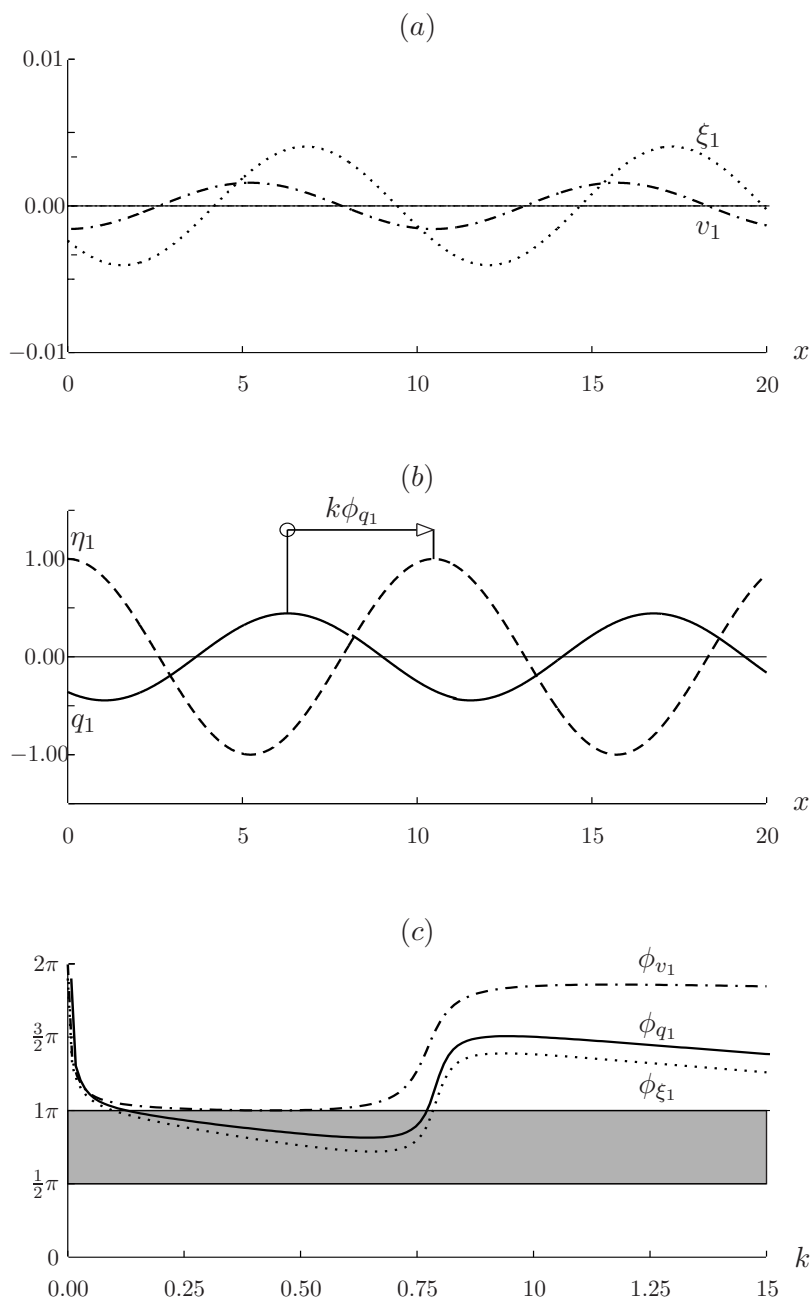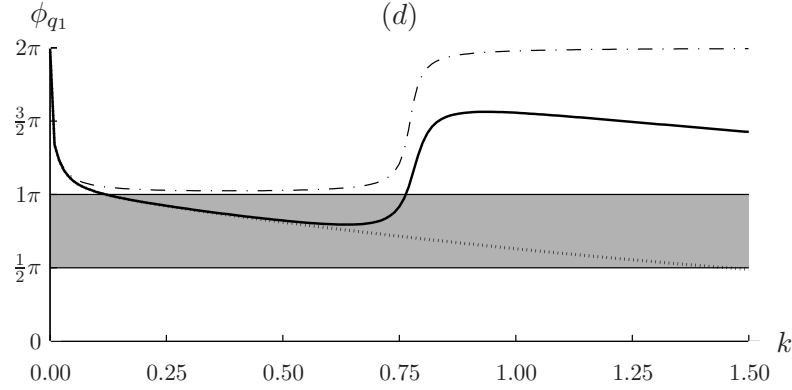
Figure 3.5. In the panels a, b, we report the perturbation amplitude of v_1 (dot-dashed in a), ξ_1 (dotted in a), q_1 (continuous in b), η_1 (dashed in b) evaluated for $d_s = 3.5 \cdot 10^{-3}$, $F_0 = 1.5$, $k = 0.6$ (point A in figure 3.4c). In panel b the phase $k\phi_{q_1}$ between sediment transport rate and bed elevation is shown. In panel (c), we report the phase angle of v_1 (dot-dashed line), ξ_1 (dotted), q_1 (continuous line) as a function of the wavenumber for $d_s = 3.5 \cdot 10^{-3}$ and $F_0 = 1.5$. The gray zone delimits the phase angles for which antidunes occur; for lower angles, downstream moving bed forms occur; for higher angles, bottom remains flat. In panel (d), plot of the phase angle of q_1 evaluated as a function of k for three different models for the same parameters used aboves. Continuous line: mechanistic sediment transport model and Dressler's equations; dotted line: mechanistic sediment transport model and dSV's equations; dot-dashed line: MPM transport model and Dressler's equations. Notice, from (3.12), that the perturbation amplitudes are all scaled by the factor $\epsilon \ll 1$.

velocity, $\xi_0 v_1$, drives the upstream migration of the bed forms. However, the remarkable similarity between ϕ_{ξ_1} and ϕ_{q_1} (compare the continuous and dotted lines in figures 3.5$a - c$) confirms that the stabilizing effect of v_1 on antidune inception is quite modest.

The mechanistic modeling of the sediment transport therefore reveals that perturbation of the particle concentration is crucial to drive antidune instability. Perturbation of the particle velocity alone is instead unable to trigger instability, but it is responsible for the main contribution to the upstream migration of the bed forms. These features explain why the simplified approaches adopted in

previous studies to model the sediment rate hamper the detection of antidune formation in a 1D framework. Such approaches (which do not consider the momentum exchange between the fluid and sediment in the bed load layer) neglect the influence of the particle concentration perturbation. In this way, the sediment transport results only related to the variable v_1. Let us consider, for instance, the complex frequency Ω that corresponds to the widely used MPM formula, which can be obtained by substituting $q = v\xi = 8(\theta - \theta_c)^{3/2}$ in (3.9b) and inserting the ansatz (3.12). After linearization, and using the sediment momentum equation at $O(\epsilon)$, we obtain an expression of Ω which is only related to the particle velocity perturbation v_1. In figure 3.5d, the phase angle of q_1 (the dot-dashed line) obtained by coupling the Dressler equations with the MPM sediment transport formula is compared with our antidune model. As expected, MPM-like models are not able to predict antidune formation (i.e., $\phi_{q_1} > \pi$ for any k) in a 1D framework and a more refined mechanistic sediment transport model is necessary.

A fundamental role in the selection of the antidune wavelength is played by the non-hydrostatic pressure component induced by the curvature of the bottom. This can be demonstrated by eliminating the addenda in equation (3.4) one by one and repeating the stability analysis. This analysis shows that the last term – which is proportional to $\partial \kappa / \partial s$ – is decisive for the wavelength selection. Confirmation of such a feature can be obtained by comparing the stability analysis results deduced using the Dressler equations and the de Saint Venant equations, which only consider the hydrostatic pressure. The differences are evident in the plane $\{k, \phi_{q_1}\}$ shown in figure 3.5d. It should in fact be noticed that the dispersion relation reads $\Omega = -\mathrm{i}kq_1$ and gives the relation between the phase angle of the sediment transport rate and the complex frequency Ω; i.e., $\phi_{q_1} = \arctan[-\Omega_r / \Omega_i]$. It follows that the wavelength selection occurs if ϕ_{q_1} exhibits a minimum for a given wave number (since Ω_i is almost independent from k). Figure 3.5d shows that wavelength instability is correctly selected by means of the Dressler model, while the de Saint Venant one predicts the instability (albeit this is due to the mechanistic sediment transport model), but fails to select a wavelength as the corresponding ϕ_{q_1} does not exhibit any minimum.

In short, the bed curvature-induced non-hydrostatic pressure

123

component is fundamental to describe the wavelength selection mechanism, while the growth of bed forms and their upstream migration need a sediment transport model that is able to describe non equilibrium conditions.

At this point, it is instructive to evaluate the role of the different forces acting on the single sediment particles (drag, dynamic friction, gravity and inertia) in determining antidune instability. To this aim, the forces in the equilibrium equation (3.10) are removed one by one and the corresponding growth rates, celerities and marginal stability curves are compared. Four different cases are considered (see table 3.1): case GI (where G stands for gravity and I for inertia) is the complete model, case I (only inertia) does not consider gravity in the particle dynamics, case G (only gravity) neglects particle inertia, and case B (base) only retains the drag force and the dynamical friction.

Table 3.1. Cases with different force balances on the sediment particles. The wavenumbers that delimit the instability zone, k_l and k_h, and the most unstable wavenumber, $k_{\max}$, are reported for each case. $(F_0, d_s) = (1.5, 3.5 \cdot 10^{-3})$, while the complex frequency, Ω, is evaluated for $k = 0.6$. The plot corresponding to the considered case is recalled in the last column.

	Forces	k_l	k_h	$k_{\max}$	$\Omega \cdot 10^{-3}$	Fig.
GI	$F^*, A^*, G_\parallel^*, I^*$	0.121	0.763	0.528	$1.05 + 1.43i$	$3c$
G	$F^*, A^*, G_\parallel^*$	0.186	0.717	0.514	$1.13 + 1.25i$	$5a$
I	F^*, A^*, I^*	0.120	0.770	0.532	$0.34 + 1.64i$	$5b$
B	F^*, A^*	0.175	0.763	0.542	$0.50 + 1.58i$	$5c$

Figure 3.6 shows the growth rate, Ω_r, of the perturbation as a function of k and F_0 for the I, G, and B cases, while case GI has already been reported in figure 3.4c. In order to make the comparison clearer, the wave numbers, k_l and k_h, which delimit the instability interval and the most unstable wave number, $k_{\max}$, are reported in table 3.1 for the representative case of F_0=1.5. The complex frequency Ω corresponding to a typical wave number is also given.

The main result that emerges in figure 3.6 and table 3.1 is that the marginal stability curves and the most unstable wave numbers

(a)

(b)
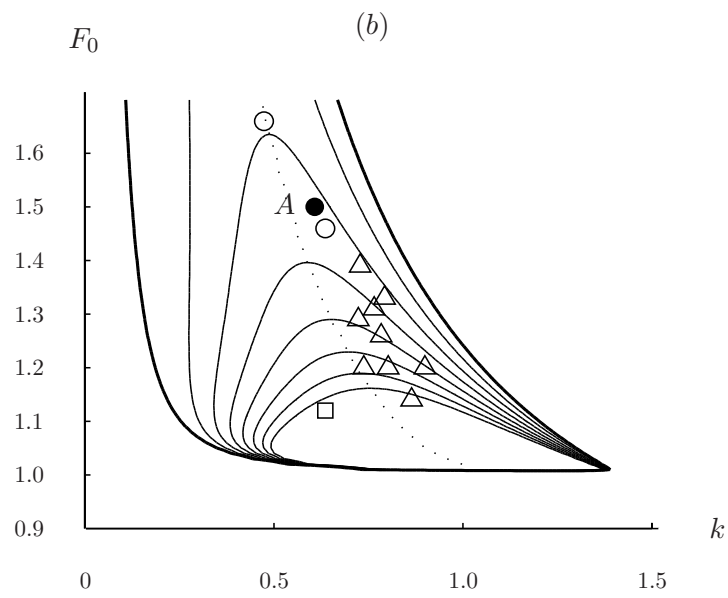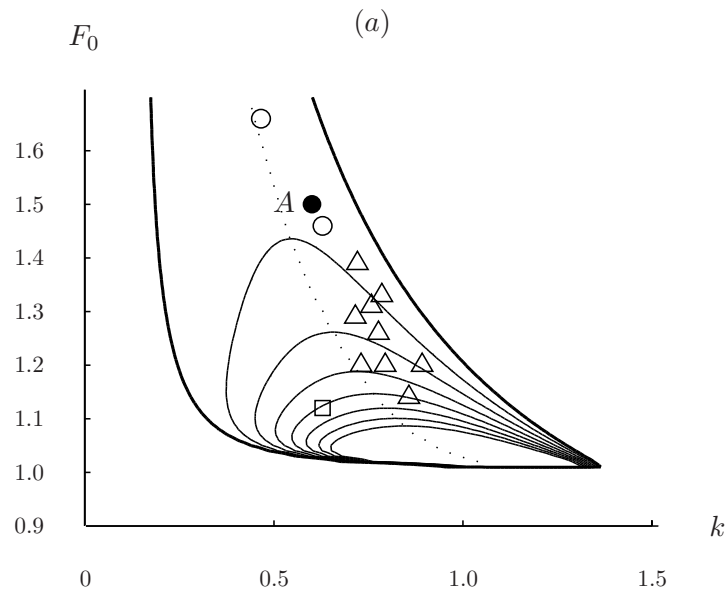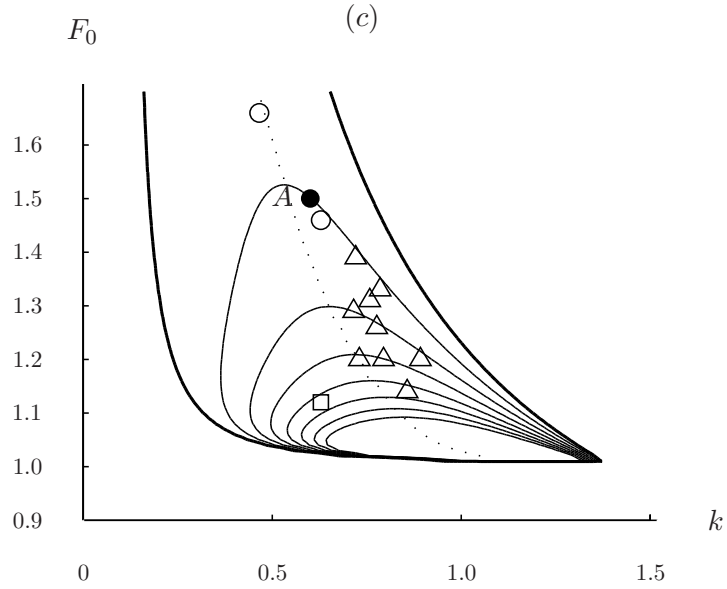
Figure 3.6. The growth rate is plotted as a function of k and F_0 (d_s=$3.5 \cdot 10^{-3}$) for cases G (a), I (b), and B (c) (see table 3.1). The symbols and lines correspond to those reported in figure 3.4.

do not change significantly if different forces are considered in the dynamic equilibrium of the particle. This general picture therefore suggests that particle inertia and gravity play secondary roles in antidune instability compared to the stream-induced forces. However, a more detailed analysis shows some interesting differences. A comparison between cases G and B reveals that gravity reduces the growth rate. This confirms the results obtained in other works (Colombini, 2004) and it is trivial as gravity opposes (favours) uphill (downhill) motion. Upstream sedimentation and downstream erosion processes are accelerated for the same reason and upstream migration celerity is therefore increased.

Particle inertia instead increases the growth rate (see figures $3.6b - c$ and table 3.1). The reason for this behaviour becomes clear if one notices that the particle velocity and bed elevation in figures $3.5a - b$ are out of phase and, therefore, the velocity reduces (increases) upstream (downstream) from a bed crest. It

follows that inertia works in the opposite direction to gravity and the growth rate of the instability is increased, while the antidune migration celerity is reduced. Unlike from some previous works (Parker, 1975b; DiCristo *et al.*, 2006) in which the sediment mass was assumed to be a fundamental ingredient for the inception of antidunes, particle inertia is not crucial in our model for the occurrence of instability and it only gives a (non fundamental) destabilizing contribution.

Finally, a comparison of cases B and GI (see figures 3.4*c* and 3.6*c*) highlights that the combined role of gravity and inertia entails an increase in the instability growth rate. This feature can be confirmed from the example reported in table 3.1, where Ω_r increases from 0.504 to 1.055, while a small reduction of Ω_i occurs. Therefore, the de-stabilizing effect due to particle inertia prevails over the stabilizing action caused by gravity. Accordingly, a reduction in the wave celerity with respect to base case B takes place.

3.5 Free surface instability

The behavior of our model is investigated in this section, removing the quasi steady assumption introduced in section 3. This allows us to confirm its validity for morphodynamic purposes and, at the same time, to study the possible occurrence of free surface instabilities, namely roll waves. To this aim, all the time derivatives in (3.3,3.5,3.9b,3.11) are retained and a further viscous dissipative term is introduced into the fluid phase momentum equation. Previous works (Needham & Merkin, 1984; Hwang & Chang, 1987; Balmforth & Mandre, 2004; Balmforth & Vakil1, 2012) that investigated free surface stability by means of a shallow water approach, have demonstrated that this dissipative term is in fact fundamental for the description of roll waves. Its role is to suppress free surface instabilities with high wavenumbers, thus confining the free surface instability to a finite region in the wavenumber space. From a physical point of view, this additional term represents the effect of the energy dissipation by shearing normal to the flow (Needham & Merkin, 1984). The most frequently used and physically based expression of this term, which has to be added to (3.3), was proposed

by Balmforth & Mandre (2004) and reads

$$\frac{1}{DRe_e}\frac{\partial}{\partial s}\left(D\frac{\partial U}{\partial s}\right),\qquad(3.18)$$

where $Re_e = U_0^* D_0^*/\nu_e$ and ν_e represents a suitable eddy viscosity.

If the new system of equations is linearized and the anstaz (3.12) is introduced, an algebraic system similar to (3.15) is obtained. By imposing the existence of a non-trivial solution (i.e., $\det\mathcal{A} = 0$) and solving this equation in Ω, the four growth rates associated with the corresponding four solutions can be easily obtained.

We evaluated the stability of the system in the space (k, F_0) for the same parameters used in figure 3.4c and found that two modes were always stable, while two modes were unstable over a significant portion of the (k, F_0) space. The corresponding instability zones are reported in figure 3.7, where the gray zone marks the instability zone associated with the free surface perturbation, while the white zone which includes the point A marks the instability zone associated with the bed perturbation.

Comparing 3.4c and 3.7a, it can be observed that the morphological instability is practically not affected by the introduction of the additional time derivatives and of the viscous dissipative term. Neither the marginal stability curve nor the locus of $\max(\Omega_r)$ undergo appreciable changes. By computing the complex frequency associated with the morphodynamic mode for $(k, F_0) = (0.6,1.5)$ (point A in figures 3.4c and 3.7a) we obtain $\Omega = (9.02,15.20)\cdot 10^{-4}$. This growth rate is slightly lower than the corresponding quasi steady case GI reported in table 3.1. This behavior is due to the dissipation term, which reduces the capacity of the flow to transport sediments.

The inclusion of all the time derivatives and the viscous dissipative term allows the presence of roll waves to be detected (figure 3.7a). The marginal stability curve, the locus of $\max(\Omega_r)$ and the perturbation celerity are comparable with the outcomes of other models (Balmforth & Vakil1, 2012; Colombini & Stocchino, 2005) and are coherent with experimental data (Brock, 1969). The feature of increasing celerity with decreasing Froude number (see figure 3.7b), observed adopting more refined models (Colombini & Stocchino, 2005) is also captured. It is also interesting to notice that the critical Froude number F_c above which the occurrence of

(a)

(b)
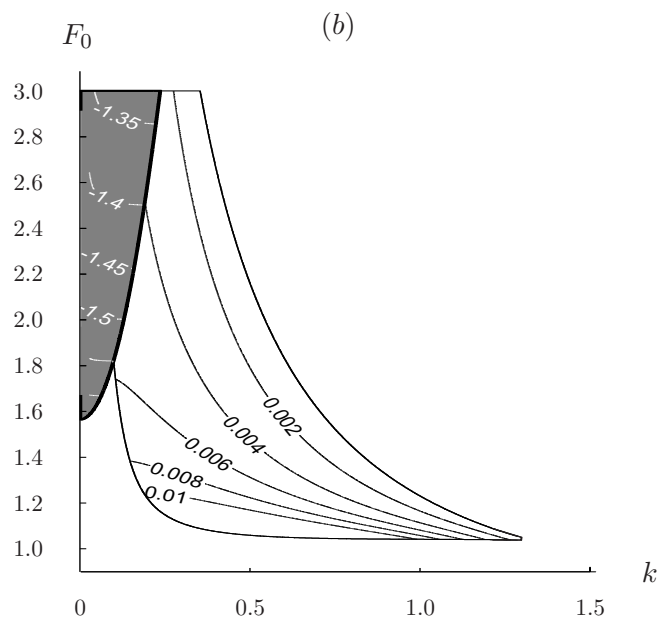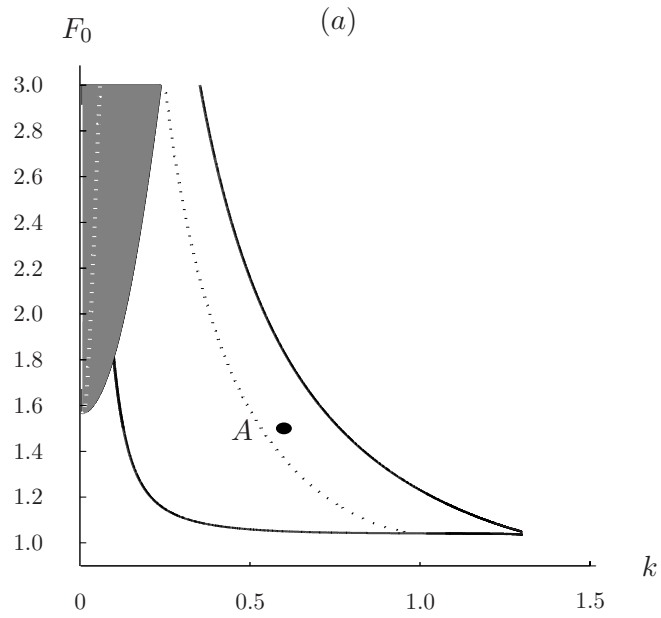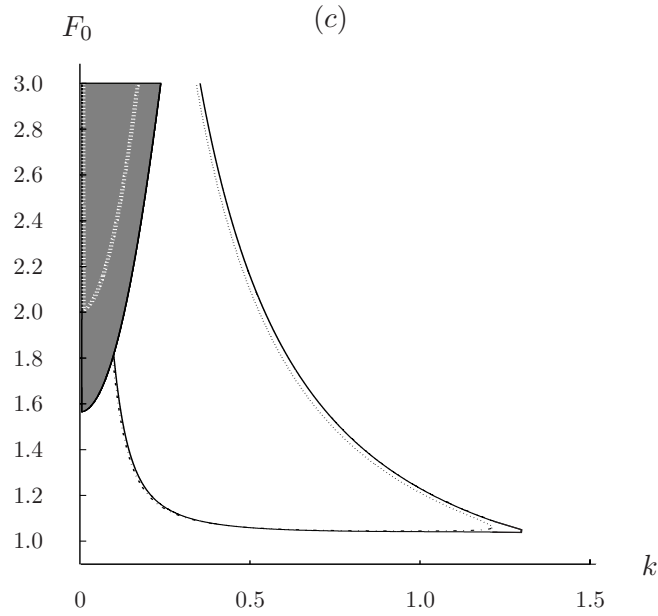
Figure 3.7. Panel (a): free surface instability zone (gray) and morphodynamic instability zone (white, indicated with point A); the dotted lines represent the locus of the most amplified wavenumbers. Panel (b): perturbation celerity (it should be recalled that a perturbation with positive celerity migrates upstream). Panel (c): comparison of the instability regions for a friction coefficient dependent (continuous line) and independent (dotted line) on the water depth. All the charts are evaluated for $d_s = 3.5 \cdot 10^{-3}$ and $Re_e = 10$.

roll waves is possible is about 1.5, apparently in contrast with the well known value $F_c = 2$. However, this behavior is typical of models in which the friction coefficient C used in Chezy's formula is assumed to depend on the water depth (Luchini & Charru, 2010; Gradowczyk, 1970). If the dependence of C on the water depth is removed – for instance by evaluating C at the uniform state – the classic result $F_c = 2$ is recovered (dotted lines in figure 3.7c). It should also be noted that the dependence or the lack of dependence of the friction coefficient on D basically has no effect on delimiting the morphological instability region.

A final comment can be made on the choice of the exact value

of Re_e adopted for the calculations. A precise estimation of the equivalent eddy viscosity is difficult, as it would require precise knowledge of the flow structure (Balmforth & Vakil1, 2012). A common approach to overcome this difficulty is to set ν_e so that the free surface instability region and the locus of the most amplified wavenumbers fit experimental data. We tried different values for the eddy viscosity, spanning several orders of magnitudes, and observed that although the marginal stability curve is quite sensitive to the actual value of ν_e (a feature that has also been observed in other works (Balmforth & Vakil1, 2012)), the locus of the most amplified wavenumbers of the roll waves was influenced much less by this choice.

3.6 The absolute nature of antidune instability

The convective or absolute nature of instability is a key property. An impulsive perturbation of the equilibrium state produces a convective instability if it migrates because of the basic motion and decays to zero along all the spatiotemporal rays x/t. On the contrary, instability is absolute if it increases unbounded throughout the domain (Bers, 1983; Huerre, 2000). Apart from speculative reasons, the nature of antidune instability is also of applicative interest. It is in fact important to evaluate whether antidunes driven by local bed perturbations (e.g., dikes, scours, etc.) only affect the downstream channel or they also spread upstream. This aspect is fundamental to correctly investigate antidune dynamics by numerical simulations and laboratory experiments.

In order to understand the nature of antidune instability, we use the criterion described by Huerre & Monkevitz (1990), who extended the concepts introduced by Briggs (1964) and Bers (1983) in plasma physics to shear flow instabilities. The response along each ray x/t can be analyzed starting from the saddle point condition

$$\frac{\partial \Omega(k)}{\partial k} = 0, \tag{3.19}$$

whose complex zero(s) $k_0 = k_{0r} + \mathrm{i}k_{0i}$ gives the absolute grow rate $\Omega_r(k_0) = \Omega_{0r}$. The theory states that the temporal grow rate along

ray $x/t=a$ is given by $\psi(a)=\Omega_{0r} - ak_{0i}$. Furthermore, if just real wave numbers are considered, equation $\partial\Omega_r/\partial k=0$ provides the wave number $k_{\max}$ which gives the maximum temporal grow rate $\Omega_{r,\max}=\Omega_r(k_{\max})$ with the corresponding group velocity

$$\beta_{\max} = \left.\frac{\partial\Omega}{\partial k}\right|_{k_{\max}}. \qquad (3.20)$$

The criterion states that instability is convective if $\Omega_r(k_{\max})>0$ and $\Omega_{0r}<0$. On the contrary, the flow is absolutely unstable if $\Omega_r(k_{\max})>0$ and $\Omega_{0r}>0$, provided the causality principle is satisfied. Recalling that a spatial branch associated with the grow rate $\tilde{\Omega}_r$ is the locus of complex wave numbers in which $\Omega_r(k_r, k_i) = \tilde{\Omega}_r$, the causality principle requires that the complex $\{k_r, k_i\}$ plane displays the pinching point k_0 between two spatial branches $k^+(\Omega_{0r})$ and $k^-(\Omega_{0r})$ of the dispersion relation, and that the spatial branches are well confined within their respective k_i half-planes when $\Omega_r \gg \Omega_{0r}$.

Introducing the previously obtained dispersion relation into condition (3.19) yields a sixth-order polynomial. In the exemplifying case $(F_0, d_s) = (1.5, 3.5 \cdot 10^{-3})$, the complex wave numbers $k_{0,j}$ ($j=1, ..., 6$) which give the vanishing group velocity and the corresponding grow rates $\Omega_{0r,j} = \Omega_r(k_{0,j})$ are reported in table 3.2 (where it can be seen that different parameter values do not change the final results of the present analysis). It can be observed that $k_{0,5}$ and $k_{0,6}$ have $\Omega_{0r,j}<0$ and would therefore lead to a convective instability, while the other four solutions have $\Omega_{0r,j}>0$: $k_{0,1}$ and $k_{0,2}$ are complex conjugate, while $k_{0,3}$ and $k_{0,4}$ are purely imaginary.

In order to asses the nature of the instability, the behaviour of the spatial branches that merge at the $j-$th branch points, in which $\Omega_{0r,j}>0$, has to be checked. At least two of the spatial branches diverging from at least one branching point must lie on distinct k_i half-plane as Ω_r attains large values (Huerre & Monkevitz, 1990) for the instability to be absolute. The behaviour of the spatial branches for the pinching points $k_{0,1}$ and $k_{0,2}$ is shown in figure 3.8a. One observes that, for increasing Ω_r (notice the trend indicated by the arrows), two of the three branches which merge at the pinching points are in the upper k_i half plane, while one is in the lower one. This indicates the absolute nature of the antidune instability.

Table 3.2. The six pinching points, $k_{0,j}$, and corresponding growth rates, $\Omega_{0,j}$, obtained by introducing the dispersion relation into condition (3.19), for the $(F_0, d_s) = (1.5, 3.5 \cdot 10^{-3})$ case.

Pinching point	$k_{0,j}$	$\Omega_{0,j} \cdot 10^{-3}$
1	$-0.464 - 0.078i$	$1.020 + 1.8364i$
2	$0.464 - 0.078i$	$1.020 + 1.8364i$
3	$2.023i$	2054.676
4	$-1.434i$	6.333
5	$0.036i$	-0.582
6	$5.890i$	-4502.531

Figures $3.8b - c$ refer to pinching points $k_{0,3}$ and $k_{0,4}$, respectively. As for increasing Ω_r, the two branches merging at the pinching points remain in the same k_i half-plane (in the upper one for $k_{0,3}$ and in the lower one for $k_{0,4}$), but the behaviour of these pinching points does not contribute to the determination of the absolute nature of antidune instability.

3.7 Conclusions

In this chapter, we have proposed a 1D model to describe the morphological instability of a granular bed bounding a turbulent supercritical open-channel flow. The very good matching between the theoretical results and the experimental data demonstrates that a suitable one-dimensional model is sufficient to catch the features of antidune instability. The key points of the model are (i) the mechanistic modelling of the sediment transport, which considers the particle concentration and particle velocity separately, and (ii) the Dressler equations, which are able to take into account the impact of the channel bottom curvature on the stream dynamics.

A careful analysis of the model components has elucidated the crucial role played by three key physical mechanisms. Firstly, the instability is driven by the phase shift between the bed perturbation and the perturbation of the sediment concentration. Secondly, the phase shift between bed perturbation and particle velocity perturbation instead controls the upstream migration of antidunes.

(a)

(b)
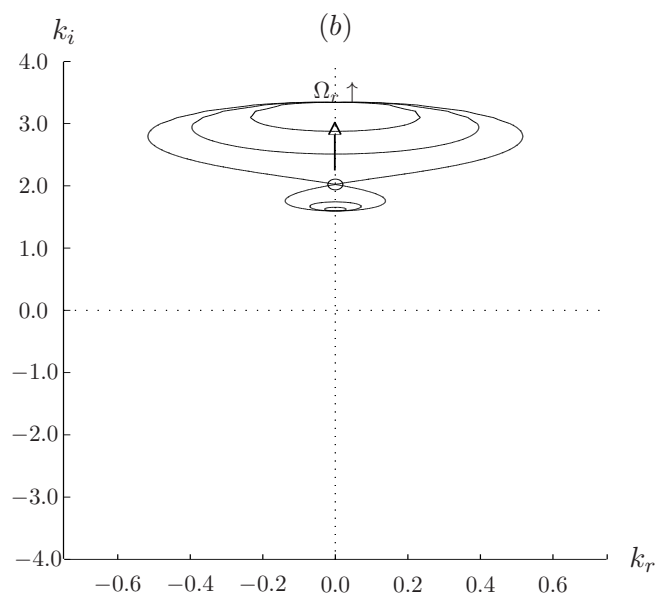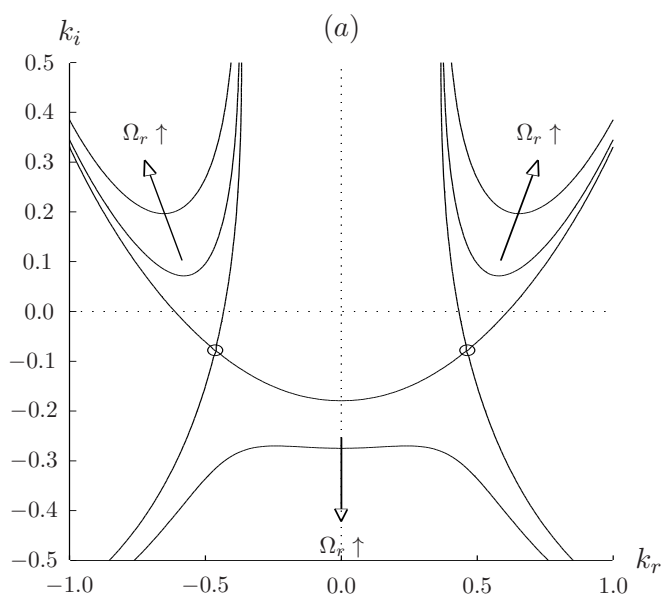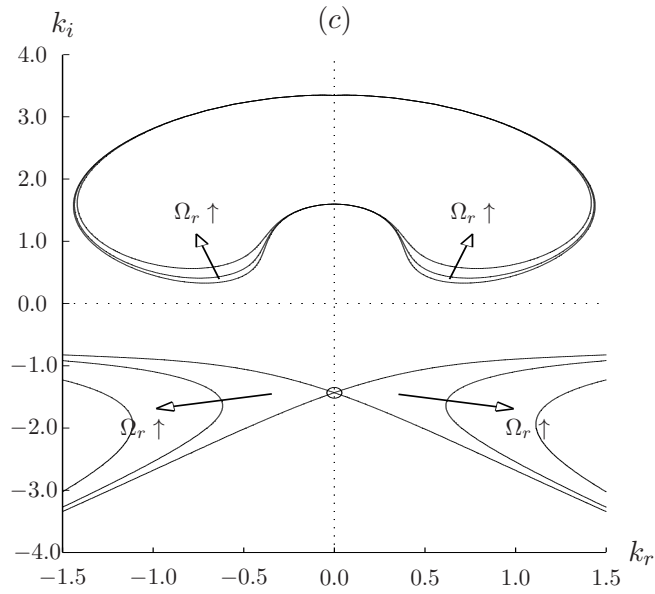
Figure 3.8. Behavior of the spatial branches at the pinching points, studied in the $k_r - k_i$ plane for $F_0 = 1.5$ and $d_s = 3.5 \cdot 10^{-3}$. In (a) we show the behavior of pinching points $k_{0,1}$ and $k_{0,2}$, in (b) of $k_{0,3}$, in (a) of $k_{0,4}$. In each panel we indicate the j-th pinching point with a circle and the corresponding spatial branch with a continuous line. The arrows indicate in which direction the spatial branches move as Ω_r attains large values. For clarifying this aspect we also report the spatial branches evaluated for $\Omega_r = 1.5\Omega_{0r,j}$ (first inner line) and for for $\Omega_r = \Omega_{0r,j}$ (second inner line).

Finally, the non-hydrostatic pressure correction induced by the channel bottom curvature is essential for wavelength selection. The importance of the first two mechanisms explains why the commonly used sediment transport formulas based on equilibrium (e.g., the Meyer-Peter-Müeller formula) are unable to describe the antidune inception in a 1D framework. In the same way, simplified 1D fluid dynamic models that assume hydrostatic pressure fail to select the right wavelength. Furthermore, we have investigated the role of gravity and inertia on sediment dynamics. As in previous studies, we have demonstrated that gravity reduces antidune instability while inertia promotes it. However, both of them play a secondary role in the occurrence of instability compared to stream-induced drag and dynamic friction. We stress that our model predicts antidune formation by taking only bedload into account (coherently with the experimental evidence).

We have obtained the dispersion relation in closed form. This result paves the way towards interesting new studies (e.g., nonmodal analysis) that would be precluded, or much more cumbersome, in 2D or 3D frameworks. An important example of such studies is given in this chapter, in which we have demonstrated the absolute nature of antidune instability, a result that can help in the interpretation of laboratory and numerical experiments on antidunes.

Appendix A

Experimental setup and equipments

This Appendix provides a description of the equipments (figure A.1) used for the realization of the experiments reported in chapter 2. The equipments are located in the Hydraulics Laboratory "G. Bidone", at the "Politecnico di Torino".

Tanks

The channel with erodible bottom, fundamental for running river morphodynamic experiments, consists of a main tank full of sand, a stilling tank and a downstream tank. In figure A.2 the general layout of the experimental apparatus is shown, and the single components can be identified.

The main tank is 4.00 m wide, 17.00 m long and 0.60 m high. The tank is made of reinforced concrete, is supported on four reinforced concrete beams 0.40 m high and with double-T cross-section.

In the longitudinal side walls of the main tank, plexiglass windows allow the evolution of the experiments to be followed, and the groundwater to be monitored. The longitudinal side walls are also surmounted by racks, on which a sand scraper moves through toothed wheels pinions.

On the bottom of the main tank there are 72 piezometers (arranged in grid of 4 longitudinal rows of 18 piezometeres). As there is a large amount of permeable sand outside the fixed walls, the
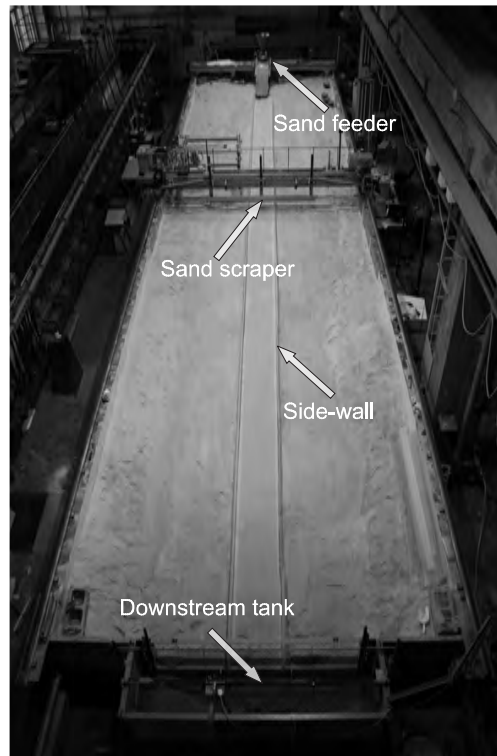
Figure A.1.   Global view of the experimental equipments.
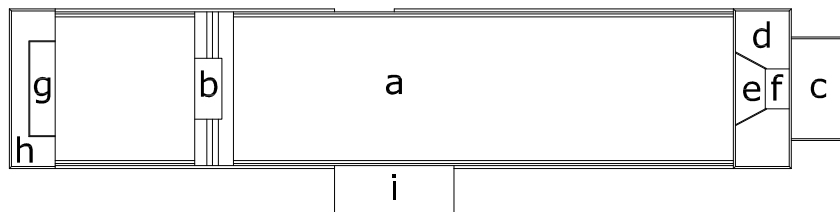
Figure A.2.   Planimetric view of the experimental setup: *a)* main tank; *b)*sand scraper; *c)* upstream tank; *d)* stilling tank; *e)* stilling tank island; *f)* sediment feeder; *g)* sediment filter tank; *h)* downstream tank; *i)* controls.

piezometers are used to saturate all the sand before the experiments, in order to avoid any water flux between the stream and the surrounding sand during the runs.

The stilling tank is 4.00 m wide, 1.40 m long and 0.60 m high,

and is used to enter the prescribed fluid rate flow in the channel. Within the stilling tank, three metal walls delimit a zone of trapezoidal shape called "the island", where the channel begins.

At the end of the main tank there is the downstream tank (4.00 m wide, 1.10 m long and 0.75 m high), used to collect the liquid discharge from the channel. Inside it, and fixed to the supporting structure of the main tank, there is a sediment filter tank. It is used to separate the sediments from the liquid discharge of the channel. It is equipped with a rectangular weir, of adjustable height, which conveys the liquid discharge in the tank downstream and regulates the water level at the end of the channel. Since the sediments carried by the stream settle in the sediment filter tank, an extraction system is used. It consists of a siphon which moves along a track fixed on the sidewalls of the sediment filter tank tank. The sediments pumped out by the siphon are discharged in a wide pipe, and transported to a square mesh sieve connected with a load cell, which quantifies the solid rate.

Mechanical equipment

Figure A.3.   Front view of the sand scraper.

On the longitudinal side walls of the main tank there are two racks along which the sand scraper moves (figure A.3). It is used for the preparation of the runs, as it shapes the sand creating a flume

with the desired characteristics (width, depth, slope). The longitudinal movement of the sand scraper along the channel is guaranteed by two electric motors that drive the rotation of the principal axle, which transmits the motion to the two toothed wheels pinions.

Figure A.4. Fixed steel blade and removable Plexiglas blade. In the picture a 50 cm wide Plexiglas blade is installed on the main blade.

In the front side of the traveling crane two blades are installed. One is made of steel, it is 2.30 wide and it is used for carrying the second blade. This second blade is made of Plexiglas, it is removable (and thus blades with different width can be placed), and it is used to shape the channel along which the experiments on alternate bars inception are performed.

The sand scraper was used to shape a straight rectangular channel with a uniform slope. Some 2 meter-long alveolar polycarbonate plates were then perpendicularly wedged into the sand, just at the carved channel boundary, in order to create fixed side-walls. To this aim, two narrow slits were cut parallel to the straight channel during the channel shaping. In this way, a fixed-wall flume was

replicated, but the channel width could easily be changed, allowing different channel geometries to be tested.

Water supply system

The upstream end of the main tank is connected to a water stilling tank which supplies the water discharge to the flume. Discharge is provided by a submerged pump, is then measured by an electromagnetic flow meter with an accuracy of ± 0.01 l s^{-1} and, finally, is regulated by a pneumatic valve.

The flow rate is regulated from the PC workstation. A *NI USB-6009* device reads the voltage signal sent from the electromagnetic flow meter by a program developed with "Lab View". In the front panel of this program (figure A.5) a digital indicator indicates the flow rate which is entering the stilling tank while with a knob the output signal (voltage from 0 to 5 V) that controls the pneumatic valve can be adjusted.

Sediments

The sand used for the experiments was chosen so that the occurrence of suspended sediment transport (Brownlie, 1981), as well as the formation of ripples and dunes is avoided (Chabert & Chauvin, 1963).

The characteristics of the sand are:

- unit weight $\rho = 2650$ kg/m^3;

- average diameter $d_{50} = 0.45$ mm;

- sorting index $I_s = 0.5(D_{84}/D_{50} + D_{50}/D_{16}) = 0.55$;

- porosity $n = 0.4$;

- hydraulic conductivity $k = 3 \cdot 10^{-4}$ m/s.

Sediment supply system

In order to ensure the dynamic equilibrium of the bottom (no aggradation nor degradation), at the beginning of the channel an equilibrium sediment rate is supplied. For this purpose, a conical hopper is used. It conveys the sediment discharge on the plate of

141

a vibrator. The vibrations of the plate convey the sediment towards a inclined ramp with rectangular outlet. The inclination of the ramp can be adjusted through threaded screws. The sand falls directly in the bottom of the channel. The regulation of the solid discharge is done in two steps: (i) by acting manually on the knob of the conical hopper in order to obtain an initial rough adjustment and; (ii) by varying the intensity of the plate vibration by means of a numerical control program developed with the software " Lab View ".

In the front panel of the program (figure A.5) a switch allows the switching on and off of the vibrator, while a knob allows the signal, (in voltage 0-5 V) that controls a digital trimmer which feeds the vibrator, to be adjusted. By adjusting the voltage of the signal, the sand discharge is regulated with an accuracy of ± 0.1 g·s $^{-1}$.

Finally, the feeding rate is calculated using the sediment transport formulas of Meyer-Peter & Muller (1948), Einstein (1950), and Ashida & Michiue (1972) as these transport formulas fit the measured bed-load very well in the adopted experimental conditions (Visconti *et al.*, 2010) .

Figure A.5. Front panel of the numerical control program devoted to control the vibrator plate and the pneumatic valve. The tool is realized with the software "Lab View".

Photographic system for the acquisition of the bed configuration

The photographic system for the acquisition of the bed configuration consists of four cameras (digital reflex *Canon EOS 400D*, equipped with auto focus, auto exposure, flash, and 10.1 megapixel image sensor with a *EF-S 18-55 MM F/3.5-5.6 II* lens) positioned along the longitudinal axis of the channel and connected on four support structures fixed, in turn, to the ceiling. The four cameras, so displaced, cover the entire experimental channel. The frames captured by any single camera are then conveniently merged together (through the software Autocad) in order to obtain the global view of the entire channel. Because of the lack of suspended sediments, the bar pattern is acquired with pixel-precision, which corresponds to 1-1.5 mm, depending on the run.

Appendix B

Complete evolution of run "a"

The material given here is the complete sequence of the run "a" of table 2.2, whose schematic evolution is given in figure 2.17, from the beginning of the run (t^*=0.0 min) to t^*=92.5 min. The pictures were recorded by two cameras fixed on the ceiling of the "G. Bidone" Hydraulics laboratory at the Politecnico di Torino five meters above the flume where the experiments were run. In order to provide a complete view of the channel, the two pictures were later merged together. The experiments were run on the 24th of may, 2011. It was impossible to print the picture as taken by the camera, for this reason, only the evolution of the front is reported in this thesis. The interested reader can contact the author for the original photographs. In order to study the temporal evolution of the front positions we also show (dashed line) the position of the front at the previous sampling time (t^*−2.5 min). Horizontal arrows link the midpoint or the lower apex of the bar front recorded at the previous sampling time with their current positions. Fronts are named with a letter A-R. We report: (i) the wavelength of the bar fronts and (ii) the celerity of the fronts at the midpoint evaluated as the displacement between the current position and the position at t^*−2.5 min divided by the time interval 2.5 min. The celerity values are reported above the corresponding horizontal arrows.

t*=0.0 min

t*=2.5 min

t*=5.0 min

t*=7.5 min

t*=10.0 min

t*=12.5 min

t*=15.0 min

t*=17.5 min

t*=20.0 min

t*=22.5 min

t^*=75.0 min

t^*=77.5 min

t^*=80.0 min

t^*=82.5 min

t^*=85.0 min

t^*=87.5 min

t^*=90.0 min

t^*=92.5 min
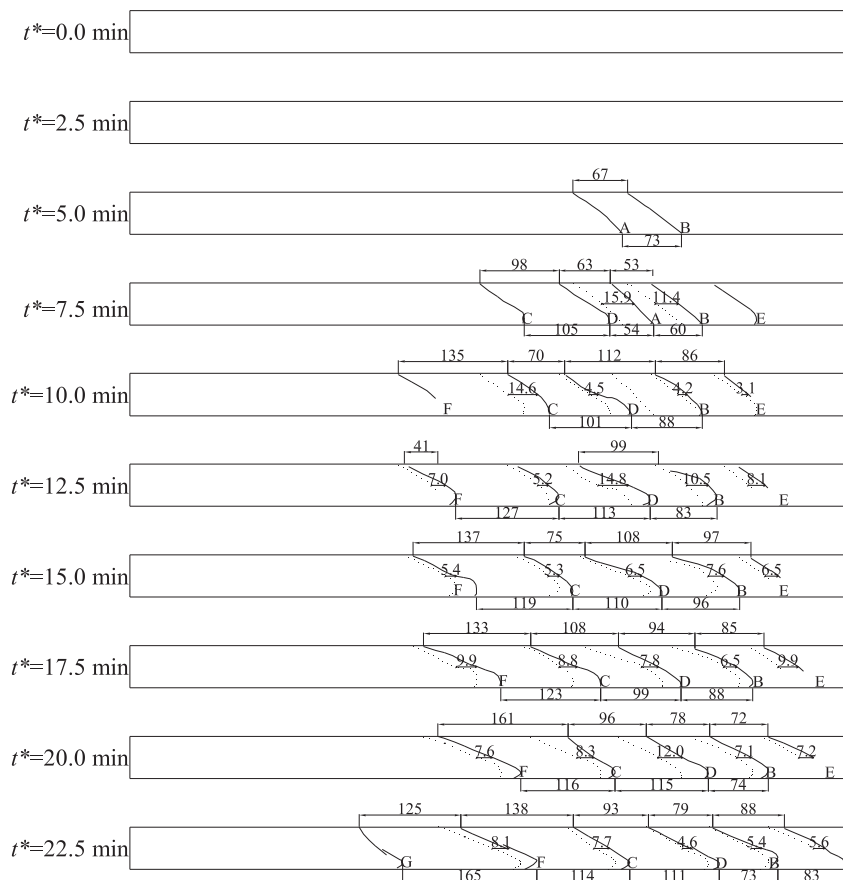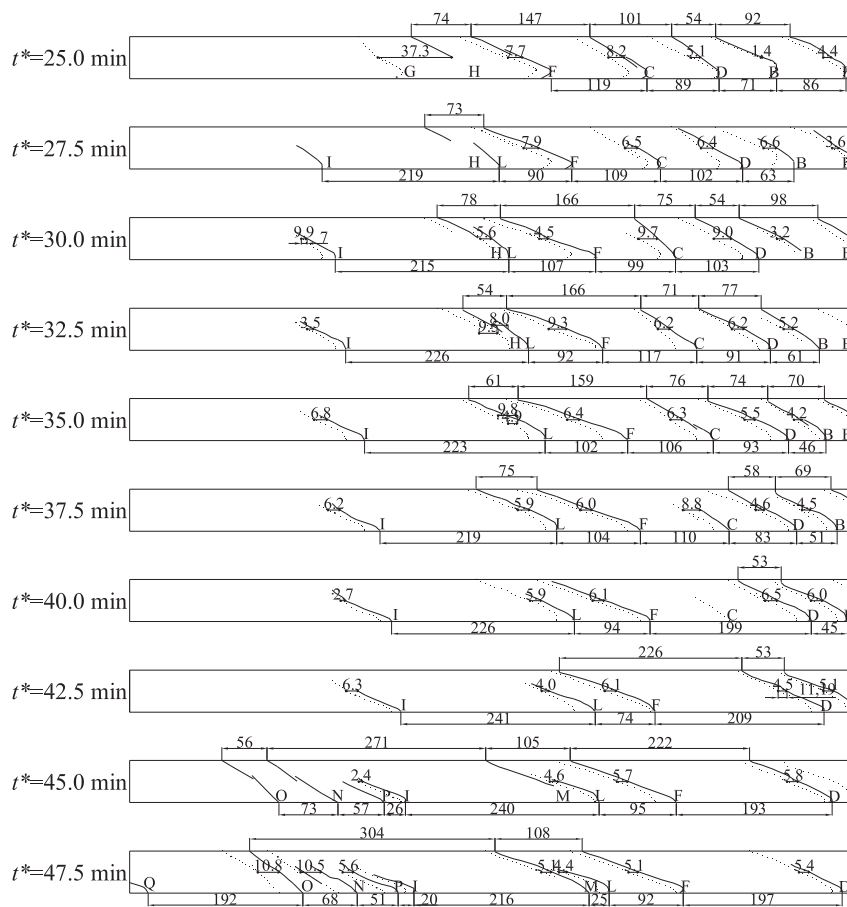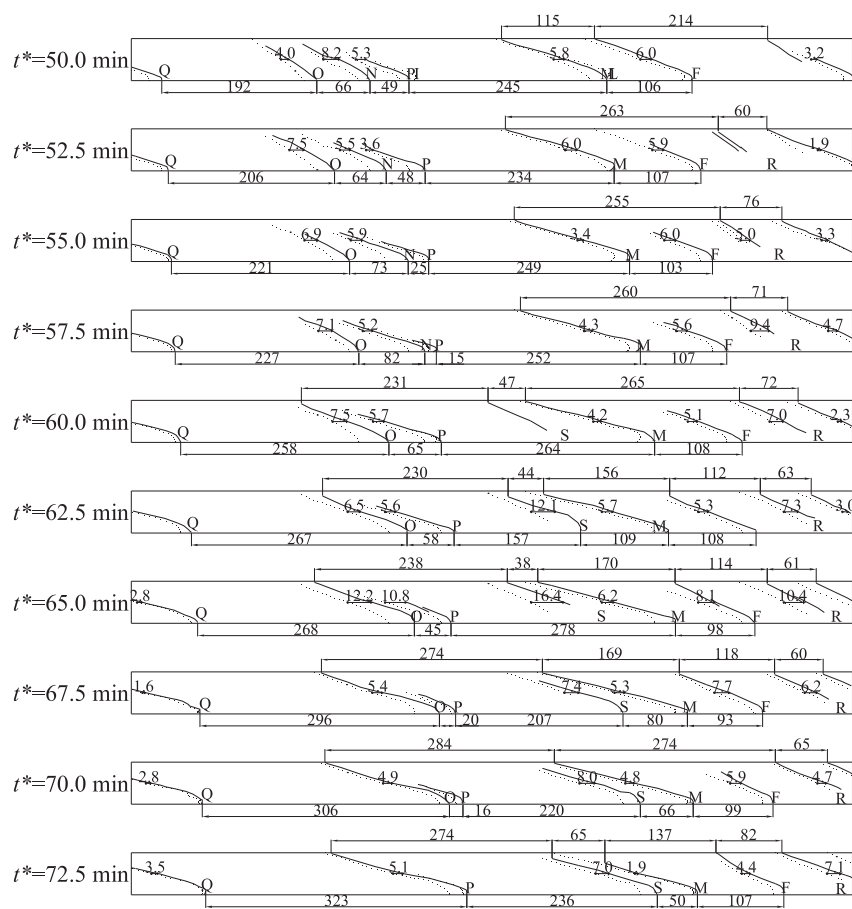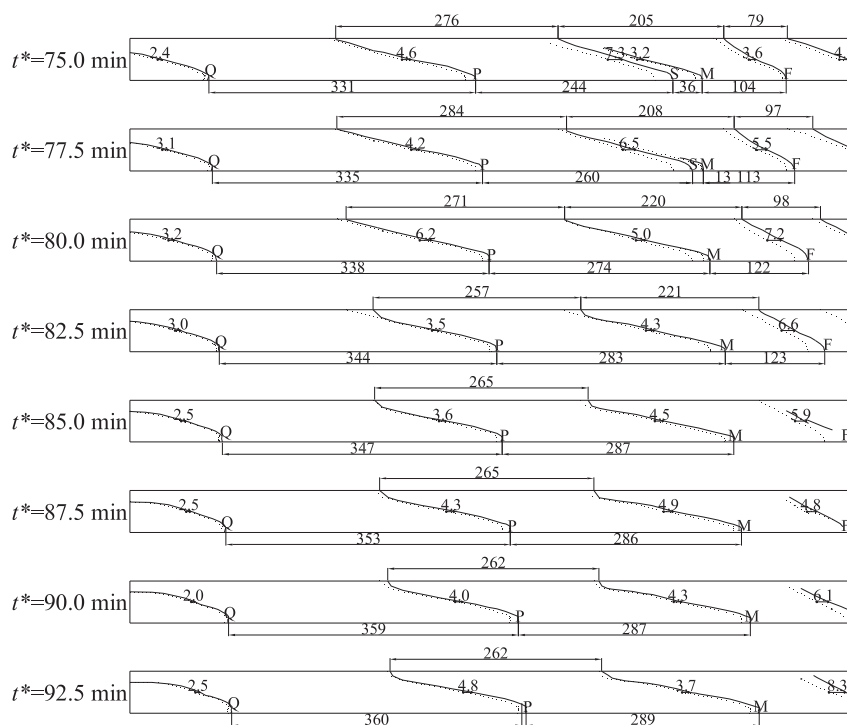
Appendix C

Derivation of Dressler's equations

In the following we report a scheme useful to interpret the derivation of Dressler's equations, as reported in his original work (Dressler, 1978). The references here reported, therefore, refer to the equations of Dressler (1978).

Continuity equation (6.01)		Continuity equation (7.01)
Momentum balance (6.02)		Momentum balance in s-n direction (7.02-7.03)
Irrotationality (6.03)	Change to curvilinear reference system (5.07-5.08)	Irrotationality (7.04)
Kinematic condition at the free surface (6.04)		Kinematic condition at the free surface (7.05)
Kinematic condition at the bottom (6.05)		Kinematic condition at the bottom (7.06)
No pressure at the free surface (6.06)		No pressure at the free surface (7.07)

```
┌─────────────────────────────┐   ┌──┐   ┌─────────────────────────────┐
│ Continuity equation (7.01)  │───│  │───│ Continuity equation (8.031) │
└─────────────────────────────┘   │  │   └─────────────────────────────┘
┌─────────────────────────────┐   │  │   ┌─────────────────────────────┐
│ Momentum balance in         │───│  │───│ Momentum balance in         │
│ s-n direction (7.02-7.03)   │   │  │   │ s-n direction (8.032-8.033) │
└─────────────────────────────┘   │  │   └─────────────────────────────┘
┌─────────────────────────────┐   │  │   ┌─────────────────────────────┐
│ Irrotationality (7.04)      │───│  │───│ Irrotationality (8.034)     │
└─────────────────────────────┘   │  │   └─────────────────────────────┘
┌─────────────────────────────┐   │  │   ┌─────────────────────────────┐
│ Kinematic condition at      │───│  │───│ Kinematic condition at      │
│ the free surface (7.05)     │   │  │   │ the free surface (8.035)    │
└─────────────────────────────┘   │  │   └─────────────────────────────┘
┌─────────────────────────────┐   │  │   ┌─────────────────────────────┐
│ Kinematic condition at      │───│  │───│ Kinematic condition at      │
│ the bottom (7.06)           │   │  │   │ the bottom (8.036)          │
└─────────────────────────────┘   │  │   └─────────────────────────────┘
┌─────────────────────────────┐   │  │   ┌─────────────────────────────┐
│ No pressure at              │───│  │───│ No pressure at              │
│ the free surface (7.07)     │   │  │   │ the free surface (8.037)    │
└─────────────────────────────┘   └──┘   └─────────────────────────────┘
```

Insert scaling (8.02)

		Continuity equation order 0 (10.01)

Continuity equation (8.031)

Momentum balance in s-n direction (8.032-8.033)

Irrotationality (8.034)

Kinematic condition at the free surface (8.035)

Kinematic condition at the bottom (8.036)

No pressure at the free surface (8.037)

Expansion in terms of σ(9.01-9.04)

Continuity equation order 0 (10.01)

Kinematic condition at free surface-order 0 (10.02)

Kinematic condition at the bottom-order 0 (10.03)

No pressure at the free surface-order 0 (10.05)

Continuity equation order 1 (12.01)

Momentum balance in s direction-order 1 (12.02)

Momentum balance in n direction-order 1 (12.03)

Kinematic condition at free surface-order 1 (12.04)

Kinematic condition at the bottom-order 1 (12.05)

```
┌─────────────────────────┐
│  Continuity equation    │────┐                  ┌──────────────────────────┐
│  order 0 (10.01)        │    │                  │  Transversal velocity profile │
└─────────────────────────┘    ├──────────────────│  order 0 (10.04)         │
┌─────────────────────────┐    │                  └──────────────────────────┘
│  Kinematic condition at │────┘
│  the bottom-order 0 (10.03) │
└─────────────────────────┘

┌─────────────────────────┐
│  Transversal velocity profile │────┐            ┌──────────────────────────┐
│  order 0 (10.04)        │    │                  │  Longitudinal velocity profile │
└─────────────────────────┘    ├──────────────────│  order 0 (10.06)         │
┌─────────────────────────┐    │                  └──────────────────────────┘
│  Kinematic condition at │    │
│  the free surface       │────┘
│  order 0 (10.02)        │
└─────────────────────────┘

┌─────────────────────────┐
│  Longitudinal velocity profile │──┐
│  order 0 (10.06)        │    │
└─────────────────────────┘    │
┌─────────────────────────┐    │            ┌──────────────────────────┐
│  Continuity equation    │────┼────────────│  Transversal velocity profile │
│  order 1 (12.01)        │    │            │  order 1 (12.06)         │
└─────────────────────────┘    │            └──────────────────────────┘
┌─────────────────────────┐    │
│  Kinematic condition at │────┘
│  the bottom-order 1 (12.05) │
└─────────────────────────┘

┌─────────────────────────┐
│  Momentum balance in    │────┐            ┌──────────────────────────┐
│  n direction-order 1    │    │            │  Pressure profile        │
│  (12.03)                │    ├────────────│  order 0 (12.031)        │
└─────────────────────────┘    │            └──────────────────────────┘
┌─────────────────────────┐    │
│  No pressure at the free │────┘
│  surface-order 0 (10.05) │
└─────────────────────────┘
```

Longitudinal velocity profile order 0 (10.06)	
Momentum balance in s direction-order 1 (12.02)	Momentum equation (12.07)
Pressure profile order 0 (12.031)	

Kinematic condition at free surface-order 1 (12.04)	Continuity equation (12.08)
Transversal velocity profile order 1 (12.06)	

Appendix D

Coefficients of Chapter 2

D.1 Parameters of the mechanistic sediment transport model

D.1.1 Parameters in flat bed conditions

$$R_0 = \frac{R\mu_{d0}}{F_0^2(R+1)},$$

$$S_0 = \frac{4\mu_{d0}(3\lambda^2\theta_{ch}f^2)^{-1}}{c_s d_s(R+1)},$$

$$T_0 = \frac{F_0^2\mu_{d0}(1-p)}{\lambda^2\theta_{ch}f^2 d_s^2 R},$$

where $c_s = 4/3$, $\lambda = 0.7$, $\theta_{ch} = 0.047$, $p = 0.4$ and for silicate sediments $R = 1.65$.

D.1.2 Correction coefficients to account for gravity

$$r_{sc} = \cos\alpha\left(1 + \frac{\tan\alpha}{\mu}\right),$$

$$r_\mu = 1 + \frac{\tan\alpha}{\mu} - \frac{\tan\alpha}{\mu_{d0}},$$

$$r_{dc} = \cos\alpha\left(1 + \frac{\tan\alpha}{\mu_d}\right),$$

$$r_e = [1 + (1 - r_\mu r_{dc})K_0]^{-3/2},$$

$$r_s = (r_\mu r_{dc})^{-1/2},$$

$$r_\lambda = \left(\frac{r_{sc}}{r_{dc}}\right)^{1/2},$$

$$\mu_d = \mu_{d0}r_\mu,$$

$$R_\mu = R_0 r_\mu r_{dc},$$

$$S_\mu = S_0\frac{r_\mu}{r_\lambda^2},$$

$$T_\mu = T_0\frac{r_\mu}{r_\lambda^2},$$

$$\theta_c = \theta_{ch}r_{sc},$$

where $\mu_{d0} = 0.3$ and $\mu = 0.6$.

D.1.3   Parametrs of the linearized problem

$$\rho_0 = \left(\frac{A_s - A_s p}{\sqrt{p_3}d_s^2}\right)^{2/3}\left(\frac{\mathrm{R}_0(-J+\mu)}{\mathcal{J}S_0\mu}\right)^{1/6}\left(\frac{A_e}{p_1^{3/2}d_s}\right)^{-2/3} + \sqrt{\frac{\mathrm{R}_0(\mu-J)}{\mathcal{J}S_0\mu}},$$

$$\rho_1 = \frac{2\mathcal{J}^2 + \mathrm{i}kJ - 2\mathcal{J}k\left(-\mathrm{i}J + F_0^2 k\right)}{2\mathcal{J}^3},$$

$$\rho_2 = \frac{\sqrt{J}v_0}{f^2\sqrt{J}S_0 - fF_0\mathcal{J}S_0 v_0},$$

$$\rho_3 = \frac{\sqrt{J}R_0(1+J\mu)}{f\mathcal{J}^3 S_0\left(f\sqrt{J}-F_0\mathcal{J}v_0\right)\mu},$$

$$\rho_4 = \frac{2A_s J\Gamma_5}{d_s \mathcal{J}^2 R},$$

$$\rho_5 = \frac{A_s c_D F_0^2 \Gamma_5}{d_s R},$$

$$\rho_6 = \frac{2\sqrt{J}T_0\xi_0(A_s\Gamma_5 - A_e\Gamma_6)}{F_0\mathcal{J}},$$

$$\rho_7 = \frac{F_0}{d_s R T_0 \xi_0},$$

$$\rho_8 = -f + \frac{F_0\mathcal{J}v_0}{\sqrt{J}},$$

$$\rho_9 = \frac{A_s\Gamma_1\Gamma_5}{A_s\Gamma_5 - A_e\Gamma_6},$$

$$\rho_{10} = -\frac{\rho_4\left[A_s\Gamma_2\Gamma_5 + A_e(\Gamma_4\theta_{ch} + \Gamma_3\theta_{f0})\right]\Gamma_6}{A_s\Gamma_5 - A_e\Gamma_6},$$

$$\Gamma_1 = \frac{2\theta_{s0}}{\xi_0},$$

$$\Gamma_2 = \frac{-\mathrm{i}k\theta_{s0}(1+J\mu)}{p_4\mathcal{J}^2\mu},$$

$$\Gamma_3 = \frac{\mathrm{i}kK_0(1+J\mu)}{p_1\mathcal{J}^3\mu},$$

$$\Gamma_4 = -\frac{\mathrm{i}k(1+J\mu)\left(p_1\mathcal{J}^2\mu + K_0\mathcal{J}(\mu-J)\right)}{p_1\mathcal{J}^5\mu^2},$$

$$\Gamma_5 = -\frac{p_3(p-1)\mathcal{J}\xi_0}{2p_4 d_s^2 \sqrt{\theta_{s0}}},$$

$$\Gamma_6 = -\frac{3p_2}{2p_1^{3/2} d_s},$$

$$p_1 = 1 + K_0\left(1 - \frac{K_1 K_2}{\mathcal{J}}\right),$$

$$p_2 = \sqrt{\frac{J}{R d_s \mathcal{J}} - \theta_{s0} - \theta_{ch}\left(\frac{\mu - J}{\mathcal{J}}\right)},$$

$$p_3 = \sqrt{\frac{K_1 K_2^{\,2}}{\mathcal{J}}},$$

$$p_4 = K_1 K_2,$$

$$\theta_{s0} = T_0 \xi_0 \left(f\frac{\sqrt{J}}{F_0 \mathcal{J}} - v_0\right)^2,$$

$$K_0 = (\mu_{do} Ae/As)^{2/3},$$

$$K_1 = \left(1 - \frac{J}{\mu} + \frac{J}{\mu_{do}}\right),$$

$$K_2 = \left(1 - \frac{J}{\left(1 - \frac{J}{\mu} + \frac{J}{\mu_{do}}\right)\mu_{do}}\right).$$

Appendix E

List of symbols

E.1 Chapeter 1

$\boldsymbol{A}$ Operator which describes the temporal evolution of $\boldsymbol{q}_{(}t)$

$\boldsymbol{A}_M$ Operator which describes the temporal evolution of $\boldsymbol{q}_M(t)$

B Dimensionless channel half width

B^* Channel half width

c Reduction coefficient used for focusing on the morpho-dynamic energy transfers

C Friction coefficient

C_0 Dimensionless unperturbed longitudinal shear stress

d_s Dimensionless sediment diameter

d_s^* Sediment diameter

D Dimensionless flow depth

D^* Flow depth

D_0^* Unperturbed flow depth

D_1 Flow depth perturbation

d_1 Time dependent amplitude of the harmonic flow depth perturbation

E — Total energy of the perturbation

E_M — Morphological energy of the perturbation

F_0 — Froude number

g — Gravity acceleration

$\hat{G}(t)$ — Growth function of $\boldsymbol{q}(t)$

$\hat{G}_M(t)$ — Growth function of $\boldsymbol{q}_M(t)$

$\hat{G}_{\mathrm{max}}$ — Absolute maximum of the growth function of $\boldsymbol{q}(t)$

$\hat{G}_{M,\mathrm{max}}$ — Absolute maximum of the growth function of $\boldsymbol{q}_M(t)$

k — Perturbation longitudinal wavenumber

$\bar{k}$ — Average value of the observed wavenumber

k_{asy} — Most unstable wavenumber (asymptotically) according to the linear theory

$\bar{k}_{\mathrm{fast}}$ — Average value of the observed wavenumber of the fast moving fronts

$\bar{k}_{\mathrm{slow}}$ — Average value of the observed wavenumber of the slowly moving fronts

K — Kinetic energy of the perturbation

K_0 — Initial value of the kinetic energy of the perturbation

$K()$ — Kreiss constant of the argument

H — Dimensionless water height

H^* — Water height

H_0 — Dimensionless unperturbed water height

H_0^* — Unperturbed water height

H_1 — Water height perturbation

h_1 — Time dependent amplitude of the harmonic water height perturbation

$\boldsymbol{H}()$ Hermitian part of the argument

$\boldsymbol{I}$ Identity matrix

m Transversal mode of the perturbation

n Dimensionless transversal coordinate

n^* Transversal coordinate

N Matrix dimension

N_j Number of fronts recorded at the $j-$th survey

p Porosity

P Potential energy of the perturbation

P_0 Initial value of the potential energy of the perturbation

P_b Bed potential energy of the perturbation

P_{b0} Initial value of the bed potential energy of the perturbation

P_s Free surface potential energy of the perturbation

P_{s0} Initial value of the free surface potential energy of the perturbation

q_i $i-$th component of $\boldsymbol{q}(t)$

$\boldsymbol{q}(t)$ Vector containing the different component of the energy perturbation

$\boldsymbol{q}_0$ Initial value of the different component of the energy perturbation

$\hat{\boldsymbol{q}}_0$ Optimal initial value of the different component of the energy perturbation

q_{Mi} $i-$th component of $\boldsymbol{q}_M(t)$

$\boldsymbol{q}_M(t)$ Vector containing the different component of the morphological energy perturbation

$\boldsymbol{q}_{0M}$ Initial value of the different component of the morphological energy perturbation

$\hat{\boldsymbol{q}}_{0M}$ Optimal initial value of the different component of the morphological energy perturbation

Q_l^* Liquid discharge

Q_n Dimensionless transversal sediment transport rate

Q_n^* Transversal sediment transport rate

Q_{n1} Transversal sediment transport rate perturbation

Q_0 Solid-liquid discharges ratio

Q_s Dimensionless longitudinal sediment transport rate

Q_s^* Longitudinal sediment transport rate

Q_{s1} Longitudinal sediment transport rate perturbation

r Experimental coefficient used for defining the direction of the bedload flux over inclined slopes

s Dimensionless longitudinal coordinate

s^* Longitudinal coordinate

s_{max} Larger singular value

S Unperturbed bed slope

t Dimensionless temporal coordinate

t_1 Time when $\hat{G}(t_1) = 1$

t^* Temporal coordinate

t_* Generic instant

$\hat{t}$ t/t_{asy}

t_j^* Instant in which the bottom configuration is recorded for the $j-$th time

t_{asy} Time when bar pattern reaches a stable wavelength

t_{max} Time when the growth function has its absolute maximum

t_{vis} Time when the bar pattern become detectable by naked eyes

T First-order moment of the area subtended by $\hat{G}(t)$

T_{osc} Period of the typical oscillation

U Dimensionless longitudinal velocity

U^* Longitudinal velocity

U_0^* Unperturbed longitudinal velocity

U_1 Longitudinal velocity perturbation

u_1 Time dependent amplitude of the harmonic longitudinal velocity perturbation

$\boldsymbol{U_r}$ Right unitary matrix

$\boldsymbol{U_l}$ Left unitary matrix

$v_p(k)$ Front phase velocity evaluated as a function of k from the linear theory

v_p^* Measured front phase velocity

$v_{p,\mathrm{fast}}^*$ Phase velocity of a front moving fast

$\bar{v}_{p,\mathrm{fast}}^*$ Average phase velocity of fronts moving fast

$v_{p,\mathrm{slow}}^*$ Phase velocity of a front moving slowly

$\bar{v}_{p,\mathrm{slow}}^*$ Average phase velocity of fronts moving slowly

V Dimensionless transversal velocity

V^* Transversal velocity

V_1 Transversal velocity perturbation

v_1 Time dependent amplitude of the harmonic transversal velocity perturbation

165

$\boldsymbol{V}$ Matrix of eigenvector

$W()$ Rayleigh quotients of the argument

z Dimensionless vertical coordinate

z^* Vertical coordinate

β Aspect ratio

δ Angle between sediment flux ans shear stress

ϵ Parameter $\lll 1$

η Dimensionless bed elevation

η^* Bed elevation

η_0 Dimensionless unperturbed bed elevation

η_0^* Unperturbed bed elevation

η_1 Time dependent amplitude of the harmonic bed elevation perturbation

θ Schields parameter

θ' Modified Schields parameter

θ_c Critical Schields parameter of motion threshold

$\kappa()$ Condition number of the argument

$\lambda_{i,j}^*$ Wavelenth of the $i-$th front recorded at the $j-$th instant

$\bar{\lambda}_j^*$ Average wavelenth between fronts recorded at the $j-$th instant

λ_{asy} Most unstable wavelength (asymptotically) according to the linear theory

λ_{min} Shortest wavelength observed

λ_{slow} Average value of the observed wavelength of the slowly moving fronts

λ_{fast} Average value of the observed wavelength of the fast moving fronts

$\Lambda()$ Spectrum of the argument

$\Lambda_\epsilon()$ Pseudospectrum of the argument

Π Porosity parameter

ρ Water density

ρ_s Sediment density

σ_i $i-$th eigenvalue

$\hat{\sigma}_j^*$ Standard deviation of the wavelength distribution recorded at the $j-$th instant

Σ Matrix of singular values

τ_n Dimensionless transversal shear stress

τ_n^* Transversal shear stress

τ_{n1} Transversal shear stress perturbation

τ_s Dimensionless longitudinal shear stress

τ_s^* Longitudinal shear stress

τ_0^* Unperturbed longitudinal shear stress

τ_{s1} Longitudinal shear stress perturbation

Φ Longitudinal sediment transport rate

Φ_0 Dimensionless unperturbed longitudinal sediment transport rate

$\omega()$ Numerical abscissa of the argument

167

E.2 Chapeter 2

a	Velocity of the x/t ray
A	Dimensionless dynamical friction
A^*	Dynamical friction
A_e	Experimental constant
A_s	Experimental constant
$\mathcal{A}$	homogeneous part of the linearized system
b	non-homogeneous part of the linearized system
c	perturbation phase celerity
C	Friction coefficient
$\mathcal{C}$	$1 - \kappa n$
d_s	Dimensionless sediment diameter
d_s^*	Sediment diameter
$\mathcal{D}$	Deposition rate
D	Dimensionless flow depth
D^*	Flow depth
D_0^*	Unperturbed flow depth
D_0	Dimensionless unperturbed flow depth
d_1	Amplitude of the harmonic perturbation of the flow depth
$\mathcal{E}$	Erosion rate
f	Experimental constant
F	Dimensionless drag force
F^*	Drag force
F_0	Froude number

F_c	Critical Froude number for roll waves formation
g	Gravity acceleration
G	Dimensionless particle weight
G^*	Particle weight
$G_\parallel$	Dimensionless particle weight parallel to the bottom
$G_\parallel^*$	Particle weight parallel to the bottom
$G_\perp$	Dimensionless particle weight perpendicular to the bottom
$G_\perp^*$	Particle weight perpendicular to the bottom
J	Slope in unperturbed conditions
k	Perturbation longitudinal wavenumber
k_i	Imaginary part of the perturbation longitudinal wavenumber
k_r	Real part of the perturbation longitudinal wavenumber
k_h	Higher unstable wavenumber
k_l	Lower unstable wavenumber
$k_{\max}$	Most unstable wavenumber
k_0	Complex solution of the saddle point condition
k_{0i}	Imaginary part of the solution of the saddle point condition
k_{0r}	Real part of the solution of the saddle point condition
$k_{0,j}$	$j-$th pinching point
$k_{(}^+ \Omega_{0r})$	Positive spatial branch of the dispersion relation
$k_{(}^- \Omega_{0r})$	Negative spatial branch of the dispersion relation
h_s	Dimensionless bed load layer thickness

h_s^*	Bed load layer thickness
I	Dimensionless particle inertia
I^*	Particle inertia
n	Dimensionless curvilinear transversal coordinate
n^*	Curvilinear transversal coordinate
$\mathcal{N}$	$1 - \kappa D$
$\mathcal{P}$	Dimensionless pressure
p	Porosity
q	Dimensionless sediment transport
q^*	Sediment transport
q_0^*	Unperturbed sediment transport
q_0	Dimensionless unperturbed sediment transport
q_1	Amplitude of the harmonic perturbation of the sediment transport
R	Sediment relative density
Re_e	Equivalent Reynold number
s	Dimensionless curvilinear longitudinal coordinate
s^*	Curvilinear longitudinal coordinate
t	Dimensionless temporal coordinate
t^*	Temporal coordinate
U	Dimensionless longitudinal velocity at the bottom
U^*	Longitudinal velocity at the bottom
U_0^*	Unperturbed longitudinal velocity at the bottom
U_0	Dimensionless unperturbed longitudinal velocity at the bottom

U_1	Amplitude of the harmonic perturbation of the longitudinal velocity at the bottom
$\mathcal{U}$	Dimensionless longitudinal velocity
v	Dimensionless sediment particle velocity
v^*	Sediment particle velocity
v_0^*	Unperturbed sediment particle velocity
v_0	Dimensionless unperturbed sediment particle velocity
v_1	Amplitude of the harmonic perturbation of the sediment particle velocity
$\mathcal{V}$	Dimensionless transversal velocity
V	Dimensionless transversal velocity at the bottom
x	Dimensionless cartesian horizontal coordinate
x^*	Cartesian horizontal coordinate
$\mathbf{X}$	$\{U, D, v, \xi\}$
$\mathbf{X}_1$	$\{u_1, d_1, v_1, \xi_1\}$
y	Dimensionless cartesian vertical coordinate
y^*	Cartesian vertical coordinate
α	Local slope
$\beta_{\max}$	Group velocity of the perturbation with maximum grow rate
γ	$\cos \alpha$
ϵ	Parameter $\lll 1$
η	Dimensionless bed elevation
η^*	Bed elevation
η_0^*	Unperturbed bed elevation

η_0 Dimensionless unperturbed bed elevation

η_1 Amplitude of the harmonic perturbation of the bed elevation

θ Schields parameter

θ_c Critical Schields parameter of motion threshold

θ_{ch} Critical Schields parameter of motion threshold for horizontal bed

θ_B Total shear stress at the bottom expressed as Schields parameter

θ_f Shear stress exerted by the fluid at the bottom expressed as Schields parameter

θ_s Shear stress exerted by the sediment at the bottom expressed as Schields parameter

Θ Solid-liquid discharges ratio

κ Local curvature

μ_d Dynamical friction coefficient

ν_e Equivalent eddy viscosity

ξ Dimensionless concentration of sediment particle in motion

ξ^* Concentration of sediment particle in motion

ξ_0^* Unperturbed concentration of sediment particle in motion

ξ_0 Dimensionless unperturbed concentration of sediment particle in motion

ξ_1 Amplitude of the harmonic perturbation of the concentration of sediment particle in motion

Π Longitudinal pressure gradient evaluated at the bottom

ρ Water density

ρ_s	Sediment density
σ	Channel shallowness
τ_B	Dimensionless total shear stress at the bottom
τ_B^*	Total shear stress at the bottom
τ_I	Dimensionless shear stress exerted by the fluid at the interface with the bed load layer
τ_I^*	Shear stress exerted by the fluid at the interface with the bed load layer
τ_f	Dimensionless shear stress exerted by the fluid at the bottom
τ_f^*	Shear stress exerted by the fluid at the bottom
τ_s	Dimensionless shear stress exerted by the sediment at the bottom
τ_s^*	Shear stress exerted by the sediment at the bottom
ϕ_{q_1}	Phase of the the perturbation of the sediment transport rate with respect of the bottom perturbation
ϕ_{v_1}	Phase of the the perturbation of the particle velocity with respect of the bottom perturbation
ϕ_{ξ_1}	Phase of the the perturbation of the concentration of the moving particles with respect of the bottom perturbation
$\psi()$	Temporal grow rate along the ray given in the argument
Ω	Complex temporal grow rate of the perturbation
Ω_i	Imaginary part of the temporal grow rate of the perturbation
Ω_r	Real part of the temporal grow rate of the perturbation
$\tilde{\Omega}$	Generic temporal grow rate of the perturbation
Ω_{0r}	Absolute grow rate at saddle point

173

$\Omega_{r,\max}$ Grow rate of the most unstable wavenumber

$\Omega_{0r,j}$ Grow rate of the $j-$th pinching point

Bibliography

AHNERT, F., 1960 Estuarine meanders in the Chesapeake Bay area. *Geograph. Rev.* **50**, 390–401.

AMSLER, M. L. & GARCIA, M. H., 1997 Sand-dune geometry of large rivers during floods - discussion. *J. Hydraul. Eng.-ASCE* **123**(6), 582–585.

AMSLER, M. L.; PRENDES, H. H.; MONTAGNINI, M. D.; SZUPIANY, R. & GARCIA, M. H., 2003 Prediction of dune height in sand-bed rivers: the case of the Paranà river, Argentina. In *Proceedings of the 3rd IAHR Symposium on River, Coastal and Estuarine Morphodynamics*. IAHR Secret, Madrid, 1104–1113.

ANDREOTTI, B., 2004 A two-species model of aeolian sand transport. *J. Fluid Mech.* (510), 47–70.

ANDREOTTI, B.; CLAUDIN, P. & DOUADY, S., 2002 Selection of dune shapes and velocities part 1: Dynamics of sand, wind and barchans. *Eur. Phys. J. B* **28**(3), 321–339.

ANTIA, E. E., 1996 Shoreface-connected ridges in German and us mid-Atlantic bights: similarities and contrasts. *J. Coastal Res.* **12**(1), 141–146.

ARGYRIS, J.; FAUST, G. & HAASE, M., 1994 *An Exploration of chaos*, Texts Comput. Mech., 7. Elsevier, New York.

ASHIDA, K. & MICHIUE, M., 1972 Study on hydraulic resistence and bedload transport rate in alluvial streams. *Trans. Japan Soc. Civil Eng.* **206**, 56–59 (in Japanese).

ASHMORE, P., 1982 Laboratory modelling of gravel braided stream morphology. *Earth Surf. Process. Landf.* **7**, 201–225.

ASHMORE, P., 1991 How do gravel-bed rivers braid? *Can. J. Earth Sci.* **28(3)**, 326–341.

ASHMORE, P.; BERTOLDI, W. & TOBIAS GARDNER, J., 2011 Active width of gravel-bed braided rivers. *Earth Surf. Processes* **36**(11), 1510–1521.

ASHMORE, P. & PARKER, G., 1983 Confluence scour in coarse braided streams. *Water. Resour. Res.* **19**(2), 392–402.

ASHMORE, P. E., 1988 Bed load transport in braided gravel-bed stream models. *Earth Surf. Processes* **13**(8), 677–695.

ASHTON, A. D. & MURRAY, A. B., 2006 High-angle wave instability and emergent shoreline shapes: 1. modeling of sand waves, flying spits, and capes. *J. Geophys. Res.* **111**(f4).

ASHWORTH, P. J.; BEST, J. L.; RODEN, J. E.; BRISTOW, C. S. & KLAASSEN, G. J., 2000 Morphological evolution and dynamics of a large, sand braid-bar, Jamuna River, Bangladesh. *Sedimentology* **47**(3), 533–555.

AUTON, T. R., 1987 Lift force on a spherical body in a rotational flow. *J. Fluid Mech.* **183**, 199–218.

BALMFORTH, N. & MANDRE, S., 2004 Dynamics of roll waves. *J. Fluid Mech.* **514**, 1–33.

BALMFORTH, N. J. & VAKIL1, A., 2012 Cyclic steps and roll waves in shallow water over an erodible bed. *J. Fluid Mech.* **695**, 35–62.

BARDINI, L.; BOANO, F.; CARDENAS, M. B.; REVELLI, R. & RIDOLFI, L., 2012 Nutrient cycling in bedform induced hyporheic zones. *Geochimica et Cosmochimica Acta* **84**, 47–61.

BATTJES, J. A., 1988 Surf-zone dynamics. *Annu. Rev. Fluid Mech.* **20**, 257–293.

BAYANI CARDENAS, M., 2008 The effect of river bend morphology on flow and timescales of surface water-groundwater exchange across pointbars. *J. Hydrol.* **362**(1-2), 134–141.

BEETS, D. J. & VAN DER SPEK, A. J. F., 2000 The Holocene evolution of the barrier and the back-barrier basins of Belgium and the Netherlands as a function of late Weichselian morphology, relative sea-level rise and sediment supply. *Neth. J. Geosc.* **79**(1), 3–16.

BENJAMIN, T. B., 1959 Shearing flow over a wavy boundary. *J. Fluid Mech.* **6**, 161–205.

BERS, A., 1983 Space-time evolution of plasma instabilities – absolute and convective. In *Handbook of Plasma Physics* , editors, ROSENBLUTH, M. & SAGDEEV, R.. North Holland, Amsterdam, 159–229.

BEST, J., 2005 The fluid dynamics of river dunes: a review and some future research directions. *J. Geophys. Res.* **110**(f4).

BEST, J. L.; ASHWORTH, P. J.; BRISTOW, C. S. & RODEN, J., 2003 Three-dimensional sedimentary architecture of a large, mid-channel sand braid bar, Jamuna River, Bangladesh. *J. Sediment. Res.* **73**(4), 516–530.

BIRNBAUM, G.; FREITAG, J.; BRAUNER, R.; KOENIGLANGLO, G.; SCHULZ, E.; KIPFSTUHL, S.; OERTER, H.; REIJMER, C. H.; SCHLOSSER, E.; FARIA, S. H.; RIES, H.; LOOSE, B.; HERBER, A.; DUDA, M. G.; POWERS, J. G.; MANNING, K. W. & VAN DEN BROEKE, M. R., 2010 Strong-wind events and their influence on the formation of snow dunes: observations from Kohnen Station, Dronning Maud Land, Antarctica. *J. Glaciol.* **56**(199), 891–902.

BLANK, H. R., 1970 Incised meanders in Mason County, Texas. *Geol. Soc. Am. Bull.* **81**(10), 3135–3140.

BLOM, A.; RIBBERINK, J. S. & DE VRIEND, H. J., 2003 Vertical sorting in bed forms: flume experiments with a natural and a trimodal sediment mixture. *Water. Resour. Res.* **39**(2), esg11–esg113.

BLONDEAUX, P., 2001 Mechanics of coastal forms. *Annu. Rev. Fluid Mech.* **33**, 339–370.

177

BLONDEAUX, P. & SEMINARA, G., 1985 A unified bar-bend theory of river meanders. *J. Fluid Mech.* **157**, 449–470.

BLUMBERG, P. N. & CURL, R. L., 1974 Experimental and theoretical studies of dissolution roughness. *J. Fluid Mech.* **65**(4), 735–751.

BOHLKE, J. K.; ANTWEILER, R. C.; HARVEY, J. W.; LAURSEN, A. E.; SMITH, L. K.; SMITH, R. L. & VOYTEK, M. A., 2009 Multi-scale measurements and modeling of denitrification in streams with varying flow and nitrate concentration in the upper Mississippi River Basin, USA. *Biogeochemistry* **93**(1-2), 117–141.

BOULTON, A. J.; FINDLAY, S.; MARMONIER, P.; STANLEY, E. & MAURICE VALETT, H., 1998 The functional significance of the hyporheic zone in streams and rivers. *Annu. Rev. Ecol. Syst.* **29**, 59–81.

BOUTOUNET, M.; CHUPIN, L.; NOBLE, P. & VILA, J. p., 2008 Shallow water viscous flows for arbitrary topography. *Commu. Math. Sc.* **6**(1).

BRENNEN, C. & WINET, H., 1977 Fluid-mechanics of propulsion by cilia and flagella. *Annu. Rev. Fluid Mech.* **9**, 339–398.

BRIGGS, R. J., 1964 *Electron-Stream Interaction with Plasma.* M.I.T. Press, Boston.

BROCK, R. R., 1969 Development of roll-wave trains in open channels. *J. Hydraul. Div.* **95**, 1401–1427.

BROWN, A. G., 1997 Biogeomorphology and diversity in multiple-channel river systems. *Global Ecol Biogeogrs* **6(3-4)**, 179–185.

BROWNLIE, W. R., 1981 Prediction of flow depth and sediment discharge in open channels. *Technical Report 43*, W. M. Keck Laboratory of Hydraulics and Water Resources, California Institute of Technology, Pasadena, California, USA.

BRUNKE, M. & GONSER, T., 1997 The ecological significance of exchange processes between rivers and groundwater. *Freshwater. Biol.* **37**(1), 1–33.

CALLANDER, R. A., 1969 Instability and river channels. *J. Fluid Mech.* **36**, 465–480.

CAMPOREALE, C.; CANUTO, C. & RIDOLFI, L., 2012 A spectral approach for the stability analysis of turbulent open-channel flows over granular beds. *Theor. Comp. Fluid Dyn.* **26**, 51–80.

CAMPOREALE, C.; GATTI, F. & RIDOLFI, L., 2009 Flow nonnormality-induced transient growth in superposed newtonian and non-newtonian fluid layers. *Phys. Rev. E* **80**(3), 036 312.

CAMPOREALE, C.; PERONA, P.; PORPORATO, A. & RIDOLFI, L., 2005 On the long-term behavior of meandering rivers. *Water. Resour. Res.* **41**(12), 1–13.

CAMPOREALE, C.; PERONA, P.; PORPORATO, A. & RIDOLFI, L., 2007 Hierarchy of models for meandering rivers and related morphodynamic processes. *Rev. Geophysics* **45**, RG1001.

CAMPOREALE, C. & RIDOLFI, L., 2006 Convective nature of the planimetric instability in meandering river dynamics. *Phys. Rev. E* **73**, 026 311.

CAMPOREALE, C. & RIDOLFI, L., 2009 Nonnormality and transient behavior of the de Saint-Venant-Exner equations. *Water Resour. Res.* **45**, W08 418.

CAMPOREALE, C. & RIDOLFI, L., 2011 Modal versus nonmodal linear stability analysis of river dunes. *Phys. Fluids.* **23**(10), 104 102.

CAMPOREALE, C. & RIDOLFI, L., 2012 Hydrodynamic-driven stability analysis of morphological patterns on stalactites and implications for cave paleoflow reconstructions. *Phys. Rev. Lett.* **108**(23).

CAMPOREALE, C. & RIDOLFI, L., 2012 Ice ripple formation at large Reynolds numbers. *J. Fluid Mech.* **694**, 225–251.

CAO, Z. & HU, P., 2008 Comment on "Long waves in erodible channels and morphodynamic influence" by Stefano Lanzoni *etal*. *Water Resour. Res.* **44**, 1–3.

179

CARLING, P. A.; GOLZ, E.; ORR, H. G. & RADECKI-PAWLIK, A., 2000a The morphodynamics of fluvial sand dunes in the River Rhine, near Mainz, Germany. I. Sedimentology and morphology. *Sedimentology* **47**(1), 227–252.

CARLING, P. A.; WILLIAMS, J. J.; GOLZ, E. & KELSEY, A. D., 2000b The morphodynamics of fluvial sand dunes in the River Rhine, near Mainz, Germany. II. Hydrodynamics and sediment transport. *Sedimentology* **47**(1), 253–278.

CASE, K., 1960 Stability of inviscid plane Couette flow. *Phys. Fluids* **3**(2), 143–148.

CASTELLE, B.; BONNETON, P. & DUPUIS, H., 2007 Double bar beach dynamics on the high-energy meso-macrotidal French Aquitanian coast: a review. *Mar. Geol.* **245**, 141 – 159.

CHABERT, J. & CHAUVIN, J. L., 1963 Formation de dunes et des rides dans les modeles fluviaux. *Technical Report 4*, Cen. Rech. ess. Chatou.

CHAN, P. Y. & GOLDENFELD, N., 2007 Steady states and linear stability analysis of precipitation pattern formation at geothermal hot springs. *Phys. Rev. E* **76**(4), 046 104.

CHAN-BRAUN, C.; GARCIA VILLALBA, M. & UHLMANN, M., 2011 Force and torque acting on particles in a transitionally rough open-channel flow. *J. Fluid Mech.* **684**, 441–474.

CHANG, H.; SIMONS, D. & WOOLHISER, D., 1971 Flume experiments on alternate bar formation. *J. Waterways, Harbors, and Coastal Eng. Div.* **97**, 155–165.

CHARRU, F.; ANDREOTTI, B. & CLAUDIN, P., 2013 Sand ripples and dunes. *Annu. Rev. Fluid Mech.* **45**, 469–493.

CHIEN, N., 1956 The present status of research on sediment transport. *Trans. ASCE* **121**, 833–868.

CHOW, V. T., 1959 *Open-channel hydraulics*. Mcgraw-Hill, New York.

CHUNG, Y. M., 2005 Unsteady turbulent flow with sudden pressure gradient changes. *Int. J. Numer. Meth. Fl.* **47**(8-9), 925–930.

COLEMAN, S. E. & FENTON, J. D., 2000 Potential-flow instability theory and alluvial stream bed forms. *J. Fluid Mech.* **418**, 101–117.

COLEMAN, S. E. & MELVILLE, B. W., 1996 Initiation of bed forms on a flat sand bed. *J. Hydraul. Eng.-ASCE* **122**(6), 301–309.

COLOMBINI, M., 1993 Turbulence-driven secondary flows and formation of sand ridges. *J. Fluid Mech.* **254**, 701–719.

COLOMBINI, M., 2004 Revisiting the linear theory of sand dunes. *J. Fluid Mech.* **502**, 1–16.

COLOMBINI, M.; SEMINARA, G. & TUBINO, M., 1987 Finite-amplitude alternate bars. *J. Fluid Mech.* **181**, 213–232.

COLOMBINI, M. & STOCCHINO, A., 2005 Coupling or decoupling bed and flow dynamics: Fast and slow sediment waves at high froude numbers. *Phys. Fluids* **17**, 036 602.

COLOMBINI, M. & STOCCHINO, A., 2008 Finite amplitude river dunes. *J. Fluid Mech.* **611**, 283–306.

COLOMBINI, M. & STOCCHINO, A., 2011 Ripple and dune formation in rivers. *J. Fluid Mech.* **673**, 121–131.

COLOMBINI, M. & STOCCHINO, A., 2012 Three-dimensional river bed forms. *J. Fluid Mech.* **695**, 63–80.

COLOMBINI, M. & TUBINO, M., 1991 Finite Amplitude free bars: a fully nonlinear spectral solution. In *Sand Transport in Rivers, Estuaries and the sea*, editors, SOULSBY, R. & BETTES, R.. A.A. Balkema, 163–169.

COPPOLA, G. & DE LUCA, L., 2006 On the transient growth oscillations in linear models. *Phys. Fluids* **18**, 078 104.

CORENBLIT, D.; BAAS, A. C.; BORNETTE, G.; DARROZES, J.; DELMOTTE, S.; FRANCIS, R. A.; GURNELL, A. M.; JULIEN,

F.; NAIMAN, R. J. & STEIGER, J., 2011 Feedbacks between geomorphology and biota controlling earth surface processes and landforms: A review of foundation concepts and current understandings. *Earth-Science Reviews* **106**, 307 – 331.

CRAIK, A. D. D., 1971 Non-linear resonant instability in boundary layers. *J. Fluid Mech.* **50**, 393.

CRASTER, R. V. & MATAR, O. K., 2009 Dynamics and stability of thin liquid films. *Rev. Mod. Phys.* **81**(3), 1131–1198.

CROCHET, M. J. & WALTERS, K., 1983 Numerical-methods in non-Newtonian fluid-mechanics. *Annu. Rev. Fluid Mech.* **15**, 241–260.

CROSATO, A. & MOSSELMAN, E., 2008 Simple physics-based predictor for the number of river bars and the transition between meandering and braiding. *Water Resour. Res.* **45**, W03 424.

DALRYMPLE, R. W. & RHODES, R. N., 1995 Estuarine dunes and bars. *Geom. Sed. Est.* **53**, 359–422.

DAVIS, R. A. & FITZGERALD, D. M., 2004 *Beaches and coasts.* Blackwell Publishing, Oxford.

DAYTON, P. K. & MARTIN, S., 1971 Observations of ice stalactites in Mcmurdo-Sound, Antarctica. *J. Geophys. Res.* **76**(6), 1595.

DE SWART, H. E. & ZIMMERMAN, J. T. F., 2009 Morphodynamics of tidal inlet systems. *Annu. Rev. Fluid Mech.* **41**, 203–229.

DEFINA, A., 2003 Numerical experiments on bar growth. *Water Resour. Res.* **39(4)**, 1–12.

DEN BERG, N. V.; FALQUES, A. & RIBAS, F., 2011 Long-term evolution of nourished beaches under high angle wave conditions. *J. Mar. Syst.* **88**(1), 102 – 112.

DEVAUCHELLE, O.; MALVERTI, L.; LAJEUNESSE, P.; LAGREE, P.-Y.; JOSSERAND, C. & THU-LAM, K.-D. N., 2010 Stability of bedforms in laminar flows with free surface: from bars to ripples. *J. Fluid Mech.* **642**, 329–348.

DiCristo, C.; Iervolino, M. & Vacca, A., 2006 Linear stability analysis of a 1D model with dynamical description of bed-load transport. *Journal of Hydraulic Research* **44**, 480–487.

Dressler, R. F., 1978 New nonlinear shallow-flow equations with curvature. *J. Hydraul. Res.* **16(3)**, 205–222.

Dressler, R. F. & Yevjevich, V., 1978 Hydraulic resistance terms modified for the Dressler curved flow equations. *J. Hydraul. Res.* **22(3)**, 145–156.

Dreybrodt, W., 1988 *Processes in karst systems.* Springer, New York.

Droge, E. H.-G. E., B., 1992 Channel erosion and erosion monitoring along the Rhine River. In *Proceedings of a symposium on erosion and sediment transport monitoring programmes in River Basins, 210.* IAHS Publication, 493–503.

Dyer, K. R. & Huntley, D. A., 1999 The origin, classification and modelling of sand banks and ridges. *Cont. Shelf Res.* **19**(10), 1285–1330.

Edgett, K. S. & Christensen, P. R., 1991 The particle size of Martian aeolian dunes. *J. Geophys. Res.* **96**(e5), 22 765–22 776.

Einstein, H. A., 1950 The bed-load function for sediment transport in open channels flows. *Technical Report 1026*, U.S. Dept. of Agriculture.

Engelund, F., 1970 Instability of erodible beds. *J. Fluid Mech.* **42**, 225–244.

Engelund, F., 1981 The motion of sediment particles on an inclined bed. *Technical Report 53*, Tech. Univ. Denmark ISVA.

Engelund, F. & Hansen, E., 1967 *A Monograph on Sediment Transport in Alluvial Streams.* Danish Technical Press, Denmark, first edition.

Engelund, F. & Skovgaa, O., 1973 Origin of meandering and braiding in alluvial streams. *J. Fluid Mech.* **57**(6), 289–302.

183

FAGHERAZZI, S. & OVEREEM, I., 2007 Models of deltaic and inner continental shelf landform evolution. *Annu. Rev. Earth. Pl. Sc.* **35**, 685–715.

FALQUES, A.; COCO, G. & HUNTLEY, D. A., 2000 A mechanism for the generation of wave-driven rhythmic patterns in the surf zone. *J. Geophys. Res.* **105**(c10), 24 071–24 087.

FEDERICI, B. & PAOLA, C., 2003 Dynamics of channel bifurcations in noncohesive sediments. *Water. Resour. Res.* **39**(6).

FEDERICI, B. & SEMINARA, G., 2003 On the convective nature of bar instability. *J. Fluid Mech.* **487**, 125–145.

FELTHAM, D. L. & WORSTER, M. G., 1999 Flow-induced morphological instability of a mushy layer. *J. Fluid Mech.* **391**, 337–357.

FERGUSON, R. I., 1973 Sinuosity of supraglacial streams. *Geol. Soc. Am. Bull.* **84**(1), 251–255.

FIELDING, C. R., 2006 Upper flow regime sheets, lenses and scour fills: Extending the range of architectural elements for fluvial sediment bodies. *Sedim. Geolog.* **190**, 227–240.

FINDLAY, S., 1995 Importance of surface-subsurface exchange in stream ecosystems: the hyperheic zone. *Limnol. Oceanogr.* **40**(1), 159–164.

FREDSØE, J., 1974 On the development of dunes in erodible channels. *J. Fluid Mech.* **64**, 1–16.

FREDSØE, J., 1978 Meandering and braiding in rivers. *J. Fluid Mech.* **57**, 289–302.

FREILE, D.; MILLIMAN, J. D. & HILLIS, L., 1995 Leeward bank margin halimeda meadows and draperies and their sedimentary importance on the Western Great Bahama bank slope. *Coral Reefs* **14**(1), 27–33.

FREZZOTTI, M.; GANDOLFI, S. & URBINI, S., 2002 Snow megadunes in Antarctica: sedimentary structure and genesis. *J. Geophys. Res.* **107**(18), 1–10.

FUJITA, Y. & MURAMOTO, Y., 1985 Studies on the process of development of alternate bars. *Technical Report 35*, Bulletin of the Disaster Prevention Research Institute.

FUKUOKA, S., 1989 Finite amplitude development of alternate bars. In *River Meandering*, editors, IKEDA, S. & PARKER, G.. AGU, 237–266.

FURBISH, D. J., 1991 Spatial autoregressive structure in meander evolution. *Geol. Soc. Am. Bull.* **103**(12), 1576–1589.

GAGLIANO, S. M. & HOWARD, P. C., 1984 Neck cutoff oxbow lake cycle along the lower mississippi river. 147–158.

GAO, M. & ROELVINK, D., 2010 Pilot study on navigation channel regulation works in the North Channel, Yangtze Estuary. In *Proceedings of 32nd Conference on Coastal Engineering, Shangai.* Coastal engineering Research Council, 1–13.

GARGETT, A., 1989 Ocean turbulence. *Annu. Rev. Fluid Mech.* **21**, 419–451.

GARRETT, C. & MUNK, W., 1979 Internal waves in the ocean. *Annu. Rev. Fluid Mech.* **11**, 339–369.

GILPIN, R. R., 1981 Ice formation in a pipe containing flows in the transition and turbulent regimes. *J. Heat Trans.-T. ASME* **103**(2), 363–365.

GILPIN, R. R. & CHENG, K. C., 1980 Wave formation and heat transfer in an ice-water interface in the presence of a turbulent flow. *J. Fluid Mech.* **99**(3), 619–640.

GILVEAR, D. & WILLBY, N., 2006 Channel dynamics and geomorphic variability as controls on gravel bar vegetation; River Tummel, Scotland. *River Research and Applications* **22(4)**, 457–474.

GOLUB, G. & VAN LOAN, C., 2001 *Matrix Computations.* John Hopkins Univ. Press, first edition.

GOLZ, E., 1990 Suspended sediment and bed load problems of the upper Rhine. *Catena* **17**(2), 127–140.

GOODCHIL, M. F. & FORD, D. C., 1971 Analysis of scallop patterns by simulation under controlled conditions. *J. Geol.* **79**(1), 52.

GRADOWCZYK, M. H., 1970 Wave propagation and boundary instability in erodible-bed channels. *J. Fluid Mech.* **33**, 93–112.

GRIFFITHS, R. W., 2000 The dynamics of lava flows. *Annu. Rev. Fluid Mech.* **32**, 477–518.

GUASTO, J. S.; RUSCONI, R. & STOCKER, R., 2012 Fluid mechanics of planktonic microorganisms. *Annu. Rev. Fluid Mech.* **44**, 373–400.

GURNELL, A. M. & PETTS, G. E., 2002 Island-dominated landscapes of large floodplain rivers, a European perspective. *Freshwater. Biol.* **47**(4), 581–600.

GUY, H. P.; SIMONS, D. B. & RICHARDSON, E. V., 1966 Summary of alluvial channel data from flume experiments. *Prof. paper U.S. Geol. Survey* **462-I**, 1–96.

HAFF, P. K. & ANDERSON, R. S., 1993 Grain scale simulations of loose sedimentary beds: the example of grain-bed impacts in aeolian saltation. *Sedimentology* **40**(2), 175–198.

HALL, P., 2004 Alternating bar instabilities in unsteady channel flows over erodible beds. *J. Fluid Mech.* **499**, 49–73.

HALL, P., 2005 On the non-parallel instability of sediment-carrying channels of slowly varying width. *J. Fluid Mech.* **529**, 1–32.

HALL, P., 2006 Nonlinear evolution equations and the braiding of weakly transporting flows over gravel beds. *Studies in Applied Mathematics* **117**, 27–69.

HANRATTY, T. J., 1981 Stability of surfaces that are dissolving or being formed by convective diffusion. *Annu. Rev. Fluid Mech.* **13**, 231–252.

HARBOR, D. J., 1998 Dynamics of bedforms in the lower Mississippi River. *J. Sediment. Res.* **68**(5), 750–762.

HAYASHI, T., 1970 Formation of dunes and antidunes in open channels. *J. Hydraul. Div.* **96(2)**, 357–366.

HE, S. & SEDDIGHI, M., 2013 Turbulence in transient channel flow. *J. Fluid Mech.* **715**, 60–102.

HOWARD, A. D., 1992 Modeling channel migration and floodplain sedimentation in meandering streams. In *Lowland Floodplain Rivers*. 1–41.

HUERRE, P., 2000 Open shear flow instabilities. In *Perspectives in Fluid Dynamics: A Collective Introduction to Current Research*, editors, J.K. BATCHELOR, H. & WORSTER, M.. Cambridge University Press,Cambridge, 159–229.

HUERRE, P. & MONKEVITZ, P. A., 1990 Local and global instabilities in spatially developing flows. *Annu. Rev. Fluid Mech.* **22**, 473–537.

HUERRE, P. & ROSSI, M., 2000 Hydrodynamic instabilities in open flows. In *Hydrodynamic and instabilities*, editors, GOLDRECHE, C. & MANNEVILLE, P.. Cambridge University Press,Cambridge, 159–229.

HUNTER, K. S.; WANG, Y. & VAN CAPPELLEN, P., 1998 Kinetic modeling of microbially-driven redox chemistry of subsurface environments: coupling transport, microbial metabolism and geochemistry. *J. Hydrol.* **209**(1-4), 53–80.

HWANG, S. H. & CHANG, H. C., 1987 Turbulent and inertial roll waves in inclined film flow. *Phys. Fluids* **30**, 1259–1268.

IKEDA, S., 1982 Prediction of alternate bar wavelength and height. *Technical Report 12*, Rep Dep. Found. Eng. Const. Eng. Saitama Univ.

IKEDA, S.; PARKER, G. & SAWAI, K., 1981 Bend theory of river meanders -1. Linear development. *J. Fluid Mech.* **112**, 363–377.

JAEGGI, M., 1984 Formation and effects of alternate bars. *J. Hydraul. Eng.* **110**, 142–156.

187

JEONG, J. & HUSSAIN, F., 1995 On the identification of a vortex. *J. Fluid Mech.* **285**, 69–94.

JONES, J. & MULHOLLAND, P., 2000 *Streams and groundwaters.* Elsevier, New York, first edition.

JULIEN, P. Y. & KLAASSEN, G. J., 1995 Sand-dune geometry of large rivers during floods. *J. Hydraul. Eng.-ASCE* **121**(9), 657–663.

KEMP, J. L.; HARPER, D. M. & CROSA, G. A., 2000 The habitat-scale ecohydraulics of rivers. *Ecological engineering* **16**(1), 17 – 29.

KENNEDY, J. F., 1963 The mechanics of dunes and antidunes in erodible-bed channels. *J. Fluid Mech.* **16**, 521–544.

KIM, J.; MOIN, P. & MOSER, R., 1987 Turbulence statistics in fully developed channel flow at low Reynolds number. *J. Fluid Mech.* **177**, 133–166.

KING, M. & LEIGHTON, D. T., 1997 Measurement of the inertial lift on a moving sphere in contact with a plane wall in a shear flow. *Phys. Fluids* **9**(5), 1248–1255.

KLEIN, R., 2010 Scale-dependent models for atmospheric flows. *Annu. Rev. Fluid Mech.* **42**, 249–274.

KLEINHANS, M. G., 2004 Sorting in grain flows at the lee side of dunes. *Earth-Sci. Rev.* **65**(1-2), 75–102.

KOBAYASHI, S. & ISHIDA, T., 1979 Interaction between wind and snow surface. *Bound. Lay. Meteorol.* **16**(1), 35–47.

KOCUREK, G., 1991 Interpretation of ancient eolian sand dunes. In *Annu. Rev. Earth. Pl. Sc., 19.* 43–75.

KOSTIC, S.; SEQUEIROS, O.; SPINEWINE, B. & PARKER, G., 2010 Cyclic steps: A phenomenon of supercritical shallow flow from the high mountains to the bottom of the ocean. *Journal of Hydro-environment Research* **3**(4), 167 – 172.

KOSUGI, K.; NISHIMURA, K. & MAENO, N., 1992 Snow ripples and their contribution to the mass transport in drifting snow. *Bound. Lay. Meteorol.* **59**(1-2), 59–66.

KU, D. N., 1997 Blood flow in arteries. *Annu. Rev. Fluid Mech.* **29**, 399–434.

LANGHORNE, D. N., 1982 A study of the dynamics of a marine sandwave. *Sedimentology* **29**(4), 571–594.

LANZONI, S., 2000 Experiments on bar formation in a straight flume: 1. Uniform sediment. *Water Resour. Res.* **36(11)**, 3337–3349.

LANZONI, S. & SEMINARA, G., 2006 On the nature of meander instability. *J. Geophys. Res.* **111**(f4).

LANZONI, S.; SEMINARA, G. & SIVIGLIA, A., 2008 Reply to comment by Cao and Hu on "Long waves in erodible channels and morphodynamic influence". *Water Resour. Res.* **44**, W06 602.

LANZONI, S.; SIVIGLIA, A.; FRASCATI, A. & SEMINARA, G., 2007 Long waves in erodible channels and morphodynamic influence. *Water Resour. Res.* **42**, W06D17.

LECLAIR, S. F., 2002 Preservation of cross-strata due to the migration of subaqueous dunes: an experimental investigation. *Sedimentology* **49**(6), 1157–1180.

LEE, C. & WU, J., 2008 Transition in wall-bounded flows. *Appl. Mech. Rev.* **61(3)**, 030 802.

LEE, H. & BALACHANDAR, S., 2010 Drag and lift forces on a spherical particle moving on a wall in a shear flow at finite Re. *J. Fluid Mech.* **657**, 89–125.

LEE, H. Y. & HSU, I. S., 1994 Investigation of saltating particle motion. *J. Hydraul. Eng.* **120**, 831–845.

LEOPOLD, L.; WOLMAN, M. & MILLER, J., 1964 *Fluvial processes in geomorphology*. W.H. Freeman and C., first edition.

LEWIN, J., 1976 Initiation of bed forms and meanders in coarse-grained sediments. *Geol. Soc. Am. Bull.* **87(2)**, 281–285.

LILLYCROP, J. W.; ROSATI, J. D. & MCGEHEE, D. D., 1989 A study on sand waves in the Panama City, Florida, entrance channel. *Technical Report CERC-TR-89-7*, US Army Engineer and Development Center.

LINDEN, P. F., 1999 The fluid mechanics of natural ventilation. *Annu. Rev. Fluid Mech.* **31**, 201–238.

LIVERPOOL, T. B. & EDWARDS, S. F., 1995 Dynamics of a meandering river. *Phys. Rev. Lett.* **75**(16), 3016–3019.

LUCHINI, P. & CHARRU, F., 2010 The phase lead of shear stress in shallow-water flow over a perturbed bottom. *J. Fluid Mech.* **665**, 516–539.

LUQUE, R. F. & VAN BEEK, R., 1976 Erosion and transport of bed load sediemnt. *J. Hydraul. Res.* **14**, 127–144.

MALIK, S. & HOOPER, A., 2007 Three-dimensional disturbances in channel flows. *Phys. Fluids* **19**, 052 102.

MARCIANO, R.; WANG, Z. B.; HIBMA, A.; DE VRIEND, H. J. & DEFINA, A., 2005 Modeling of channel patterns in short tidal basins. *J. Geophys. Res.* **110**(1).

MARTIN, S., 1974 Ice stalactites: comparison of laminar flow theory with experiment. *J. Fluid Mech.* **63**(1), 51–79.

MARTIN-PEREZ, A.; MARTIN-GARCIA, R. & ALONSO-ZARZA, A. M., 2012 Diagenesis of a drapery speleothem from Castaiar cave: from dissolution to dolomitization. *Int. J. Spel.* **41**(2), 251–266.

MARZADRI, A.; TONINA, D.; BELLIN, A.; VIGNOLI, G. & TUBINO, M., 2010 Semianalytical analysis of hyporheic flow induced by alternate bars. *Water Resour. Res* **46**.

MEYER-PETER, E. & MULLER, R., 1948 Proc. 2nd Meeting IAHSR. In *Formulas for bed–load transport*. IAHSR, 1–26.

MILES, J. W., 1980 Solitary waves. *Annu. Rev. Fluid Mech.* **12**, 11–43.

MOIN, P. & MAHESH, K., 1998 Direct numerical simulation: a tool in turbulence research. *Annu. Rev. Fluid Mech.* **30**, 539–578.

MONDET, J.; LEROUX, C.; VINAY, G.; CANDAUDAP, F.; LE MEUR, E. & FILY, M., 1997 Images of antarctic sastrugi at different scales from ground to satellite. In *Proceedings of the EARSEL workshop on remote sensing of land ice and snow*, editor, WUNDERLE, S . 53–60.

NAUMBURG, E.; MATA-GONZALEZ, R.; HUNTER, R. G.; McLENDON, T. & MARTIN, D. W., 2005 Phreatophytic vegetation and groundwater fluctuations: a review of current research and application of ecosystem response modeling with an emphasis on great basin vegetation. *Environ. Manage.* **35**(6), 726–740.

NEEDHAM, D. J. & MERKIN, J. H., 1984 On roll waves down an open inclined channel. *Proc. Roy. Soc. A.* **394**, 259–278.

NELSON, J. & SMITH, J., 1989 Flow in meandering channels with natural topography. In *River Meandering*, editors, IKEDA, S. & PARKER, G.. AGU, 69–102.

NEUFELD, J. A.; GOLDSTEIN, R. E. & WORSTER, M. G., 2010 On the mechanisms of icicle evolution. *J. Fluid Mech.* **647**, 287–308.

NEUMAN, C. M., 1993 A review of aeolian transport processes in cold environments. *Prog. Phys. Geog.* **17**(2), 137–155.

NIKORA, V. I.; SAPOZHNIKOV, V. B. & NOEVER, D. A., 1993 Fractal geometry of individual river channels and its computer simulation. *Water. Resour. Res.* **29**(10), 3561–3568.

NINO, Y.; GARCIA, M. & AYALA, L., 1994 Gravel saltation 1. experiments. *Water Resour. Res.* **30**, 1907–1914.

OGAWA, N. & FURUKAWA, Y., 2002 Surface instability of icicles. *Phys. Rev. E* **66**(4), 041 202/1–041 202/11.

OLESEN, K., 1983 Alternate bars and meandering of alluvial rivers. In *River Meandering: proceedings of the Conference Rivers 1983, New Orleans, Louisiana*, editor, CHARLES, E.. ASCE, 873–884.

OLSSON, P. & HENNINGSON, D., 1995 Optimal disturbance growth in water table flow. *Stud. Appl. Math.* **94**, 183–210.

ORON, A.; DAVIS, S. H. & BANKOFF, S. G., 1997 Long-scale evolution of thin liquid films. *Rev. Mod. Phys.* **69**(3), 931–980.

PACKMAN, A. I. & BROOKS, N. H., 2001 Hyporheic exchange of solutes and colloids with moving bed forms. *Water. Resour. Res.* **37**(10), 2591–2605.

PARISH, T., 1988 Surface winds over the Antarctic Continent: a review. *Rev. Geophys.* **26**(1), 169–180.

PARKER, G., 1975a Meandering of supraglacial melt streams. *Water. Resour. Res.* **11**(4), 551–552.

PARKER, G., 1975b Sediment inertia as cause of river antidunes. *J. Hydr. Div.* **101(2)**, 211–221.

PARKER, G., 1976 On the cause and characteristic scales of meandering and braiding in rivers. *J. Fluid Mech.* **76**, 457–480.

PARKER, G. & JOHANNESSON, K., 1989 Observations on several recent theories of resonance and overdeepening in meandering channels. In *River meandering*, editors, IKEDA, S. & PARKER, G.. AGU, 379–415.

PARKER, G.; PAOLA, C.; WHIPPLE, K. X. & MOHRIG, D., 1998 Alluvial fans formed by channelized fluvial and sheet flow. 1: Theory. *J. Hydraul. Eng.-ASCE* **124**(10), 985–995.

PARKER, G.; SEMINARA, G. & SOLARI, L., 2003 Bed load at low shields stress on arbitrarily sloping beds: Alternative entrainment formulation. *Water Resour. Res.* **39(7)**, 1183.

PARKER, G. & SEQUEIROS, O., 2006 Large scale river morphodynamics: application to the Mississippi delta. In *River Flow 2006*, Proceedings and monographs in engineering, water and earth sciences , editor, FERREIRA, R M L AND ALVES, C T L AND LEAL, G A B AND CARDOSO, A H. 3–11.

PEREGRINE, D. H., 1983 Breaking waves on beaches. *Annu. Rev. Fluid Mech.* **15**, 149–178.

PERRON, J. T.; DIETRICH, W. E. & KIRCHNER, J. W., 2008 Controls on the spacing of first-order valleys. *J. Geophys. Res.* **113**(4).

POTTER, M. C. & WIGGERT, D. C., 1991 *Mechanics of fluids.* Prentice-Hall, New York.

POWELL, D. M., 1998 Patterns and processes of sediment sorting in gravel-bed rivers. *Prog. Phys. Geog.* **22**(1), 1–32.

PREUSSER, F.; RADIES, D. & MATTER, A., 2002 A 160,000-year record of dune development and atmospheric circulation in Southern Arabia. *Science* **296**(5575), 2018–2020.

RANASINGHE, R. & PATTIARATCHI, C., 2003 The seasonal closure of tidal inlets: causes and effects. *Coast. Eng. J* **20**, 2347–2366.

RECKING, A.; BACCHI, V.; NAAIM, M. & FREY, P., 2009 Antidunes on steep slopes. *J. Geophys. Res.* **114**(F4), 2156–2202.

REDDY, S. & HENNINGSON, D., 1993 Energy growth in viscous channel. *J. Fluid Mech.* **252**, 209–238.

REINFELDS, I. & NANSON, G., 1993 Formation of braided river floodplains, Waimakariri River, New Zealand. *Sedimentology* **40**(6), 1113–1127.

REMPFER, D., 2003 Low-dimensional modelling and numerical simulation of transition in simple shear flows. *Annu. Rev. Fluid Mech* **252**, 209–238.

REPETTO, R.; TUBINO, M. & PAOLA, C., 2002 Planimetric instability of channels with variable width. *J. Fluid Mech.* **457**, 79–109.

REYNOLDS, A. J., 1965 Waves on an erodible bed. *J. Fluid Mech.* **22**, 113–133.

RICCO, P.; LUO, J. & WU, X., 2011 Evolution and instability of unsteady nonlinear streaks generated by free-stream vortical disturbances. *J. Fluid Mech.* , 1–38.

RICHARDS, K. J., 1980 The formation of ripples and dunes on an erodible bed. *J. Fluid Mech.* **99**, 597–618.

193

ROELVINK, J. & BROKER, I., 1993 Cross-shore profile models. *Coast. Eng.* **21**, 163 – 191.

RUST, B. & GOSTIN, V., 1981 Fossil transverse ribs in Holocene alluvial fan deposits, Depot Creek, South Australia. *J. Sediment. Res.* **51**, 441–444.

SAFFMAN, P. G., 1965 The lift on a small sphere in a slow shear flow. *J. Fluid Mech.* **22**, 385–400.

SAUERMANN, G.; KROY, K. & HERRMANN, H. J., 2001 Continuum saltation model for sand dunes. *Phys. Rev. E* **64**(3i), 313 051–3130 510.

SAUERMANN, G.; ROGNON, P.; POLIAKOV, A. & HERRMANN, H. J., 2000 The shape of the barchan dunes of Southern Morocco. *Geomorphology* **36**(1-2), 47–62.

SCHIELEN, R.; DOELMAN, A. & DE SWART, H., 1993 On the nonlinear dynamics of free bars in straight channels. *J. Fluid Mech.* **252**, 325–356.

SCHMID, P., 2007 Nonmodal stability theory. *Annu. Rev. Fluid Mech.* **39**, 129–162.

SCHMID, P. & HENNINGSON, D., 2001 *Stability and Transition in Shear Flows.* Springer, First Edition.

SCHNEIDER, T., 2006 The general circulation of the atmosphere. *Annu. Rev. Earth. Pl. Sc.* **34**, 655–688.

SCHUTTELAARS, H. M. & DE SWART, H. E., 1999 Initial formation of channels and shoals in a short tidal embayment. *J. Fluid Mech.* **386**, 15–42.

SEKINE, M. & KIKKAWA, H., 1992 Mechanics of saltating grains. *J. Hydraul. Eng.* **118**, 536–558.

SEKINE, M. & PARKER, G., 1992 Bed load transport on transverse slope. *J. Hydraul. Engng ASCE* **118**, 513–535.

SEMINARA, G., 2006 Meanders. *J. Fluid Mech.* **554**, 271–297.

194

SEMINARA, G., 2010 Fluvial sedimentary patterns. *Annu. Rev. Fluid Mech.* **42**, 43–66.

SEMINARA, G.; SOLARI, L. & G.PARKER, 2002 Bed load at low shields stress on arbitrarily sloping beds: Failure of the Bagnold hypothesis. *Water Resour. Res.* **38(11)**, 1249.

SEMINARA, G. & TUBINO, M., 1989 Alternate bars and meandering: Free, forces and mixed interactions. In *Sand Transport in Rivers, Estuaries and the sea*, editors, IKEDA, S. & PARKER, G.. AGU, 267–320.

SEMINARA, G.; ZOLEZZI, G.; TUBINO, M. & ZARDI, D., 2001 Downstream and upstream influence in river meandering. part 2. planimetric development. *J. Fluid Mech.* **438**, 213–230.

SHAW, J. & KELLERHALS, R., 1977 Paleohydraulic interpretation of antidune bedforms with applications to antidunes in gravel. *J. Sedimentary Petrology* **47**, 57–266.

SHORT, M. B.; BAYGENTS, J. C. & GOLDSTEIN, R. E., 2005 Stalactite growth as a free-boundary problem. *Phys. Fluids* **17**(8), 1–12.

SIMPSON, R. L., 2001 Junction flows. *Annu. Rev. Fluid Mech.* **33**, 415–443.

SNOW, R., 1989 Fractal sinuosity of stream channels. *Pure Appl. Geophys.* **131**(1-2), 99–109.

SPIJKER, M., 1991 On a conjecture by le Veque and Trefethen related to the Kreiss matrix theorem. *BIT Numer. Math.* **31**, 551–555.

STEIGER, J.; GURNELL, A. M. & PETTS, G. E., 2001 Sediment deposition along the channel margins of a reach of the middle River Severn, UK. *River Research and Applications* **17**(4-5), 443–460.

STØLUM, H. H., 1996 River meandering as a self-organization process. *Science* **271**(5256), 1710–1713.

STØLUM, H. H., 1997 Fluctuations at the self-organized critical state. *Phys. Rev. E* **56**(6), 6710–6718.

STØLUM, H. H., 1998 Planform geometry and dynamics of meandering rivers. *Geol. Soc. Am. Bull.* **110**(11), 1485–1498.

STRIDE, A. H., 1982 *Offshore tidal sands : processes and deposits.* Chapman and Hall, New York.

SUN, T.; MEAKIN, P.; JOSSANG, T. & SCHWARZ, K., 1996 A simulation model for meandering rivers. *Water. Resour. Res.* **32**(9), 2937–2954.

SWENSON, J. B.; VOLLER, V. R.; PAOLA, C.; PARKER, G. & MARR, J. G., 2000 Fluvio-deltaic sedimentation: a generalized Stefan problem. *Eur. J. App. Math.* **11**(5), 433–452.

TAMBRONI, N.; BOLLA PITTALUGA, M. & SEMINARA, G., 2005 Laboratory observations of the morphodynamic evolution of tidal channels and tidal inlets. *J. Geophys. Res.* **110**(4).

TAMBRONI, N. & SEMINARA, G., 2006 Are inlets responsible for the morphological degradation of Venice lagoon? *J. Geophys. Res.* **111**(3).

TAYLOR, G. I., 1923 Stability of a viscous liquid contained between two rotating cylinders. *Philos. T. Roy. Soc. A* **223**(605-615), 289–343.

TEALDI, S.; CAMPOREALE, C. & RIDOLFI, L., 2011 Modeling the impact of river damming on riparian vegetation. *J. Hydrol.* **396**(3-4), 302–312.

TEALDI, S.; CAMPOREALE, C. & RIDOLFI, L., 2013 Inter-species competition-facilitation in stochastic riparian vegetation dynamics. *J. Theor. Biol.* **318**, 13–21.

THIBODEAUX, L. J. & BOYLE, J. D., 1987 Bedform-generated convective transport in bottom sediment. *Nature* **325**(6102), 341–343.

TOCKNER, K.; MALARD, F. & WARD, J. V., 2000 An extension of the flood pulse concept. *Hydrol. Process.* **14**(16-17), 2861–2883.

TONINA, D. & BUFFINGTON, J. M., 2007 Hyporheic exchange in gravel bed rivers with pool-riffle morphology: laboratory experiments and three-dimensional modeling. *Water. Resour. Res.* **43**(1).

TREFETHEN, L. & EMBREE, M., 2001 *Spectra and Pseudospectra.* Princeton Univ. Press, first edition.

TREFETHEN, L.; TREFETHEN, A.; REDDY, S. & DRISCOLL, T., 1993 Hydrodynamic stability without eigenvalues. *Science* **261**, 578 – 584.

TROWBRIDGE, J. H., 1995 A mechanism for the formation and maintenance of shore-oblique sand ridges on storm-dominated shelves. *J. Geophys. Res.* **100**(c8), 16 071–16 086.

TUBINO, M.; REPETTO, R. & ZOLEZZI, G., 1999 Free bars in rivers. *J. Hydr. Res.* **37(6)**, 759–775.

TUCKER, G. E. & BRAS, R. L., 1998 Hillslope processes, drainage density, and landscape morphology. *Water. Resour. Res.* **34**(10), 2751–2764.

UENO, K., 2003 Pattern formation in crystal growth under parabolic shear flow. *Phys. Rev. E* **68**(21), 021 603/1–021 603/14.

VAN DE GRAAFF, W. J. E. & EALEY, P. J., 1989 Geological modeling for simulation studies. *Am. Ass. Petroleum Geol. Bull.* **73**(11), 1436–1444.

VAN DE KREEKE, J., 1990 Can multiple tidal inlets be stable? *Estuar. Coast. Shelf. S.* **30**(3), 261–273.

VAN DER VEGT, M.; SCHUTTELAARS, H. M. & DE SWART, H. E., 2007 Modeling the formation of undulations of the coastline: the role of tides. *Cont. Shelf Res.* **27**(15), 2014–2031.

VAN DIJK, W. M.; VAN DE LAGEWEG, W. I. & KLEINHANS, M. G., 2012 Experimental meandering river with chute cutoffs. *J. Geophys. Res.* **117**(3).

VAN RIJN, L. C., 1998 *Principles of coastal morphology.* Aqua Publications,Blokzijl, The Netherlands.

VISCONTI, F.; CAMPOREALE, C. & RIDOLFI, L., 2010 Role of discharge variability on pseudomeandering channel morphodynamics: Results from laboratory experiments. *J. Geophys. Res.* **115**, F04 042.

VITTORI, G. & BLONDEAUX, P., 1990 Sand ripples under sea waves-2. Finite-amplitude development. *J. Fluid Mech.* **218**, 19–39.

VITTORI, G.; DE SWART, H. E. & BLONDEAUX, P., 1999 Crescentic bedforms in the nearshore region. *J. Fluid Mech.* **381**, 271–303.

WARD, J.; TOCKNER, K.; ARSCOTT, D. & CLARET, C., 2002 Riverine landscape diversity. *Freshwater Biology* **47**, 517–539.

WEBER, K. J., 1986 How heterogeneity affects oil recovery. In *Reservoir Characterization.* 487–544.

WENDL, M. C., 1999 General solution for the Couette flow profile. *Phys. Rev. E* **60**(5b), 6192–6194.

WILLGOOSE, G.; BRAS, R. L. & RODRIGUEZ-ITURBE, I., 1991 A coupled channel network growth and hillslope evolution model .1. Theory. *Water. Resour. Res.* **27**(7), 1671–1684.

WILLIAMS, J., 1977 Aeroacoustics. *Annu. Rev. Fluid Mech.* **9**, 447–468.

WOODS, A. W., 2010 Turbulent plumes in nature. *Annu. Rev. Fluid Mech.* **42**, 391–412.

WU, F.; SHAO, Y. & CHEN, Y., 2011 Quantifying the forcing effect of channel width variations on free bars: Morphodynamic modeling based on characteristic dissipative galerkin scheme. *J. Geophys. Res.* **116**, F03 023.

WUNSCH, C. & FERRARI, R., 2004 Vertical mixing, energy and the general circulation of the oceans. *Annu. Rev. Fluid Mech.* **36**, 281–314.

YECKO, P., 2008 Disturbance growth in two-fluid channel flow: the role of capillarity. *Int. J. Mulyiphase Flow* **34**, 72–282.

YOKOKAWA, M.; TAKAHASHI, Y.; YAMAMURA, H.; KISHIMA, Y.; PARKER, G. & IZUMI, N., 2011 Antidunes and cyclic steps: relating their features to a suspension index and a velocity coefficient. In *Japan Geoscience Union Meeting 2011*. Japan Geoscience Union, SCG064–14.

YUN, G.; KIM, D. & CHOI, H., 2006 Vortical structures behind a sphere at subcritical Reynolds numbers. *Phys. Fluids* **18**(1).

ZANG, T. A. & KRIST, S. E., 1989 Numerical experiments on stability and transition in plane channel flow. *Theor. Comp. Fluid Dyn.* **1**(1), 41–64.

ZELLER, J., 1967 Meandering channels in Switzerland. In *Symposium on river morphology*, editor, IUGG AND IASH . 174–186.

ZHANG, D. & SUNAMURA, T., 2011 Multiple bar formation by breaker-induced vortices: a laboratory approach. *Coast. Eng. Proc.* **1**(24).

ZOLEZZI, G.; GUALA, M.; TERMINI, D. & SEMINARA, G., 2005 Experimental observations of upstream overdeepening. *J. Fluid Mech.* **531**, 191–219.

ZOLEZZI, G. & SEMINARA, G., 2001 Downstream and upstream influence in river meandering. Part 1. General theory and application overdeepening. *J. Fluid Mech.* **438**, 183–211.